# UNDERSTANDING THE ROLE OF HCN IN STAR FORMATION STUDIES

Gerwyn Hill Jones

A Thesis submitted to
Cardiff University
for the degree of
Doctor of Philosophy

April 2023

*"Be OK with mediocrity"*
*Michael Anderson*

# ACKNOWLEDGEMENTS

Well, where to begin? There have been so many people who have helped me through my PhD.

First and foremost, to my incredible supervisor Dr Paul Clark, who has suffered with me longer than most should. From the first undergraduate project six years ago to this doctorate today, you have been incredibly supportive and understanding through very dark days. I will be forever grateful for the help that you've provided over the past 6 years.

My special thanks also go to Lewis Prole and Felix Priestley. Our shared experience of Vater Rhein, Heidelberg will be ingrained in my memories for years to come. To my D&D adventuring group (Jacob Elford, Holly Davies, Jaspa Stritt, Hidde Jense and again Lewis), those Mondays were always the brightest part of my week in which I looked forward to killing invincible vampires and evil dragons.

To those in my office over the past 4 years (Michael Anderson, Elizabeth Watkins, Zeinab Khorrami, Roger Wesson and again Felix and Lewis), your acceptance of my Colombian flag taking pride of place in the office was greatly appreciated. Michael: your persistent check-ins during many a dark day did not go unnoticed, thank you. Thanks to all at The Rest Frame coffee breaks who, although my presence was often rare but consistent in my high scoring on the Peñoloza scale, were always there to support me on my lowest days of which there were many.

Most importantly, I would like to thank my family. / Yn bennaf ôll, hoffwn rhoi diolch i fy nheulu. Mam, Dad a Rhodri: mi fyswn i ar goll heb eich cariad a chefnogaeth. I Mam a Dad, mae'n rhaid i mi ddiolch i chi am eich cefnogaeth yn ariannol a emosiynol dros y dyddiau dywyll. Hefyd mae'n rhaid diolch i ti Rhodri am yr holl golffio a'r snwcer ti di talu am, ond plis rho cyfle i mi ennill rhyw ddydd!

# SUMMARY

Star formation studies currently rely on the HCN J = 1 → 0 emission since it is thought to trace the same dense gas regions in which star formation occurs (at densities above $10^4$ cm$^{-3}$). However, new studies show that HCN J = 1 → 0 emission trace densities below $10^4$ cm$^{-3}$ at densities of around $10^3$ cm$^{-3}$. In this work, we focus on modelling the HCN emission from simulated molecular clouds and investigate the density regime probed by HCN emission.

We model the molecular cloud environments through cloud-cloud collisions using a Voronoi moving-mesh hydrodynamical code called AREPO. These molecular clouds are then post-processed by a radiative transfer code called RADMC-3D that produces synthetic images of HCN emission. 10 simulations in total were made; 4 simulations were produced that varied the initial collisional velocity of the clouds. 6 simulations were produced that varied the interstellar radiation field strength (ISRF).

For the variations in the initial collisional cloud velocity, we find HCN emission traces gas with a volumetric density of $\sim 2.85 \times 10^3$ cm$^{-3}$ and a visual extinction of $\sim 5.05$ mag. For the work on the variation of the ISRF strength, we find that HCN traces gas with a density of $4.3 \times 10^3$ cm$^{-3}$ and the visual extinction of 7 mag. These characteristic densities of $\sim 2.85 \times 10^3$ cm$^{-3}$ and $4.3 \times 10^3$ cm$^{-3}$ are more consistent with the observational studies that suggest that HCN emission traces more diffuse densities. This finding has implications in observational studies of HCN emission where HCN emission no longer provides evidence of “slow” star formation.

Our work on HCN emission has shown that it is not as simple to say that HCN emission traces a certain density or that the effective density of HCN emission can be described by one particular observational property such as the optical depth. We show that the effective density of HCN emission has some correlation with the local ISRF strength of the molecular cloud environment. We suggest that those observing HCN emission in the local Milky-Way or an environment similar to it should use an effective density of $\sim 3 \times 10^3$ cm$^{-3}$ with an upper limit of $\sim 1 \times 10^4$ cm$^{-3}$ for those observing regions of high star formation.

# PUBLICATIONS

## FIRST AUTHOR PUBLICATIONS

Jones, G. H., Clark, P. C., Glover, S. C. O., Hacar, A., 2023, *On the density regime probed by HCN emission.* MNRAS 520, 1005.

# CONTENTS

# LIST OF TABLES

# List of Figures

# CHAPTER 1

# INTRODUCTION

One of the most spine tingling moments of classical music occurs in Haydn's "The Creation", where a choir whispers "And God said: Let there be Light, and there was Light"; and with a sudden explosion of sound (from *ppp* to *fff* with an inclusion of a full orchestra) on the final word it is as if the whole universe explodes into light. Because of this thing called light, we have been able to uncover vast amount of knowledge of our universe. One of the main sources of light that we can see is stars: dense, nuclear burning, balls of gas. Understanding how stars are formed is of great importance to astrophysicists, since the formation of planets and the potential for life are byproducts of the formation of stars. Also, star formation produces the vast majority of the heavy elements in the Universe along with the death of stars being the main source of heavier elements.

## 1.1 STAR FORMATION

Starting on the largest scales, star formation occurs in galaxies, in which it was originally thought that the spiral arms of galaxies contributed significantly to the triggering of the formation of stars. However, Moore et al. (2012); Urquhart et al. (2014) and Ragan et al. (2018) have all argued that the role of spiral arms in star formation is insignificant, in that the inter-arms of the galaxy is just as likely to form stars compared to the spiral arms, it is simply that there is more gas in the arms to form more stars than the inter-arms.

To understand how these star forming regions occur we present a top down view of how the gas evolves from the galactic scale down to the molecular cloud scale. Starting at the largest scale, we have galaxies that consist of stars and the interstellar medium (ISM), that is the "stuff" between the stars. Galaxies come in various shapes and sizes and can be grouped into classifications according to Edwin Hubble's tuning

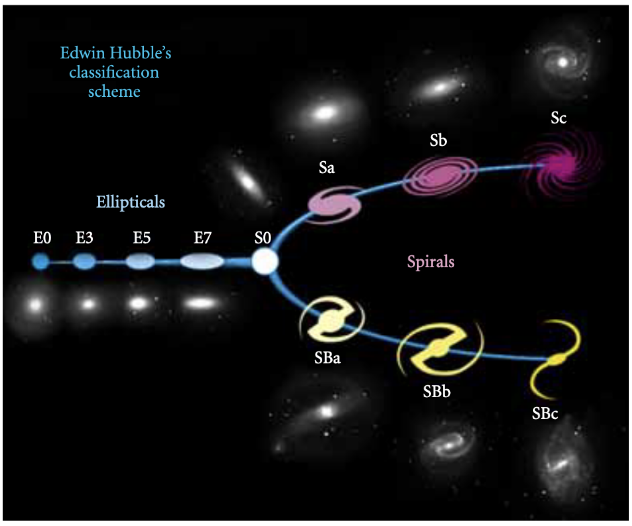

**Figure 1.1.** Figure from Aguerri (2012) showing the Hubble tuning fork where galaxies are grouped into classifications according to their shapes and ages.

**Table 1.1.** The density and temperature regimes of the phases of the ISM.

| ISM Phase | Density [$\mathrm{cm}^{-3}$] | Temperature [K] | Scale Height [pc] | Fractional Volume [%] |
|---|---|---|---|---|
| Hot Ionised Medium (HIM) | $\sim 0.003$ | $10^6$ | $\sim 1000$ | 30–70% |
| Warm Ionised Medium (WIM) | 0.1 | 8000 | $\sim 1000$ | 20–50% |
| Warm Neutral Medium (WNM) | 0.5 | 8000 | $\sim 300$ | 10–20% |
| Cold Neutral Medium (CNM) | 50 | 80 | $\sim 100-300$ | 1–5% |
| Molecular Cloud | 100 - $\geq 10^6$ | $\leq 50$ | $\sim 80$ | $< 1\%$ |

fork classification as seen in Figure 1.1. It is generally thought that galaxies evolve from spiral galaxies to ellipticals as they age, that is that they travel from right to left in Figure 1.1. One reason that it is thought that galaxies follow the tuning fork is that elliptical galaxies typically have very low star formation rates whereas spiral galaxies have comparatively much higher star formation rates.

Spiral galaxies such as our own Milky-Way span scale lengths of order of $\sim$ kiloparsecs (kpc) in the radial direction and order of parsecs to kiloparsecs in the vertical direction. Figure 1.2 shows a general overview of the different stages of star formation and how it is a multi scale process ranging from galactic scales to cloud scales.

The ISM is a multi-phase medium that accounts for $\sim 10-15\%$ of the total mass of the Galactic disk. It tends to concentrate near the Galactic plane and along the spiral arms. The ISM was an idea originated by Field et al. (1969), where pressure stable regions called phases arise from the equilibrium between the heating and

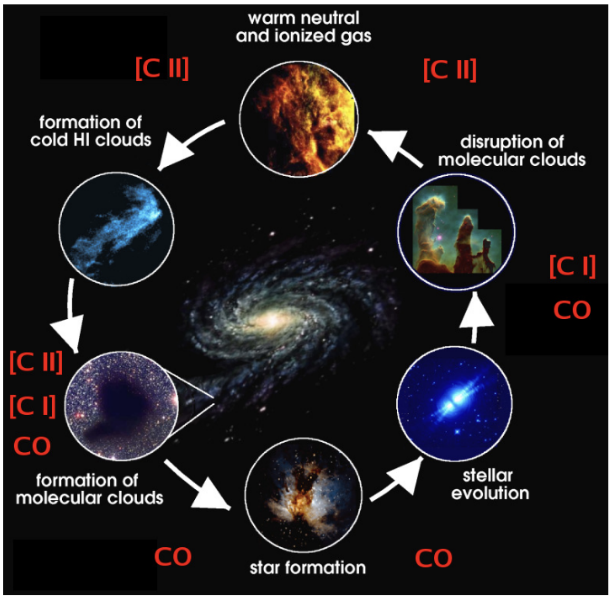

**Figure 1.2.** Figure from Kulesa et al. (2012) showing the different stages of star formation and how observers use different gas tracers to observe these stages.

cooling processes of the ISM. These phases have since evolved to through discourse in the scientific community to be 5 phases spanning densities of $\sim 10^{-3} - 10^{6}\mathrm{cm}^{-3}$ and temperatures of $\sim 10 - 10^{6}$K. The gas in the ISM is the reservoir for star formation and we therefore present these phases that play a vital role in star formation. Since the warm neutral medium phase feeds the cold neutral medium phase, which in turn feeds the molecular cloud phase, and due to the cooling instability, all of the gas in these phases can oscillate quickly. These phases are summarized in Table 1.1. For completeness, we include the hot and warm ionised medium in the table since these make up the entire ISM phase. However, these phases are not as important to our research compared to the warm and cold neutral medium along with the molecular cloud phase. Therefore, we only briefly describe the hot and warm ionised medium and delve deeper into the latter three phases.

The hot ionised medium (HIM) consists of ionised gas that makes up roughly 30-70% of the fractional volume of the ISM. To probe these regions of HIM such as H II regions, we take advantage of the fact that these ionised particles are moving incredibly fast and that these particles when in close proximity to one another can be attracted or repelled from each other and causes radiation due to the acceleration arising from this attraction or repulsion. This is the Bremsstrahlung radiation, and is often observed by X-rays.

The warm ionised medium (WIM) consists of ionised gas that makes up roughly 20-50% of the fractional volume of the ISM. To trace the WIM, we use the hydrogen alpha (H$\alpha$) line which is the first spectral line of the Balmer series. H$\alpha$ is observed in the visible region of the electromagnetic spectrum.

The warm neutral medium (WNM) consists of neutral gas that makes up roughly 20% of the fractional volume of the ISM. With most of the neutral gas being in the form of atomic hydrogen (HI). The typical scale height of the WNM is roughly 1000 pc and contains HI at a temperature of roughly 8000 K and a density of 0.5 cm$^{-3}$. Due to the transition from the first excited energy level to the ground state of neutral hydrogen (commonly referred to the Lyman-$\alpha$ transition) arising at a wavelength of 1216 Å and an energy of 10.2 eV (a temperature equivalence of $\sim 10^5$ K), its probability of being excited is incredibly low and therefore little to no emission arises from this transition. In order to observe HI, we use the 21-cm line emission that was first observed by Ewen & Purcell (1951). The existence of the 21-cm line results from the transitions within the "hyperfine" structure of the hydrogen atom. This is where the energy level splits into two due to the interactions between the electron spin and the neutron spin. There are two possible states that the electron and neutron spins can be orientated, one in which both are parallel to one another and one in which they are anti-parallel. The state where the spins are parallel is slightly higher in energy compared to the anti-parallel state and therefore the transition between these two states produces the 21cm emission line.

As the name suggests, the cold neutral medium (CNM) is like the WNM but colder and consists of neutral gas that makes up roughly 5% of the fractional volume of the ISM. The typical scale height of the CNM is roughly 300 pc and contains gas at a temperature of roughly 80 K and a density of 50 cm$^{-3}$. The gas is able to be cooled down to these temperatures due to the formation of other heavier gas species such as carbon, and through the very effective cooling of the ionized carbon hyperfine line ([CII]).

The coldest and densest phase of the ISM is molecular clouds, and consists of molecular gas that makes up less than 1% of the fractional volume of the ISM. The typical scale height of molecular clouds is roughly 80 pc and contains gas at a temperature of roughly less than 50 K and a density of anywhere between 100 to $10^6$ cm$^{-3}$. Molecular clouds vary in shapes and sizes and can start its life as a diffuse cloud that then condenses into clumps (Rigby et al., 2019) that fragment and form filamentary structures that are thought to have dense cores within these filamentary structures (André et al., 2010). These cores and filamentary structures are thought to be the main sites of star formation (André et al., 2010; Bontemps et al., 2010; Könyves et al., 2010). As we travel down this chain of possible events from diffuse clouds to dense cores, the gas in these regions get progressively denser. It is argued by Wu et al. (2010) and Lada et al. (2009) that there is a threshold density for star formation at around n $\sim 1 \times 10^4$ cm$^{-3}$. In molecular clouds, molecular hydrogen ($H_2$) can be formed from atomic hydrogen on the surface of dust grains. This process along with the large abundance of atomic hydrogen makes producing large amounts of molecular hydrogen possible. Once the densities are high enough ($> 10^3$ cm$^{-3}$) so $H_2$ gas can quickly self-shield from the ambient UV radiation, an environment in which other molecular gas species such as carbon monoxide (CO), diazenylium ($N_2H^+$) and hydrogen cyanide (HCN) can be formed.

On every scale (that is - galactic kpc scale, sub-kpc scale and cloud scale), observers are particularly motivated to find how much of the gas is converted to stars. This therefore brings us to the Kennicutt-Schmidt (KS) law named after the original work by Schmidt (1959) on the Milky-Way and the extension of this to extragalactic work by Kennicutt (1989). The KS law seen in Figure 1.3 that shows a correlation between the surface density of gas and the surface density of star formation rate. The KS law can be formalised by the following generalised equation,

$$\Sigma_{\rm SFR} = {\rm A}\Sigma_{\rm Gas}^{\rm N} \quad . \tag{1.1}$$

One might expect the KS relation to be between the volume densities of star formation and gas, but because most observations of external galaxies can measure only surface densities integrated along the line of sight, the KS law is commonly referred to by the surface densities of the gas and star formation rate. As there is no way to directly measure surface density through observations, we have to relate emission to surface density. In the case of the surface density of star formation, it is often found through observing the infrared (IR) emission, calculating its luminosity (LIR) and converting this luminosity by a star-formation-rate calibrated factor (Hao et al., 2011; Murphy et al., 2011). Equally, the surface density of gas requires emission from a gas tracer that is either atomic such as the HI 21cm line or molecular such as CO, HCN or $N_2H^+$. The integrated emission (CO emission is commonly used) is then related to $H_2$ column density $N(H_2)$ through an X-factor, where $N(H_2) = X(CO)\,I(CO)$. Kennicutt (1998) used a value of $X(CO) = 2.8 \times 10^{20}$ cm$^{-2}$ $({\rm K\,km\,s^{-1}})^{-1}$. Other studies such as Pineda et al. (2010) find a different value for the X(CO) and therefore studies investigating the KS relation often omits these conversion factors and relate the KS relation through the luminosities (i.e. $L_{\rm IR}$ v $L_{\rm CO}$). Also, Clark & Glover (2015) show that X(CO) is likely itself to be a function of SFR, which plays havoc with the KS relation.

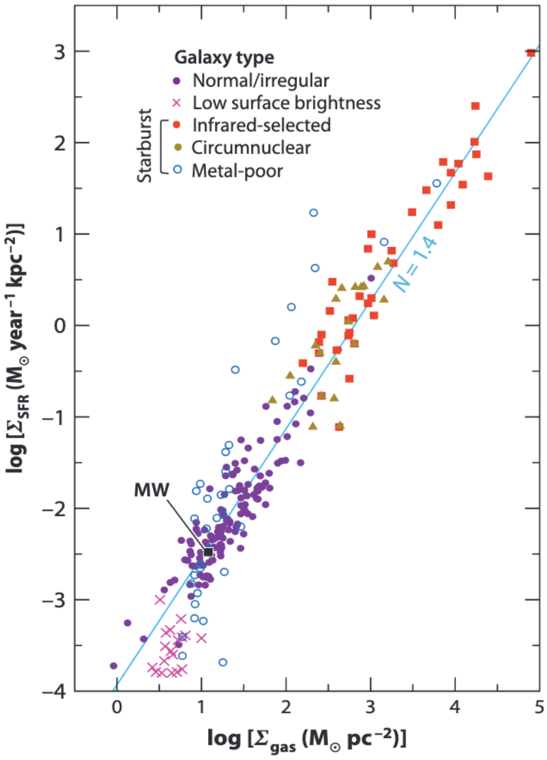

**Figure 1.3.** Figure from Kennicutt & Evans (2012) showing the integrated star-formation law for a number of different types of galaxy. The blue line indicates the canonical power-law index, N = 1.4.

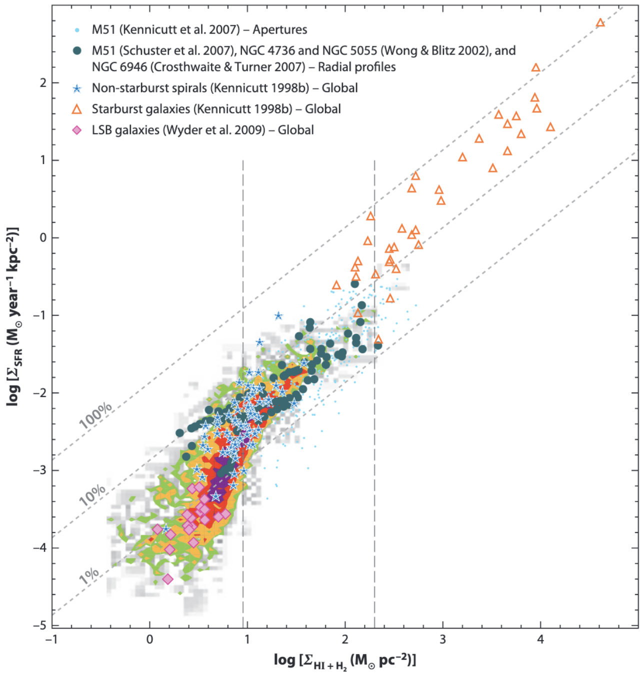

**Figure 1.4.** Figure from Bigiel et al. (2008) showing the KS relation of galaxies resolved to sub-kpc scales, the dotted grey lines denote lines of constant star formation efficiency with N = 1.0.

Kennicutt (1989) observed galaxies through a combination of HI and CO emission at a resolution where the galaxy would fill a single pixel. They found that the value for N in the KS relation to be N = 1.4. Other studies such as Bigiel et al. (2008) observe galaxies with CO emission where the resolution was able to be at sub-kpc scales. At these sub-kpc scales, Bigiel et al. (2008) found a change in the slope in the KS relation where N = 1.0 (see Figure 1.4). They also find a result in the star formation efficiency; that is the percentage of gas that is able to form stars where 0% means that none of the gas is converted stars and 100% means that all of the gas is converted to stars. They found that the star formation efficiency was typically low (below 10 %) and that this therefore means that galaxies are very inefficient at forming stars. Going to smaller scales, Wu et al. (2005) uses HCN emission to probe galactic dense cores and find a similar KS relation to Bigiel et al. (2008) of N = 1.0. The use of HCN emission was also used by Gao & Solomon (2004b) to show that the correlation has a smaller dispersion for the KS relationship found with HCN emission compared to CO emission and that their star formation efficiency is also typically around 10%. It is argued that this smaller dispersion in the correlation for HCN emission is due to the fact that HCN traces denser gas compared to CO (which we will go into further in Section 1.2) and therefore more likely to omit diffuse gas that

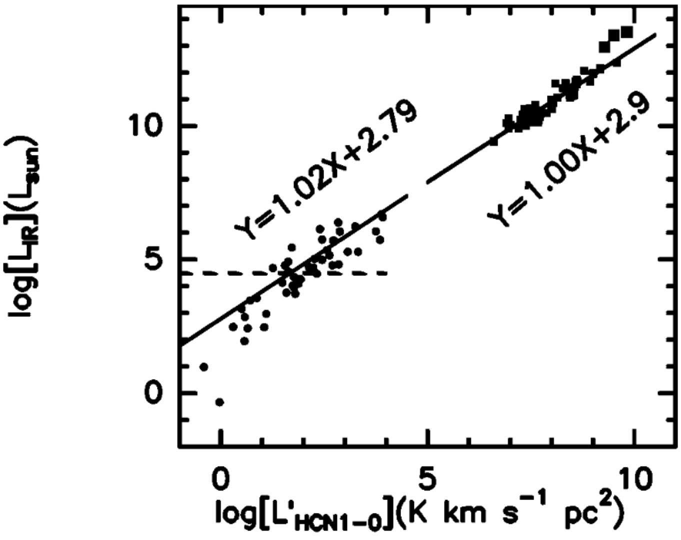

**Figure 1.5.** Figure from Wu et al. (2005) showing the KS relation of galaxies resolved to sub-kpc scales, the dotted grey lines denote lines of constant star formation efficiency with N = 1.0.

may not be gravitationally bound.

A simple argument for the KS relation of N = 1.4 was postulated by several authors (Elmegreen, 1994; Wong & Blitz, 2002; Krumholz & McKee, 2005; Krumholz & Tan, 2007) that a roughly constant fraction of the gas present in molecular clouds will be converted into stars each free-fall time. With $t_{\rm ff} \propto \rho^{-0.5}$, we would expect $\dot{\rho} \propto \rho^{1.5}$ and with an assumption that scale heights of galaxies do not vary significantly we can come to the conclusion that $\Sigma_{\rm SFR} \propto \Sigma_{\rm gas}^{1.5}$. Whilst this free-fall time can explain this N = 1.4, we do find two serious problems with the free-fall theory. Firstly, no evidence has been found in well-studied molecular clouds for collapse at $t_{\rm ff}$ (Zuckerman & Evans, 1974). With these studies showing star formation efficiencies of around 10%, this inefficiency in star formation can not be explained by free-fall collapse. If gas is able to collapse through free-fall, we would see a much higher star formation efficiency. Therefore this efficiency of 10% that is observed can only work if star formation is typically halted by some process; be it external (through supernovae) or internal (through turbulence). Secondly, by simply looking at the free-fall time equation, we see that $t_{\rm ff} \propto 1/\langle\rho\rangle$, and therefore this dependency of the free-fall time on the density of the gas raises the question, how is it possible to calculate a relevant $t_{\rm ff}$ in a cloud. An unknown here is at what density does this gas begin to free-fall, i.e. at what density is the point of no return.

The KS law has since been investigated by Gao & Solomon (2004a,b) using HCN $J = 1 - 0$ line emission (note that we will refer to 'HCN $J = 1 - 0$' simply as

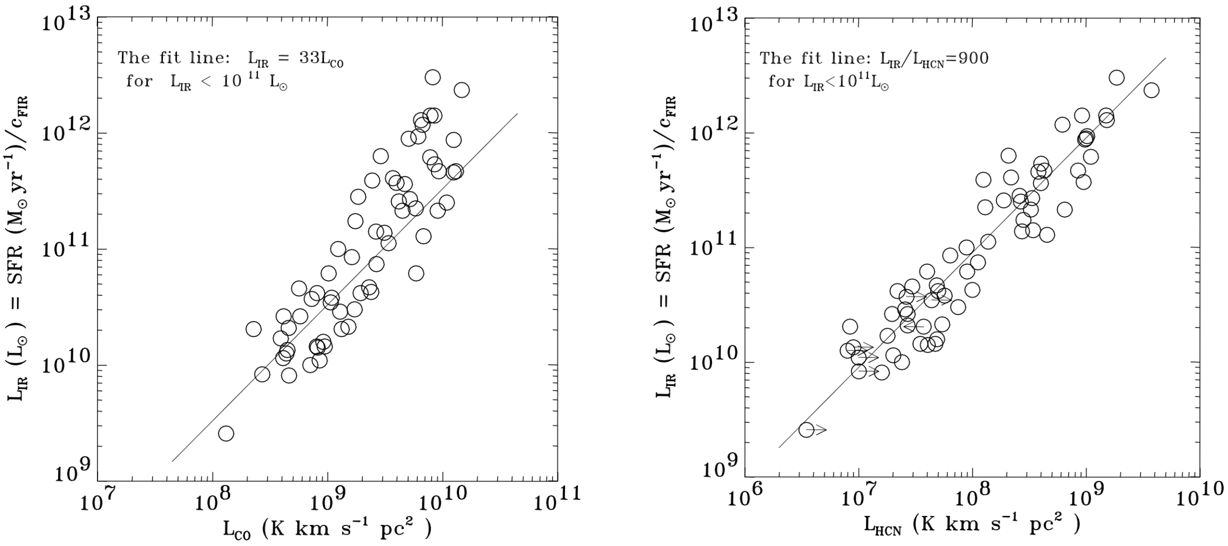

**Figure 1.6.** Figures from Gao & Solomon (2004b) showing the variation in the KS relation between CO as the gas tracer (Figure on the left) and HCN as the gas tracer (Figure on the right).

'HCN' for the rest of the thesis). As Figure 1.6 shows for $L_{FIR} \propto L_{HCN}$, Gao & Solomon (2004b) found a value of N = 1 and that $\Sigma_{SFR} \propto \Sigma_{gas}$. An explanation from Wu et al. (2005) stated that HCN emission from a galaxy simply counts the number of star forming clumps present in these galaxies. This idea was further strengthened by the correlation between the densities that HCN emission traces and the densities that star formation occurs. Research from Lada et al. (2009) and Lada et al. (2010) found that star formation occurs almost exclusively in dense regions of molecular clouds at densities above $\sim 10^4$ to $10^5$ cm$^{-3}$. This finding from Lada et al. (2009) and Lada et al. (2010) ties in with an assumption Gao & Solomon (2004a,b) placed on HCN in that HCN emission traces densities $> 3 \times 10^4$ cm$^{-3}$.

## 1.2 HCN AS A DENSE GAS TRACER

One might expect that because the largest constituent of molecular clouds is molecular hydrogen, $H_2$, that the line emission of $H_2$ would be the most common tool for observers to use to observe molecular clouds. However, $H_2$ line emission is almost impossible to observe due to three reasons; firstly, $H_2$ is symmetric, and thus lacks a permanent dipole moment and the vibrational and rotational transitions are faint because of their quadrupolar origin. The rotational lines occur in the infrared at wavelengths of around 2 $\mu$m Hinkle et al. (2000) and requires temperatures of around 7000K to excite. Secondly, molecular hydrogen can be electronically excited via the Lyman-Werner bands which requires energies of ∼ 11 ev Schauer et al. (2021) corresponding to a temperature of $\sim 10^5$ K emitting in the UV. Lastly, the first excited state of molecular hydrogen is at ∼ 510K Stahler & Palla (2004). Using Table 1.1, we see that the formation of molecular hydrogen occurs when the gas is "cold" ($\sim 50K$) and at a temperature of 510K most of the hydrogen is in atomic form and therefore very little emission stems from molecular hydrogen. This therefore makes $H_2$ a poor tracer of the cold regions of a galaxy.

Instead, different molecules are used to probe different density regimes of the molecular cloud since the detectability of such molecules has some dependence on its critical density. That is the density at which the spontaneous de-excitation of a photon from the initial energy level, i, to a final energy level, k, is equal to the sum of all contributions from collisional excitation and de-excitation rates from the same initial energy level, i, to all possible energy levels. This can be written as,

$$\mathrm{n_{crit}} \equiv \frac{\mathrm{A_{i,k}}}{\sum_{\mathrm{k}} \mathrm{q_{i,k}}} \quad , \tag{1.2}$$

where $\mathrm{A_{i,k}}$ is the Einstein A-coefficient and $\mathrm{q_{i,k}}$ is the collisional rate coefficients (Jansen, D.J.,, 1995).

One can visualise this by finding the critical density of CO J = 1 → 0. Here we use the Einstein A-coefficient for spontaneous emission from the first energy level to the ground state of CO and divide by the summation of the collisional rate coefficients for CO where i in equation 1.2 is always the first energy level (i = 1), and the final energy level, k, is equal to 0, 2, 3, 4, 5 etc. i.e. the summation of one collisional de-excitation rate and several collisional excitation rates for CO (with a cutoff above a k level when $\mathrm{q_{i,k}}$ becomes negligible).

Using equation 1.2, the critical density of carbon monoxide (CO J = 1 → 0 emission line) is calculated to be $4.1 \times 10^2$ cm$^{-3}$. However, it is commonly stated in observational studies that the critical density of CO is $1 \times 10^3$ cm$^{-3}$. This is because most studies only consider the collisional de-excitation rate, $\mathrm{q_{1,0}}$, and not all other collisional excitation rates, $\mathrm{q_{1,>1}}$, that should be considered in the calculation of the critical density of a gas.

Observers also use CO to trace star formation as is shown in the previous section (Section 1.1), since CO is used to detect molecular clouds and molecular clouds are a prerequisite of star formation even though molecules are not needed to form stars, as Glover & Clark (2012a) presents. Research by Lada et al. (2009) and Lada et al. (2010) suggest that star formation occurs in density regions above $\sim 10^4$ cm$^{-3}$ and therefore the use of CO emission to trace star formation is unreasonable. This is also compounded by the research from Goldsmith et al. (2008), Liszt et al. (2010), Pety et al. (2013) and Roman-Duval et al. (2016) that showed CO tracing densities much lower than its critical density and the star formation regions of $\sim 10^4$ cm$^{-3}$, due to the fact that CO is optically thick at these density regimes.

The concept of critical density is only really useful in optically thin regimes. In optically thick regimes, radiative trapping occurs, where light that is emitted from gas such as CO would normally be allowed to escape freely without any further interactions in optically thin regimes instead interacts and excites other CO molecules before it is allowed to escape. This radiative trapping alters the level populations, to approach those in LTE, effectively driving the critical density down below $n_{\rm crit}$. Indeed, Shirley (2015) suggests a new term that can describe the densities that optically thick gas tracers can trace, which is the effective density, $n_{\rm eff}$, which is the density a modest line intensity (1 K km s$^{-1}$ is often used) is observed that is based on radiative transfer calculations with reasonable assumptions about the column density and gas kinetic temperature of the region.

To probe higher densities, one then would be looking for a molecule with a higher critical density. Molecules such as $N_2H^+$ and HCN have been used to trace denser gas in molecular clouds since their critical densities are $n_{\rm crit} \sim 10^5$ cm$^{-3}$ (Jørgensen, 2004) and $n_{\rm crit} \sim 10^6$ cm$^{-3}$ (Dumouchel et al., 2010; Jiménez-Donaire et al., 2017) respectively. Shirley (2015) shows a significant difference between $n_{\rm eff}$ of $8.4 \times 10^3$ cm$^{-3}$ for HCN emission compared to $n_{\rm crit}$ of $4.7 \times 10^5$ cm$^{-3}$, which suggests caution when using $n_{\rm crit}$ instead of $n_{\rm eff}$. Studies from Wu et al. (2005), Krumholz & Tan (2007), Krumholz & Thompson (2007), Wu et al. (2010), Usero et al. (2015), Jiménez-Donaire et al. (2017) and Onus et al. (2018) state that HCN traces densities $> 10^4$ cm$^{-3}$. This along with Shirley (2015) estimate value of $n_{\rm eff}$ of $\sim 10^4$ cm$^{-3}$ has led more and more researchers to use HCN emission as a new standard gas tracer for star formation.

For the analysis produced by Shirley (2015), the radiative transfer code RADEX (van der Tak et al., 2007) was used with a static, uniform density sphere, with the CMB as the only background radiation field. This result of $n_{\rm eff} \sim 10^4\,{\rm cm}^{-3}$ is the density required to produce a line with a strength of 1 K km/s, which is not necessarily the same as the definition of emission-weighted mean density other studies have used. Much like the various definitions of $n_{\rm crit}$, there appears to be no set standard in our definition of $n_{\rm eff}$. This gives us a motivation to try and clarify some sort of standard $n_{\rm eff}$ that can be used for HCN. Generally there seems to be some relation between the critical density and the optical depth, however it is not clear how much contribution the optical depth has on $n_{\rm eff}$. One disadvantage with Shirley (2015)

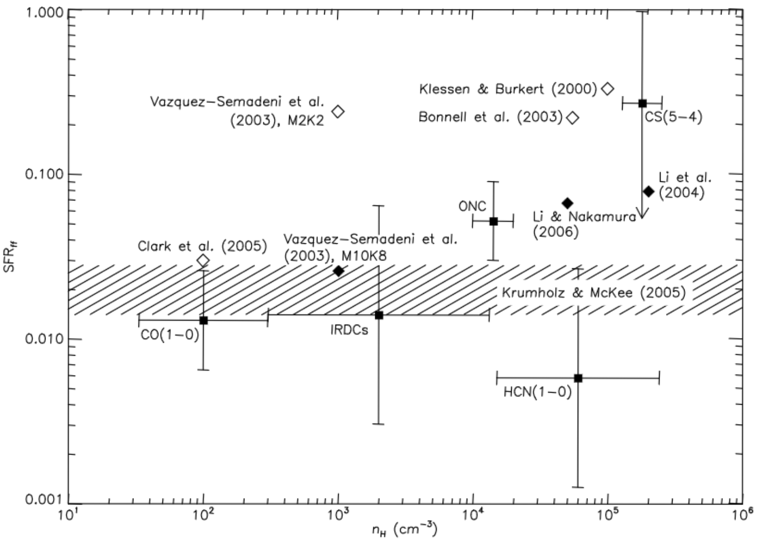

**Figure 1.7.** Figure from Krumholz & Tan (2007) showing the star formation rate per free-fall time according to different gas tracers.

is that there is no consideration that the density in molecular clouds follows some probability distribution function (PDF), which would realistically follow a lognormal distribution and not a delta function (Mac Low & Klessen, 2004; Elmegreen & Scalo, 2004).

Contrary to other observational studies that show HCN emission tracing densities above $10^4\,\mathrm{cm}^{-3}$, Pety et al. (2017), Kauffmann et al. (2017) and Barnes et al. (2020) have shown that HCN also traces diffuse regions of molecular clouds at a density of $\sim 500\,\mathrm{cm}^{-3}$, $\sim 10^3\,\mathrm{cm}^{-3}$ and $\sim 10^3\,\mathrm{cm}^{-3}$ from the three papers respectively. These findings have serious implications on observational results that use HCN as a dense gas tracer, with results such as observed mass estimates of star forming regions being reliant on the observed radius that is dependent on the density of $10^4$ cm$^{-3}$ that observers use. A lower density of $10^3$ cm$^{-3}$ would imply that an observed radius for a density region above $10^4$ cm$^{-3}$ would lie within the observed region and that observers are overestimating the observed mass of star forming regions.

This lower density threshold for HCN also has implications with the star formation rate derived in Krumholz & Tan (2007) who state that HCN traces densities $\sim 6 \times 10^4$ cm$^{-3}$ and that this implies that star formation is “slow”, in the sense that only a small percentage of gas forms stars every free-fall time. Shown in Figure 1.7 is the star formation rate per free-fall time according to different gas tracers with HCN being an outlier giving this suggestion of “slow” star formation. This much lower density of $10^3$ cm$^{-3}$ for HCN will undoubtedly “speed up” the star formation rate and shifting their HCN data point towards the trend of Figure 1.7. This higher star formation rate and lower threshold density directly contradicts the conclusions made by Krumholz & Tan (2007). However, like all observations that try to find a 3 dimensional property, there must be some assumptions and uncertainties when these observations of column densities are subject to some conversion model to determine volume density. The findings from Pety et al. (2017), Kauffmann et al. (2017) and Barnes et al. (2020) therefore gives us motivation to investigate HCN, particularly to see whether or not these observations of $\sim 10^3\,\mathrm{cm}^{-3}$ have any validity and to provide some clarity to observers as to what exactly HCN is tracing in terms of density.

## 1.3 CHEMICAL MODELING

The chemical processes in the ISM, particularly in molecular clouds, are hugely important, since not only are these fundamental for observers to observe these molecular cloud regions, they are also incredibly important in the heating and cooling processes of the ISM (discussed in further details in Section 2.1.9). Therefore, there has been a great amount of effort in modelling these chemical processes, since these are these are the basis of synthetic observations and provide the ability to give an accurate description of where these molecules are really formed in molecular clouds. However, one of the biggest difficulties with chemical modelling is the complexity of such models. For example, the UMIST database contains over 2000 chemical reactions (Woodall et al., 2007). This is typically overcome by creating simplistic models that approximate reactions and often exclude complex reactions with a particular molecule such as Nitrogen. Chemical modelling usually involves solving a set of ordinary differential equations (ODE) and the computational time is related to $N^3$, where N is the number of species contained in the chemical models.

Some of the first chemical modelling was done by Hollenbach et al. (1971); Jura (1974); Glassgold & Langer (1975) and Black & Dalgarno (1977) through photodissociation regions (PDR) modeling, specifically with steady state models for the transitions from H to $H_2$ and from $C^+$ to CO. Jumping forward to the 2000s and we get reliable chemical models of the ISM, which include highly complex chemical models. Through the work of both Bergin et al. (2004) and Hosokawa & Inutsuka (2006), different methods to accurately model chemical abundances such as $H_2$ and CO within GMCs were produced. Although these chemical models are accurate they have their drawbacks, mainly that these models are restricted to one-dimensional zone models.

As previously mentioned, an approach to dealing with such complex chemical modelling is through simplification of the modelling. This is often done through a so called reduced chemical network approach. By taking a select set of limited chemical reactions, and creating a network of these limited reactions, it can greatly reduce the computational cost without limiting the modelling power of the chemical network (Nelson & Langer, 1999; Gong et al., 2017). The biggest advantage to this approach is that the chemistry can be modelled within hydrodynamical codes such as Zeus-mp (Norman, 2000; Glover & Jappsen, 2007). Indeed, the work by Glover & Jappsen (2007) was the first to introduce a chemical network into a hydrodynamical code, where the hydrogen chemistry was followed through several different reactions of ionized, atomic and molecular hydrogen (8 reactions in total). The work by Glover & Jappsen (2007) was specifically looking into the formation of $H_2$ with their motivation being that transient clouds are predominantly made up of $H_2$ and that the formation timescale of $H_2$ can be equated to $t_{\rm form} \simeq 10^9\,{\rm yr/n}$ (Hollenbach et al., 1971), which suggests that in gas with a mean number density $\sim 100$ cm$^{-3}$, characteristic of most giant molecular clouds (Blitz & Shu, 1980), molecular clouds should form at timescales of $\sim 10$ Myr. However, studies such as Hartmann et al. (2001) and Mac Low & Klessen (2004) suggest rapid formation of molecular clouds on the timescale of only a few Myrs. By modelling the formation of $H_2$ in a turbulent molecular cloud simulation, Glover & Mac Low (2007) showed that in a turbulent ISM with the presence of shocks, the formation timescale of $H_2$ drastically reduces to the same timescales suggested by Hartmann et al. (2001) and Mac Low & Klessen (2004).

Modelling $H_2$ alone is typically not something that observers are interested, since they can not observe the emission of $H_2$. However, they can observe CO and therefore producing a theoretical model that follows the formation and destruction of CO is of great importance to observers. Glover et al. (2010) evolved the hydrogen chemical network developed by Glover & Jappsen (2007) to involve helium, carbon and oxygen reactions such that the formation and destruction of CO could be followed. The introduction of these three new gas species drastically increased the amount of reactions in the network from 8 to 218 reactions, therefore it is easy to see that introducing new gas species can make these chemical networks to computationally demanding since each network follows the $N^3$ law.

Research by Glover & Clark (2012b) showed that a simplified chemical network produced by Nelson & Langer (1999) (NL99) reproduces the CO abundance in more complicated models of Glover et al. (2010), and therefore recommend the NL99 network for simulating CO formation. The latest chemical model produced to follow the formation and destruction of CO was that of Gong et al. (2017), who produced a chemical network that improved upon NL99. Their chemical network was shown to improve the accuracy of CO abundance in particular the abundance of CO at densities of $100 - 500$ cm$^{-3}$ with a realistic cosmic-ray ionization rate of $2 \times 10^{-16}$ s$^{-1}$H$^{-1}$ (Indriolo et al., 2007; Hollenbach et al., 2012) compared to NL99 that significantly underproduces CO abundance in the same regime.

Another approach to chemical modelling is through following the chemical evolution and excitation states rather than dynamical evolution of the gas. Using this approach Bisbas et al. (2015) was able to model chemical evolutions while accounting for attenuation of the UV field from arbitrary sources as well as photodissociation and photoionization effects. An accurate treatment of chemical abundances from chemical modelling can give us the opportunity to produce and study synthetic observations of these gas tracers in molecular cloud environments.

## 1.4 Synthetic observations of HCN

Although observationally HCN is becoming a popular tracer, there is a distinct lack of studies of HCN through theoretical modelling. Therefore, there is scope to research into HCN through theoretical modelling because there is an ability to uncover the unknowns of HCN through observations. In this section we present a few studies of synthetic observations of HCN.

Krumholz & Thompson (2007) investigated how the KS law changes with differing molecular gas tracers with HCN being one of three molecular gas tracers investigated (Gao & Solomon, 2004a,b; Gao et al., 2007; Nguyen et al., 1992; Riechers et al., 2006). Similar to Gao & Solomon (2004b), the model uses an LVG calculation but with the inclusion of a lognormal PDF for the density in the molecular gas in their model. In their LVG calculation, a homogeneous sphere with a uniform Maxwellian velocity distribution was implemented to create a simple analytical model that can calculate the escape probabilities, $\beta_{ij}$. Their model showed strong correlation with the observed data with a direct proportionality between far infrared luminosity and HCN luminosity. Their model suggests that HCN emission generally traces dense gas, $\mathrm{n}_{\mathrm{dense}} \sim 10^5$ cm$^{-3}$.

Leroy et al. (2017) highlights the problem with using HCN emission to trace "dense" gas in extragalactic studies by stating that HCN can emit below the critical density with varying effectiveness from optical depths and temperatures. Leroy et al. (2017) states that "if low density regions outnumber higher density regions, then they may contribute appreciably to, or even dominate, emission from that molecule" and therefore tries to pinpoint at what densities HCN starts to dominate. Using the one-zone non-LTE code RADEX van der Tak et al. (2007) to calculate the emissivity, $\epsilon$, of gas across a range of n($H_2$), $T_{kin}$ and $\tau$. For the density, they used two density distributions: a pure lognormal and a lognormal distribution that exhibits a power law tail at high densities, both distributions are commonly used as a reasonable description of the cold, turbulent gas that produces low-J mm-wave line emission. Through their modelling they suggest that HCN emission generally traces densities of $n_{dense} \sim 10^4 - 10^5$ cm$^{-3}$ depending on the density distribution.

Onus et al. (2018) improved on previous theoretical work on HCN through the use of the same high-resolution simulations used in Federrath (2015). These simulations are based on magnetohydrodynamics (MHD) with adaptive mesh refinement code FLASH (Fryxell et al., 2000; Dubey et al., 2008), to create a more realistic stochastic environment rather than some uniform density or a prescribed PDF. Four simulations of increasing physical complexity were made using FLASH that were then post-processed with DESPOTIC using several different HCN emission models resulted in finding that HCN emission traces gas with a luminosity-weighted mean density of $0.8 - 1.7 \times 10^4\,\mathrm{cm}^{-3}$. The limitation of this study is the absence of chemical evolution and associated detailed heating and cooling effects through radiative transfer in FLASH. Therefore, the two key inputs of DESPOTIC which is the HCN abundance and temperature are not accurately self-consistently calculated. Also the choice of implementing a periodic boundary condition on a small 8pc$^3$ section of a molecular cloud is unrealistic, as real clouds are not periodic. It is therefore unclear how representative this is of behaviour of real GMCs.

It is clear that there is a disconnect between the observational studies of HCN produced by Pety et al. (2017), Kauffmann et al. (2017) and Barnes et al. (2020) which show HCN tracing gas at $\sim 10^3$ cm$^{-3}$ and the theoretical studies of HCN that show that HCN traces gas at $10^4 - 10^5$ cm$^{-3}$. This gives us motivation to improve on the previous theoretical studies of HCN with an improved hydrodynamical code with a more accurate chemical model.

## 1.5 Thesis Outline

This thesis investigates HCN as a dense gas tracer in various molecular cloud environments and probe whether or not the research done by Pety et al. (2017), Kauffmann et al. (2017) and Barnes et al. (2020) in that HCN is a more diffuse gas tracer than originally thought holds any truth. This thesis is presented as follows:

- In Chapter 2, we discuss the algorithms and adaptations of the numerical code that we use to model the molecular clouds environments.

- In Chapter 3, we present our simulations of the molecular cloud environments, describing in detail the initial conditions of the cloud properties and the variations in the select parameters to produce the variations required to robustly test our hypothesis.
- In Chapter 4, we present our synthetic observations of HCN that were produced from simulations of varying initial cloud-cloud collisional velocities.
- In Chapter 5, we present our synthetic observations of HCN that were produced from simulations of varying interstellar radiation field strength and cosmic ray ionization rates.
- In Chapter 6, we summarise the main conclusions drawn from this work and discuss our future plans.

# CHAPTER 2
# NUMERICS

This chapter describes the numerical codes and numerical techniques used to produce the results in this thesis. The simulations performed in this thesis were run using existing codes, and the science goals did not required these to be modified in any way. For completeness and to put the rest of the thesis in context I describe them in detail here. All the coding work in this thesis was associated with the data reduction and analysis that is presented in Chapters 3, 4, 5 and 6.

## 2.1 AREPO

The ISM is a fluid and therefore in order to do study the ISM through numerical simulations, we need to use a hydrodynamical code. To study the dynamics of the molecular clouds we use AREPO, which is a moving mesh hydrodynamical code produced by Springel (2010). Most hydrodynamical codes can be split up into several different physical equations and techniques, and therefore, in order to understand AREPO, we have split the code into the most important aspects that are required to get the dynamics and physical properties of the ISM.

### 2.1.1 BASIC FLUID APPROACH

Firstly, we have to look at the most basic fundamentals of the hydrodynamical code before delving into the the added complexities inside AREPO that paint a more accurate picture of the ISM. In almost all cases of astrophysical modelling, we deal with an ideal gas, and therefore use the ideal gas equation of state. An ideal gas can be described as collisions between atoms or molecules that are perfectly elastic and in which there are no inter-molecular attractive forces, and can be written in as,

$$\mathrm{PV} = \mathrm{Nk_BT} \quad , \tag{2.1}$$

where P is the pressure of the gas, V is the volume in which the gas is contained, N is the number of particles that make up the gas, $k_B$ is the Boltzmann constant and T is the temperature of the gas.

The motion of the gas is governed entirely by conservation laws; the conservation of matter, the conservation of momentum and the conservation of energy. These are presented in the form of the following equations,

$$\frac{\partial \rho}{\partial \mathrm{t}} + \nabla \cdot (\rho \mathbf{v}) = 0 \quad , \tag{2.2}$$

$$\rho \frac{\partial \mathbf{v}}{\partial \mathrm{t}} + \rho(\mathbf{v} \cdot \nabla \mathbf{v}) + \nabla \mathrm{P} = 0 \quad , \tag{2.3}$$

$$\frac{\partial \epsilon}{\partial \mathrm{t}} + \mathbf{v} \cdot \nabla \epsilon + \frac{\mathrm{P}}{\rho} \nabla \cdot \mathbf{v} = 0 \quad . \tag{2.4}$$

These are the equations of matter, momentum and energy respectively; where $\rho$ is the density of the gas, $\mathbf{v}$ is the velocity of the gas and $\epsilon$ is the specific internal energy of the gas.

They can also be written in compact form, which will become very useful for our introduction of magnetic fields into our simulations (see Section 2.1.5),

$$\frac{\partial \mathbf{U}}{\partial \mathrm{t}} + \nabla \cdot \mathbf{F} = 0 \quad , \tag{2.5}$$

where $\mathbf{U}$ is the state vector that describes the fluid and $\mathbf{F}$ is the flux function of the state vector,

$$\mathbf{U} = \begin{pmatrix} \rho \\ \rho \mathbf{v} \\ \rho e \end{pmatrix} \quad , \tag{2.6}$$

$$\mathbf{F}(\mathbf{U}) = \begin{pmatrix} \rho \mathbf{v} \\ \rho \mathbf{v} \mathbf{v}^T + P \\ (\rho e + P)\mathbf{v} \end{pmatrix} \quad . \tag{2.7}$$

Here $e = u + \frac{1}{2}\mathbf{v}^2$ is the total energy per unit mass and u denoting the thermal energy per unit mass.

For the ISM, we assume that the gas evolves adiabatically and therefore we use the hydrostatic equilibrium for a general polytropic equation of state, which can be written as the following,

$$P = K\rho^{\gamma} \quad , \tag{2.8}$$

where K is the adiabatic constant and $\gamma$ is the adiabatic index which is governed by the degrees of freedom a particle can have in the gas. In our case for the ISM, we treat $\gamma = 5/3$.

### 2.1.2 Voronoi Mesh

To be able to evolve the gas we must use numerical methods that solve these equations with respect to time. The two main numerical approaches for solving these equations are Eulerian and Lagrangian. The Lagrangian method is one that divides the fluid into a set of discrete moving elements, referred to as particles. The particles evolve through moving and interacting with other particles as if on a boat in a river. All smooth particle hydrodynamical (SPH) codes such as GADGET (Springel et al., 2001) and GADGET-2 (Springel, 2005) use the Lagrangian method. The Eulerian method is one that partitions the gas into a fixed grid of cells where the gas evolve by fluxing their physical properties from one cell to another neighbouring cell. All adaptive mesh refinement (AMR) codes such as RAMSES (Teyssier, 2002) and FLASH (Fryxell et al., 2000) use the Lagrangian method. Arepo use a combination of both Lagrangian and Euler methods in the form of a moving mesh, specifically a moving unstructured mesh defined by the Voronoi tessellation of a set of discrete points.

An example of such mesh in 2D can be seen in Figure 2.1. In 3D, one can think of forming a Voronoi mesh by dispersing a set of discrete points into a box and inflating each point like a balloon until each skin of the balloon meets the skin of their neighbouring inflated points. Even though this is a good conceptual method of understanding how a Voronoi mesh is generated, Arepo does a different method of generating its Voronoi mesh.

It first inserts these discrete points into a box such that a Delaunay tessellation is possible. A Delaunay tessellation is a triangulation of the plane, where the points serve as vertices of the triangles. An example of a Delaunay tessellation is shown in Figure 2.2, which is used to produce the same Voronoi tesselation as Figure 2.1. In Figure 2.3, we see how the Delaunay tessellation forms the basis to the generation of the Voronoi tessellation. The Voronoi tessellation and the Delaunay tessellation intercepts perpendicularly to one another.

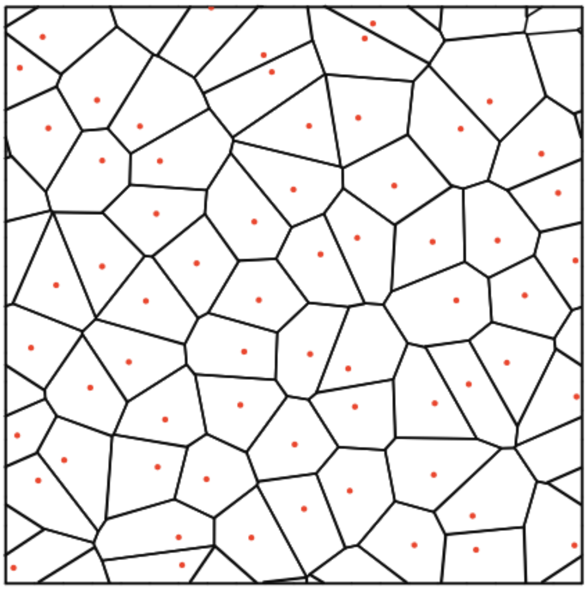

**Figure 2.1.** Diagram taken from Springel (2010) showing an example of a Voronoi tessellation in 2D with periodic boundary conditions.

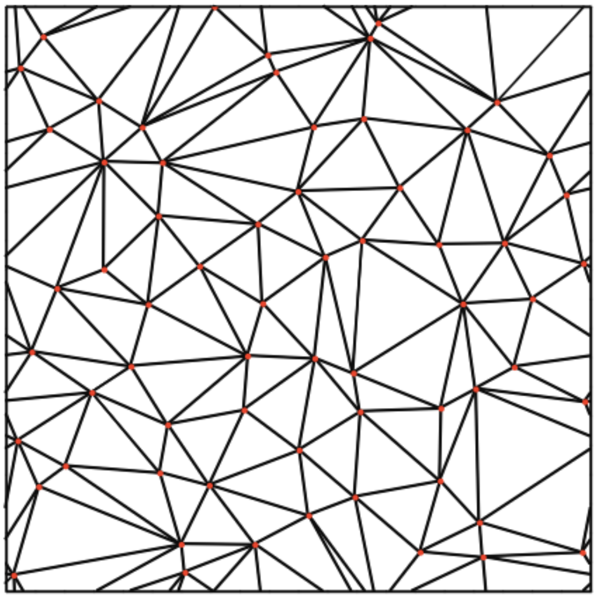

**Figure 2.2.** Diagram taken from Springel (2010) showing an example of a Delaunay tessellation in 2D with periodic boundary conditions.

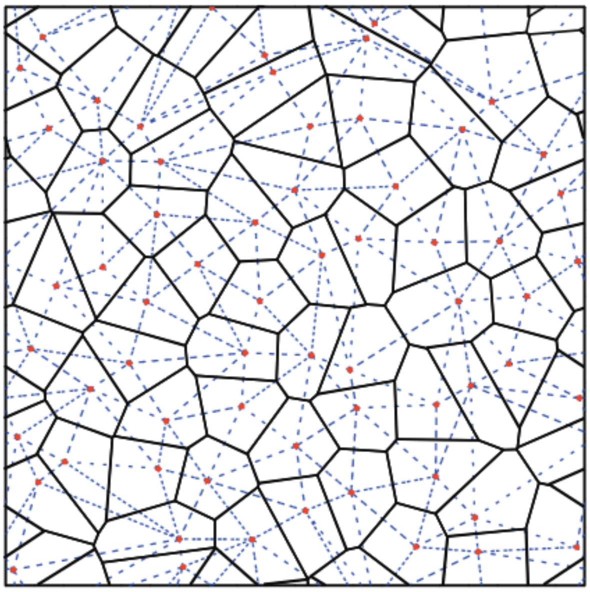

**Figure 2.3.** Diagram taken from Springel (2010) showing a figure showing how the Delaunay tessellation (the same tessellation as Fig. 2.2) leads to the generation of the Voronoi tessellation (the same tessellation as Fig. 2.1) (the solid lines show the Voronoi and the dashed lines the Delaunay tessellation).

### 2.1.3 Mesh Refinement

One of the main advantages of an unstructured mesh is the ability to refine and de-refine cells, i.e. split and merge cells. This results in the ability to have very high resolutions in regions where it is needed the most and have very coarse resolution in regions of little interest.

This process is much better explained by presenting a picture which we show in Figure 2.4. We first explain the refinement process that occurs in Arepo.

If we want to increase the resolution in a particular region we need to have a refinement process, this is done by placing a new mesh-generating point at *almost exactly* the same location as the original point of the cell. This minimizes any changes to the structure of the surrounding cells. The conserved quantities of the original cell, $\mathbf{U}$, are distributed among the two halves by weighting with the relative fractions of the volumes occupied by the two new cells.

A de-refinement strategy where a cell is dissolved by simply removing its mesh-generating point from the tessellation is implemented into the code. This means that the volume of the removed cell will be absorbed by the neighbouring Voronoi cells, illustrated in Figure 2.4. Arepo then distributes the conserved fluid quantities, $\mathbf{U}$, of the dissolved cell among these neighbouring cells, in proportion to the claimed volume fractions.

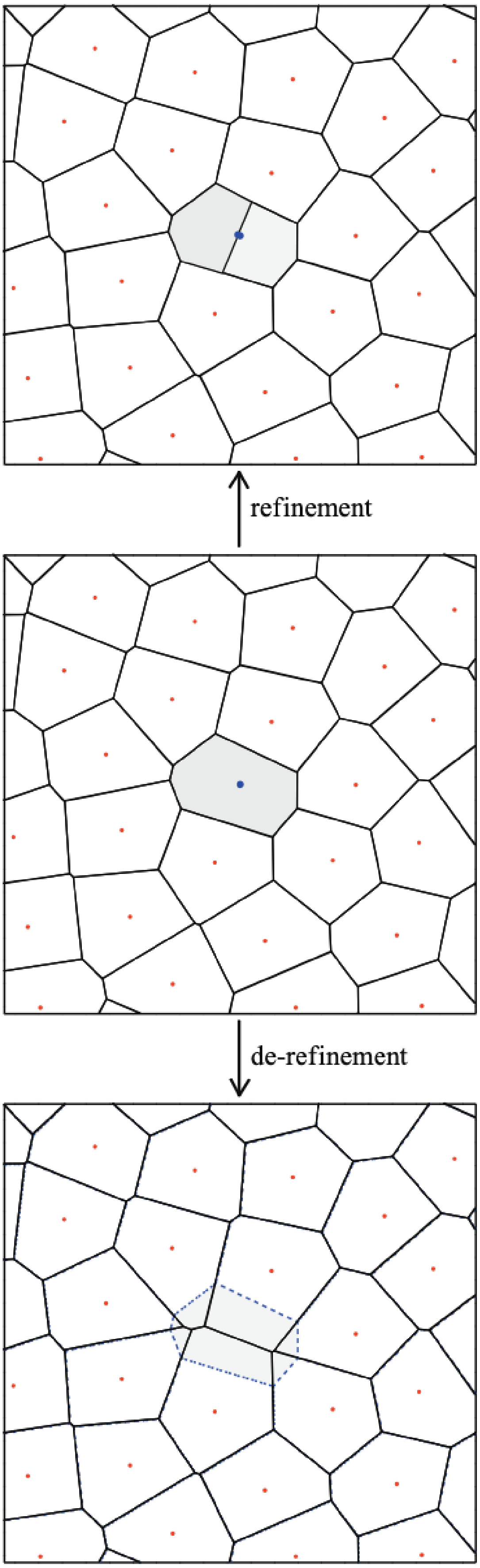

**Figure 2.4.** Diagram taken from Springel (2010) showing the refinement and de-refinement processes.

### 2.1.4 FINITE VOLUME

Now that the mesh has been constructed, we have the ability to describe how the gas moves from one Voronoi cell to another neighbouring cell. This is done through the *finite-volume* strategy, where the Voronoi cells serve as the discretization of the system's volume. The state of the fluid is described by the cell averages of the conserved quantities for those cells. We can define the cells' mass, $m_i$, momentum, $\mathbf{p}_i$, and energy, $E_i$, through integrating the state vector $\mathbf{U}$ with respect to volume, dV, for cell i,

$$\mathbf{Q}_\mathrm{i} = \begin{pmatrix} m_i \\ \mathbf{p}_i \\ E_i \end{pmatrix} = \int_{V_i} \mathbf{U}\, dV \quad . \tag{2.9}$$

In order to calculate how much of $Q_i$ moves into a neighbouring cell j, we can use equation 2.5 to calculate the rate of change in $Q_i$. Using Gauss' theorem to convert the volume integral over the flux divergence into a surface integral over the cell we can get,

$$\frac{\mathrm{d}\mathbf{Q}_\mathrm{i}}{\mathrm{dt}} = -\int_{\partial \mathrm{V_i}} [\mathbf{F}(\mathbf{U}) - \mathbf{U}\mathbf{w}^\mathrm{T}]\, \mathrm{d}\mathbf{n} \quad , \tag{2.10}$$

where $\mathbf{w}$ is the velocity at which the cell boundary between two cells moves, which is visualised in Figure 2.5, $\mathbf{n}$ is the normal vector of the volumetric cell surface.

An interesting feature that arises from equation 2.12 is that if $\mathbf{w} = 0$, we get a fully Eulerian treatment of the flux since the mesh is taken to be static. If $\mathbf{w} = \mathbf{v}$, we get a fully Lagrangian approach since the surface would be allowed to move at every point with the local flow velocity.

We can then use Figure 2.5 to show how the gas in cell i is fluxed over to cell j using equation 2.12. If we take the red line in Figure 2.5 to be a flat polygonal face with Area, $A_{ij}$, that divides cell i and cell j. Then we can define the averaged flux across the face i-j as,

$$\mathbf{F}_\mathrm{ij} = \frac{1}{\mathrm{A_{ij}}} \int_{\mathrm{A_{ij}}} [\mathbf{F}(\mathbf{U}) - \mathbf{U}\mathbf{w}^\mathrm{T}]\, \mathrm{d}\mathbf{A_{ij}} \quad , \tag{2.11}$$

where $\mathbf{F}_{ij}$ is the averaged flux across the face i-j and $d\mathbf{A_{ij}}$ is the partial derivative of the area vector facing the direction of cell j from cell i.

The average flux across all faces of the cell can then be quantified by,

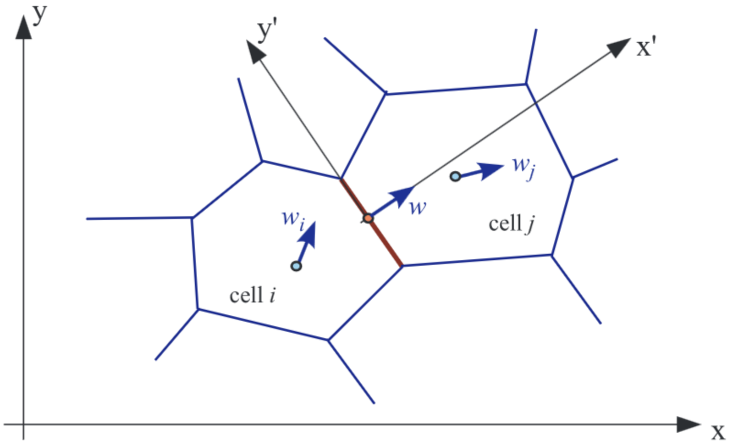

**Figure 2.5.** Diagram taken from Springel (2010) showing how the properties of cell i is fluxed into cell j.

$$\frac{\mathrm{d}\mathbf{Q}_\mathrm{i}}{\mathrm{dt}} = -\sum_\mathrm{j} \mathrm{A}_\mathrm{ij}\mathbf{F}_\mathrm{ij} \quad . \tag{2.12}$$

The conservation of the physical properties that are fluxed from cell to cell is not exactly conserved in an unstructured mesh, which is evidently a problem for AREPO. Godunov & Bohachevsky (1959) first produced an exact Riemann solver, which is a method by which time-averaged fluxes of all conserved quantities are calculated at cell interfaces, effectively solving the problem of conserving these quantities. An exact Riemann solver is computationally very expensive and thus most hydrodynamical codes use approximate Riemann solvers. AREPO uses a collection of Riemann solvers depending on if we include anything that effects the *finite-volume* equations such as self-gravity or magnetic fields . Our inclusion of both self-gravity and magnetic fields in our simulations require us to use Harten-Lax-van Leer with contact and Alfven mode (commonly referred to HLLD) (Miyoshi & Kusano, 2005).

### 2.1.5 MAGNETIC FIELDS

The inclusion of magnetic fields into AREPO was introduced by Pakmor et al. (2011). We first reintroduce equation 2.6 but here we include a magnetic field, **B**, into the state vector,

$$\mathbf{U} = \begin{pmatrix} \rho \\ \rho\mathbf{v} \\ \rho e \\ \mathbf{B} \end{pmatrix} \quad . \tag{2.13}$$

Here, the total energy per unit mass is changed to include the influence from the magnetic field, to $e = u + \frac{1}{2}\mathbf{v}^2 + \frac{1}{2\rho}\mathbf{B}^2$.

The flux function $F(\mathbf{U})$ becomes,

$$\mathbf{F}(\mathbf{U}) = \begin{pmatrix} \rho\mathbf{v} \\ \rho\mathbf{v}\mathbf{v}^T + p - \mathbf{B}\mathbf{B}^T \\ (\rho e + p)\mathbf{v} - \mathbf{B}(\mathbf{v}\cdot\mathbf{B}) \\ \mathbf{B}\mathbf{v}^T - \mathbf{v}\mathbf{B}^T \end{pmatrix} \quad . \tag{2.14}$$

Here, $p = P + \frac{1}{2}\mathbf{B}^2$ is the total gas pressure.

If $\mathbf{B} = 0$, these equations (2.13 and 2.14) reduce back down to equations presented in Section 2.1.1 (2.6 and 2.7).

A problem arises from the use of the *finite-volume* method, similar to the Riemann solver problem, the *finite-volume* can not preserve $\nabla \cdot \mathbf{B} = 0$ in an initially divergence free field. There is an error propagation of $\nabla\cdot\mathbf{B}$ that grows as it propagates through the cells. Therefore a cleaning technique is needed to regain a divergence-free magnetic field at any time. In AREPO, the Dedner cleaning technique (Dedner et al., 2002) is used which adds an additional conserved scalar, $\psi$, (which is related to the divergence of the magnetic field) to both equations 2.13 and 2.14 to diffuse away the error as soon as it appears. Therefore both equations 2.13 and 2.14 are changed to give,

$$\mathbf{U} = \begin{pmatrix} \rho \\ \rho\mathbf{v} \\ \rho e \\ \mathbf{B} \\ \psi \end{pmatrix} \qquad \mathbf{F}(\mathbf{U}) = \begin{pmatrix} \rho\mathbf{v} \\ \rho\mathbf{v}\mathbf{v}^T + p - \mathbf{B}\mathbf{B}^T \\ (\rho e + p)\mathbf{v} - \mathbf{B}(\mathbf{v}\cdot\mathbf{B}) \\ \mathbf{B}\mathbf{v}^T - \mathbf{v}\mathbf{B}^T + \psi \\ c_h^2\mathbf{B} \end{pmatrix} \quad , \tag{2.15}$$

where $c_h$ is a positive constant. The scalar quantity is allowed to decay exponentially in the time integration process through the use of the following,

$$\frac{\partial\psi}{\partial \mathrm{t}} = -\frac{\mathrm{c_h^2}}{\mathrm{c_p^2}}\psi \quad , \tag{2.16}$$

where $c_p$ is a second positive constant.

To further the stability of the advection of $\nabla \cdot \mathbf{B}$, Pakmor & Springel (2013) also included the Powell approach for divergence control (Powell et al., 1999). In this scheme, additional source terms are introduced into the momentum equation, induction equation and energy equation. These source terms add a passive advection of $\nabla \cdot \mathbf{B}/\rho$ with the flow of the gas to counteract further growth of local $\nabla \cdot \mathbf{B}$ errors.

### 2.1.6 SELF GRAVITY

By including a gravitational field to our simulation, equation 2.5 is changed to,

$$\frac{\partial \mathbf{U}}{\partial \mathrm{t}} + \nabla \cdot \mathbf{F} = \begin{pmatrix} 0 \\ -\rho\nabla\Phi \\ -\rho\mathbf{v}\nabla\Phi \\ 0 \\ 0 \end{pmatrix} \quad , \tag{2.17}$$

where $\Phi$ is the gravitational potential.

The gravitational potential can be described by some external gravitational field such as a neighbouring black hole or by the self-gravity of the molecular gas. In our case we have the latter case and therefore describe the self-gravity of the gas as a solution of Poisson's equation,

$$\nabla^2\Phi = 4\pi \mathrm{G}\rho \quad , \tag{2.18}$$

where G is the universal gravitational constant.

We can define the total gravitational energy between cell i and cell j as,

$$\mathrm{E_{pot}} = \frac{1}{2}\sum_{\mathrm{ij}} \mathrm{Gm_i m_j}\phi(\mathrm{r_{ij}}) \quad , \tag{2.19}$$

where $\phi(r_{ij})$ describes the gravitational interaction kernel between two cells.

If the distance between two cells is very small, we have a problem where we can potentially be introducing artificial two-body interactions between the two cells. To avoid this we can introduce a gravitational softening of radius, h. AREPO has many methods of approaching the use of the gravitational softening. Here we use an adaptive gravitational softening method where each cell "sees" an individual softening length based on their cell radius. The radius of a cell is multiplied by a variable scaling factor. The closest softening length from a logarithmically spaced table of possible softening lengths is then adopted for the cell. We can formulate this in the from of,

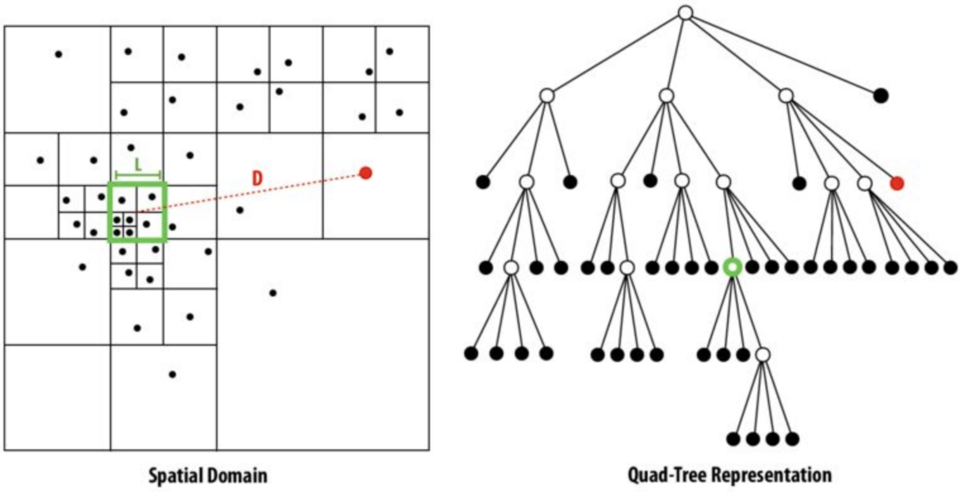

**Figure 2.6.** Diagram of the Barnes–Hut oct-tree algorithm.

$$\phi(\mathrm{r_{ij}}) = -\frac{1}{f_h \mathrm{r_{cell}}} \quad , \tag{2.20}$$

where $f_h$ is a variable scaling factor that was chosen to be a value of 2 for all simulations.

This gravitational softening length only comes into effect when the distance between two cells is less than 2.8 $\epsilon_{\mathrm{soft}}$ where $\epsilon_{\mathrm{soft}} = f_h \mathrm{r_{cell}}$, otherwise AREPO uses conventional Newtonian mechanics.

It would almost be computationally impossible for AREPO to calculate the net gravitational forces exerted on a particular cell by individually calculating the gravitational forces between it and all other cells in the simulation, and repeat this for all other cells in the simulations for each time-step. We can avoid this by implementing an Barnes–Hut (Barnes & Hut, 1986) oct-tree algorithm, shown visually in Figure 2.6.

### 2.1.7 SINK PARTICLES

The implementation of self-gravity in AREPO results in the ability for the gas in our simulations to form regions of densities high enough to undergo runaway gravitational collapse. At the end of this gravitational collapse is a star and in terms of AREPO would be a very small and incredibly dense cell that would slow down the computational time immensely, therefore we have a problem that must be overcome without restricting the possibility of gas in the cells from forming stars. We therefore introduce sink particles into our simulations (Bate et al., 1995). These sink particles do not behave like cells and instead are independent from the influences of the cells, instead they behave like rubber ducks in a river. Therefore they follow the dynamics of the star and also have the ability to have the gas from the neighbouring cells be accreted onto the sink particles. In our simulations, several conditions must be met for a gas cell to be turned into a sink particle, which follows the criteria laid out in Federrath et al. (2010). First, the candidate cell must be above a sink creation density, $n_{SC}$, that we may define as a variable parameter and be a local minimum in the gravitational potential. Also the gas within the sink accretion radius, $\mathrm{r}_{\mathrm{sink}}$, must be gravitationally bound, and both moving towards *and* accelerating towards the candidate's location – that is, the mass-weighted $\nabla \cdot \mathbf{v}$ and $\nabla \cdot \mathbf{a}$ within the sink creation radius must be negative.

### 2.1.8 TIME INTEGRATION

AREPO uses an explicit time integration method. This puts a constraint on the size of the local time-step that we can have in our time integration in order to maintain accuracy and stability. This is defined as the local Courant–Friedrichs–Levy (CFL) time-step criterion, which is written as,

$$\Delta \mathrm{t} \leq \mathrm{C}_{\mathrm{CFL}} \frac{\mathrm{r}_{\mathrm{cell}}}{\mathrm{v}_{\mathrm{signal}}} \quad , \tag{2.21}$$

where the Courant factor $\mathrm{C}_{\mathrm{CFL}}$ is a variable parameter, $\mathrm{r}_{\mathrm{cell}}$ is the cell radius and $\mathrm{v}_{\mathrm{signal}}$ is the signal speed and is characterised by the fastest mode that information can travel, and therefore we must consider both the sound speed and the Alfvén speed,

$$\mathrm{v}_{\mathrm{signal}} = \left( \gamma \frac{\mathrm{p}}{\rho} + \frac{\mathbf{B}^2}{\rho} \right)^{\frac{1}{2}} \quad . \tag{2.22}$$

The inclusion of self-gravity means we adopt a criterion for gravitational acceleration,

$$\Delta \mathrm{t} \geq \sqrt{\frac{2\mathrm{C}_{\mathrm{grav}} \epsilon_{\mathrm{soft}}}{|\mathbf{a}|}} \quad , \tag{2.23}$$

where $\mathrm{C}_{\mathrm{grav}}$ is a variable parameter that we may input into the code. For all simulations the Courant factor $\mathrm{C}_{\mathrm{CFL}}$ and $\mathrm{C}_{\mathrm{grav}}$ where chosen to be 0.5 and 0.05 respectively.

To allow for as large a time-step as possible AREPO uses a power-of-two time-step hierarchy where the total simulation time is subdivided into $2^{\mathrm{N}}$ equal steps. In all of our simulations N is set to 32. The voronoi cells are then associated with the

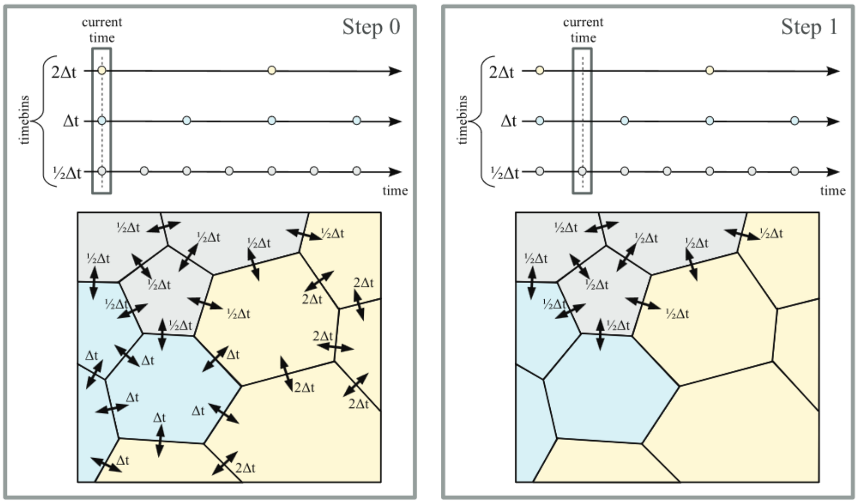

**Figure 2.7.** Diagram taken from Springel (2010) showing how AREPO does its power-of-two time-step hierarchy in that it first evolves all three Δt, and then in the next time-step only evolves 1/2Δt.

time bin that corresponds to the largest time step that is just smaller than the most restrictive time step constraint from gravity and MHD. Transitioning to a shorter time step is always possible, but changing to a longer time step only occurs if the current time is synchronized with the target time bin. Figure 2.7 shows how AREPO approaches this power-of-two time-step hierarchy, in that it first evolves all three Δt, and then in the next time-step only evolves 1/2Δt and would then only evolve 1/2Δt and Δt and not 2Δt.

The gravitational time integration is done with a second-order accurate leapfrog scheme, expressed through alternating "drift" (which modify the positions) and "kick" (which modify the velocities) operations.

The time integration of the hydrodynamic quantities is described in Pakmor et al. (2016), where the implementation of MUSCL-Hancock scheme is used (van Leer, 1984; Toro, 1997), which has been shown to provide second-order accuracy in time and space.

### 2.1.9 HEATING AND COOLING

The heating and cooling processes in the ISM plays a vital role in the dynamics and the formation of molecular clouds along with the formation and destruction of important chemical species. Therefore, implementing all the possible heating and cooling processes in the ISM into AREPO will result in a more accurate simulation of the environment that we are researching.

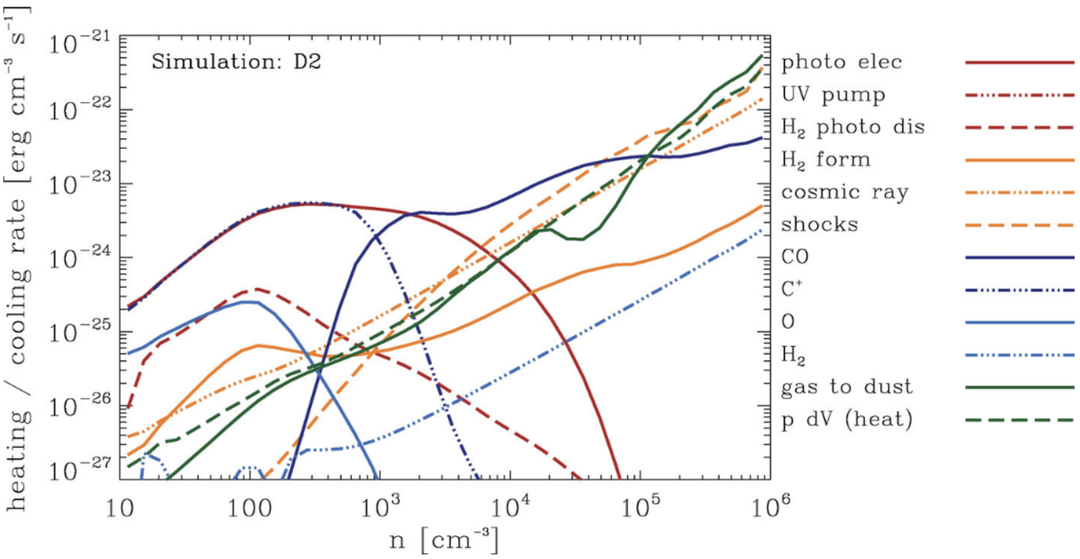

**Figure 2.8.** Figure taken from Glover & Clark (2012a) showing the heating and cooling rates per unit volume in a typical molecular cloud simulation, plotted as a function of the hydrogen nuclei number density n, at a time just before the onset of star formation.

Figure 2.8 from Glover & Clark (2012a) illustrates which heating and cooling process are dominant and shows that these heating and cooling processes are density dependent. In this section we only highlight the heating and cooling process relevant to the environment that the simulation starts and finishes in, which in our case is both the cold neutral medium and the molecular cloud phase of the ISM. We start at the higher density scale of Figure 2.8, in which the compressional adiabatic heating (P dV) dominates along with adiabatic shocks. Countering this heating is the thermal cooling due to expansion. On the opposite density scale of Figure 2.8, the photoelectric heating dominates. This is where electrons are liberated from dust grains by UV photons. These liberated electrons provide a source of heating for the gas through collisions. Since the heating and cooling processes are time dependent, we characterise their effectiveness through the rate per unit volume at which these processes heat or cool. We therefore describe the photoelectric heating rate per unit volume by the following equation,

$$\Gamma_{\rm PE} = 1.3 \times 10^{-24}\, \epsilon\, {\rm e}^{-2.5{\rm A_V}} {\rm G_0}\, n \ {\rm erg\, s^{-1}\, cm^{-3}} \quad , \tag{2.24}$$

where $\epsilon$ is the heating efficiency, the $\rm e^{-2.5A_V}$ is the effect of dust shielding, and $\rm G_0$ is the strength of the interstellar radiation field in units of Habing (1968), and $n$ is the number density of H nuclei.

The use of $\mathrm{G_0}$ is a convenient way of quantifying the intensity of UV radiation in the ISM that contribute to the photoelectric heating, and is equated to the following,

$$\mathrm{G_0} = \frac{\int_{6\mathrm{eV}}^{13.6\mathrm{eV}} u_\nu \mathrm{d}\nu}{5.29 \times 10^{-14}\,\mathrm{erg\,cm^{-3}}} \quad , \tag{2.25}$$

where $u_\nu = \frac{4\pi}{\mathrm{c}}\mathrm{J}_\nu$ is the energy density of the radiation field, and the limits in the integral are chosen such that the photons have energies to contribute to photoelectric heating. Below the lower limit of 6 eV, the energy is too low to ionise carbon, the main constituent of dust. Above the upper limit of 13.6 eV, we start to ionise hydrogen and because there is so much hydrogen in the ISM the photons with energies above 13.6 eV will be absorbed by the hydrogen rather than the dust.

The number on the denominator is the value estimated by Habing (1968) such that $\mathrm{G_0}$ would equal 1 for a solar-like environment. However, a more accurate estimate by Draine (1978) showed that the solar neighbourhood has a value of $\mathrm{G_0} = 1.7$ in units of Habing (1968).

Dust grains are also heated by photons below and above this small 6 - 13.6 eV region although less significant and the radiative heating rate per unit volume in an optically thin regime can be written as,

$$\Gamma_{\mathrm{ext}} = 4\pi\mathcal{D}\rho \int_0^\infty \kappa_\nu \mathrm{J}_\nu \mathrm{d}\nu \quad , \tag{2.26}$$

where $\mathcal{D}$ is the gas-to-dust mass fraction, $\kappa_\nu$ is the dust grain opacity, $\rho$ is the density of the gas.

To accommodate for optically thick regions, an attenuation factor, $\chi$, is multiplied by $\Gamma_{ext}$. To calculate the attenuation factor, we must know what the column density of the cell is and therefore we use the TREECOL method introduced by Clark et al. (2012). TREECOL uses the tree-based scheme used to calculate the gravitational forces in the simulation. It then creates a sphere of pixels (called a HEALPIX) which is used as the end point for the calculation of the column density. By starting at the cell that we want to calculate the column density, we trace along along the spherical grid as illustrated in Figure 2.9 and use the information that is already available from the calculation of the gravitational forces and calculate the column density along each HEALPIX pixel.

Dust grains also cool by radiating their energy away and the radiative cooling rate per unit volume can be written as,

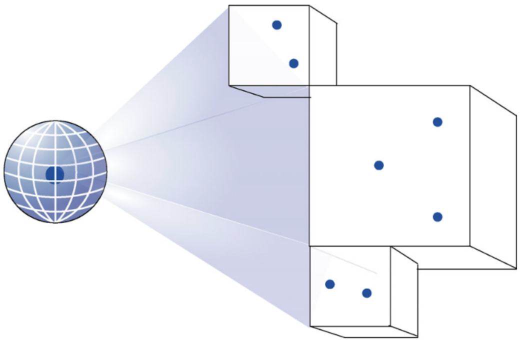

**Figure 2.9.** Diagram taken from Clark et al. (2012) illustrating the TREECOL concept.

$$\Lambda_{\rm d} = 4\pi\mathcal{D}\rho \int_0^\infty \kappa_\nu {\rm B}_\nu({\rm T_d}){\rm d}\nu \quad , \tag{2.27}$$

where $\mathrm{B}_\nu(\mathrm{T_d})$ is simply the Planck function.

Dust grains are also able to thermally interact with the gas through collision between the atoms/molecules/ions in the gas and the dust grains.

From the perspective of the gas, the energy transfer per unit volume from the gas to the dust grain is given by,

$$\Lambda_{\rm gd} \simeq 4 \times 10^{-33} {\rm T_g^{1/2}}({\rm T_g} - {\rm T_d}){\rm n}^2 \ {\rm erg\,s^{-1}\,cm^{-3}} \quad , \tag{2.28}$$

where $\mathrm{T_g}$ is the gas temperature, $\mathrm{T_d}$ is the dust temperature and n is the gas number density. One thing to note here is that if $\mathrm{T_g} < \mathrm{T_d}$, the net flow of energy is from the grains to the gas, leading to heating instead of cooling.

Cosmic ray ionization also plays a significant part in the heating processes in the ISM. This is where high-energy relativistic particles (mainly protons) ionize the gas in the ISM liberating electrons that further collide with and heat the gas. The heating rate per unit volume from the contribution of cosmic ray ionization is written as,

$$\Gamma_{\rm cr} = {\rm q_{cr}} \left( \frac{\zeta}{10^{-17}\,{\rm s^{-1}}} \right) {\rm n \ erg\,s^{-1}\,cm^{-3}} \quad , \tag{2.29}$$

where $\mathrm{q_{cr}}$ is the amount of energy deposited as heat and is a calculated through a series of complicated equations derived from Draine (2011) and Krumholz (2014), $\zeta$ is the cosmic ray ionisation rate (CRIR).

Whilst not as dominant of a heating process compared to the photoelectric emission from dust grains, photodissociation of $\mathrm{H_2}$ by UV radiation plays a role in heating the ISM at low densities as seen in Figure 2.8. The heating rate per unit volume from the contribution of photodissociation of $H_2$ is written as,

$$\Gamma_{\rm ph} = 6.4 \times 10^{-13} k_{\rm ph} {\rm n}_{\rm H_2} \; {\rm erg\,s^{-1}\,cm^{-3}} \quad , \tag{2.30}$$

where $n_{H_2}$ is the number density of molecular hydrogen, $k_{ph}$ is the photodissociation rate described by the following equation,

$$k_{\rm ph} = 3.3 \times 10^{-13} f_{\rm shield}({\rm N}_{\rm H_2}) {\rm e}^{\tau_{\rm d,1000}} {\rm G}_0 \quad , \tag{2.31}$$

where $f_{shield}(N_{H_2})$ is a numerical factor accounting for the effects of self-shielding, $\tau_{d,1000}$ is the optical depth due to dust at 1000Å which relates to the column density of total hydrogen by a factor of $2 \times 10^{-21}$ ($\tau_{d,1000} = 2 \times 10^{-21} N_{H_{tot}}$).

UV radiation can heat up molecular hydrogen without dissociating molecular hydrogen into two atomic hydrogen. This is through a process called “UV pumping”, which is where UV radiation produces vibrationally excited $H_2$ via radiative pumping. This produces heat at high densities through collisional de-excitation. We assume a heat transfer of 2 eV per UV photon (Burton et al., 1990) and adopt a pumping rate that is 6.94 times larger than the photdissociation rate, $k_{ph}$ (Draine & Bertoldi, 1996).

We also consider the recombination cooling processes for our simulations, notably the gas-phase recombination and the recombination on dust grains. The former is where ions collide with free moving electrons and recombine to give its atomic/molecular form. The later is where an ionized dust grain collides with a free moving electron. These are both cooling processes since the binding energy and the free electron’s kinetic energy are radiated away.

Two of the main cooling contributions found in Figure 2.8 [CII] and CO line cooling. All cooling through line cooling is done by radiating away the energy that a molecule in an excited state has through either collisional or spontaneous de-excitation. In the case of [CII], its main contribution to the cooling comes from the transition between the two fine structure levels in its ground state. Equally for CO, the main contribution to the cooling comes from the transition from first rotationally excited level J = 1 to the ground state J = 0. We also consider the effects of line cooling in our simulation from [CI], [OI], [SiII], $^{13}$CO, C$^{18}$O and $H_2$. In all cases, the main contribution to the cooling rate is dictated by the gas temperature and the number density of both the molecule and its main collisional partner.

### 2.1.10 CHEMISTRY

AREPO evolves the chemistry of the environment through the use of chemical networks, which is to say a network of chemical reactions that can be switched on and off depending on the environment that the simulation is investigating. The inclusion of chemistry gives us the ability to maintain a more accurate portrayal of the cooling processes in the molecular phase of the ISM. Since line cooling is the dominant process in this region and the more abundant these chemical species that contribute to line cooling the colder and denser these regions will be. Being able to get a good estimate of the gas temperature also gives us the ability to more accurately get an estimate of the level populations of HCN and therefore a better estimate of the HCN emission. Therefore an accurate treatment of both the thermodynamics and chemistry is required in our simulations. We use a modified version of the chemical network developed by Gong et al. (2017), which itself improved upon the chemical network introduced by Nelson & Langer (1999). The chemical reactions involved in our simulations are all shown in both Tables 2.1 and 2.2. One might notice that there is no treatment of nitrogen in our chemical network. This is due to the complex nature of nitrogen chemistry, it is currently computationally intractable to self-consistently compute the time-dependent abundance of HCN in AREPO. These chemical networks have been in production for over 25 years since Nelson & Langer (1997), and have since been improved upon to that of Gong et al. (2017).

## 2.2 RADMC-3D

Like the name suggests, observers probe and diagnose astrophysical systems through the process of making observations of said astrophysical system, i.e. recording the emission that emanates from these observed regions. Therefore, in order to link our simulations to the work that the observers have done we must simulate the emission that would emanate from our simulations. To model the propagation of light in our simulations we first have to look at the physics of how light propagates through the ISM, which is through radiative transfer. We therefore start by writing the equation of radiative transfer,

$$\frac{\mathrm{dI}_\nu(\omega)}{\mathrm{ds}} = \mathrm{j}_\nu(\omega) - \alpha_\nu(\omega)\mathrm{I}_\nu(\omega) \quad , \tag{2.32}$$

where $\omega$ is the direction, $\mathrm{I}_\nu$ is the specific intensity at a given frequency, $\nu$, $\mathrm{j}_\nu$ is the emissivity coefficient and $\alpha_\nu$ is the absorption coefficient.

**Table 2.1.** List of Collisional Chemical Reactions.

| No. | Reaction | Reference |
|---|---|---|
| 1 | $H + e^- \rightarrow H^+ + e^- + e^-$ | Janev et al. (1987) |
| 2 | $H^+ + e^- \rightarrow H + \gamma$ | Ferland et al. (1992) |
| 3 | $He^+ + H_2 \rightarrow H_2^+ + He$ | Barlow et al. (1984) |
| 4 | $He^+ + H_2 \rightarrow H^+ + H + He$ | Barlow et al. (1984) |
| 5 | $H_2 + e^- \rightarrow H + H + e^-$ | Trevisan & Tennyson (2002) |
| 6 | $H_2 + H \rightarrow H + H + H$ | Mac Low & Shull (1986), Lepp & Shull (1983)<br>Martin et al. (1996) |
| 7 | $H_2 + H_2 \rightarrow H + H + H_2$ | Martin et al. (1998), Jacobs et al. (1967) |
| 8 | $H_2^+ + H_2 \rightarrow H_3^+ + H$ | Linder et al. (1995) |
| 9 | $H_2^+ + H \rightarrow H_2 + H^+$ | Karpas et al. (1979) |
| 10 | $H_3^+ + e^- \rightarrow H + H + H$ | McCall et al. (2004) |
| 11 | $H_3^+ + e^- \rightarrow H_2 + H$ | McCall et al. (2004) |
| 12 | $He + e^- \rightarrow He^+ + e^- + e^-$ | Janev et al. (1987) |
| 13 | $He^+ + e^- \rightarrow He + \gamma$ | Hummer & Storey (1998), Badnell (2006) |
| 14 | $C^+ + H_2 \rightarrow CH_X + H$ | Wakelam et al. (2010), Gong et al. (2017) |
| 15 | $C^+ + H_2 + e^- \rightarrow C + H + H$ | Wakelam et al. (2010), Gong et al. (2017) |
| 16 | $C + H_2 \rightarrow CH_X + \gamma$ | Prasad & Huntress (1980) |
| 17 | $C + H_3^+ \rightarrow CH_X + H_2$ | Vissapragada et al. (2016) |
| 18 | $C^+ + e^- \rightarrow C + \gamma$ | Badnell (2006), Badnell et al. (2003) |
| 19 | $C + e^- \rightarrow C^+ + e^- + e^-$ | Voronov (1997) |
| 20 | $O^+ + H \rightarrow O + H^+$ | Stancil et al. (1999) |
| 21 | $O + H^+ \rightarrow O^+ + H$ | Stancil et al. (1999) |
| 22 | $O^+ + H_2 \rightarrow OH_X + H$ | Gong et al. (2017) |
| 23 | $O^+ + H_2 + e \rightarrow O + H + H$ | Gong et al. (2017) |
| 24 | $O + H_3^+ \rightarrow OH_X + H_2$ | de Ruette et al. (2016) |
| 25 | $O + H_3^+ + e^- \rightarrow H_2 + O + H$ | de Ruette et al. (2016) |
| 26 | $C^+ + OH_X \rightarrow HCO^+$ | Gong et al. (2017) |
| 27 | $C + OH_X \rightarrow CO + H$ | Zanchet et al. (2009) |
| 28 | $CH_X + He^+ \rightarrow C^+ + He + H$ | Prasad & Huntress (1980), McElroy et al. (2013) |
| 29 | $CH_X + H \rightarrow H_2 + C$ | Wakelam et al. (2010) |
| 30 | $CH_X + O \rightarrow CO + H$ | Wakelam et al. (2010) |
| 31 | $OH_X + H \rightarrow H_2 + O$ | McElroy et al. (2013), Tsang & Hampson (1986) |
| 32 | $OH_X + O \rightarrow O + O + H$ | Carty et al. (2006) |
| 33 | $OH_X + He^+ \rightarrow O^+ + He + H$ | Wakelam et al. (2010) |
| 34 | $CO + H_3^+ \rightarrow HCO^+ + H_2$ | Kim et al. (1975) |
| 35 | $CO + He^+ \rightarrow C^+ + O + He$ | Petuchowski et al. (1989) |
| 36 | $CO + H \rightarrow C + OH_X$ | Mitchell (1984) |
| 37 | $HCO^+ + e^- \rightarrow OH_X + C$ | Geppert et al. (2005) |
| 38 | $HCO^+ + e^- \rightarrow CO + H$ | Geppert et al. (2005) |
| 39 | $Si^+ + e^- \rightarrow Si + \gamma$ | Nahar (2000) |
| 40 | $Si + e^- \rightarrow Si^+ + e^- + e^-$ | Voronov (1997) |

**Table 2.2.** List of Grain-assisted Reactions, Cosmic-Ray Reactions, and Photodissociation Reactions.

| No. | Reaction | Reference |
|---|---|---|
| 1 | $H + H + gr \rightarrow H_2 + gr$ | Hollenbach & McKee (1979) |
| 2 | $H^+ + e^- + gr \rightarrow H + gr$ | Weingartner & Draine (2001) |
| 3 | $C^+ + e^- + gr \rightarrow C + gr$ | Weingartner & Draine (2001) |
| 4 | $He^+ + e^- + gr \rightarrow He + gr$ | Weingartner & Draine (2001) |
| 5 | $Si^+ + e^- + gr \rightarrow Si + gr$ | Weingartner & Draine (2001) |
| 6 | $H + cr \rightarrow H^+ + e^-$ | Glassgold & Langer (1974) |
| 7 | $H_2 + cr \rightarrow H_2^+ + e^-$ | Glassgold & Langer (1974) |
| 8 | $H_2 + cr \rightarrow H + H^+ + e^-$ | McElroy et al. (2013) |
| 9 | $H_2 + cr \rightarrow H + H$ | McElroy et al. (2013) |
| 10 | $He + cr \rightarrow He^+ + e^-$ | McElroy et al. (2013) |
| 11 | $C + cr \rightarrow C^+ + e^-$ | McElroy et al. (2013) |
| 12 | $CO + H + cr \rightarrow HCO^+ + e^-$ | Gong et al. (2017) |
| 13 | $C + \gamma_{cr} \rightarrow C^+ + e^-$ | Heays et al. (2017) |
| 14 | $CO + \gamma_{cr} \rightarrow C + O$ | Heays et al. (2017) |
| 15 | $Si + \gamma_{cr} \rightarrow Si^+ + e^-$ | Heays et al. (2017) |
| 16 | $C + \gamma \rightarrow C^+ + e^-$ | Heays et al. (2017) |
| 17 | $CH_X + \gamma \rightarrow C + H$ | Gong et al. (2017), Heays et al. (2017) |
| 18 | $CO + \gamma \rightarrow C + O$ | Heays et al. (2017) |
| 19 | $OH_X + \gamma \rightarrow O + H$ | Gong et al. (2017), Heays et al. (2017) |
| 20 | $Si + \gamma \rightarrow Si^+ + e^-$ | van Dishoeck (1988) |
| 21 | $H_2 + \gamma \rightarrow H + H$ | Draine & Bertoldi (1996) |

Both the emissivity and absorption coefficients describe how the light is emitted and absorbed as it travels through the ISM and can be absorbed and emitted by different means. The first means of absorption and emission is through dust grains.

Due to the complex nature of scattering, most radiative transfer codes make approximations by using a ray tracing technique which assumes that the light propagates by straight rays. Therefore, our case is simplified to no longer consider dust grain scattering and only consider the thermal emission and absorption. The absorption from dust grains can be written as,

$$\alpha_\nu^{\mathrm{abs}} = \rho_{\mathrm{dust}} \kappa_\nu^{\mathrm{abs}} \quad , \tag{2.33}$$

where $\rho_{\mathrm{dust}}$ is the density of dust grains and $\kappa_\nu^{\mathrm{abs}}$ is the absorption opacity.

And through Kirchhoff's law we can write the emission from dust grains as,

$$\mathrm{j}_\nu^{\mathrm{therm}} = \alpha_\nu^{\mathrm{abs}} \mathrm{B}_\nu(\mathrm{T}) \quad , \tag{2.34}$$

where $\mathrm{B}_\nu(\mathrm{T})$ is the Planck function.

The most important mode of propagation of light in our case is through line emission, since we are investigating the emission of HCN. The absorption of light with a frequency, $\nu$, that excites a given species of gas from a lower energy level, $j$, to a higher energy level, $i$, is described by the following equation,

$$\alpha_{\mathrm{ij}}(\omega, \nu) = \frac{\mathrm{h}\nu}{4\pi}(\mathrm{n_j B_{ji}} - \mathrm{n_i B_{ij}})\phi_{\mathrm{ij}}(\nu) \quad , \tag{2.35}$$

where h is the planck constant, $\mathrm{n_j}$ is the number density of atoms in the lower energy level, $\mathrm{n_i}$ is the number density of atoms in the higher energy level, $\mathrm{B_{ji}}$ and $\mathrm{B_{ij}}$ are the Einstein coefficients of stimulated absorption and emission respectively and $\phi_{\mathrm{ij}}(\nu)$ is the line profile function.

The emission of light of a given gas species due to a de-excitation from a higher energy level, $i$, to a lower energy level, $j$, is described by the following equation,

$$\mathrm{j_{ij}}(\omega, \nu) = \frac{\mathrm{h}\nu}{4\pi}\mathrm{n_i A_{ij}}\phi_{\mathrm{ij}}(\nu) \quad , \tag{2.36}$$

where $\mathrm{A_{ij}}$ is the Einstein coefficient of spontaneous emission. Note that these Einstein coefficients obey,

$$\mathrm{A_{ij}} = \frac{2\mathrm{h}\nu_{\mathrm{ij}}^3}{\mathrm{c}^2}\mathrm{B_{ij}}, \quad \mathrm{B_{ji} g_j} = \mathrm{g_i B_{ij}} \quad , \tag{2.37}$$

where c is the speed of light and both $\mathrm{g_j}$ and $\mathrm{g_i}$ are the statistical weights of the energy levels.

In local thermal equilibrium (LTE), the relative level populations between state i and state j is given by the Boltzmann distribution,

$$\frac{\mathrm{n_i}}{\mathrm{n_j}} = \frac{\mathrm{g_i}}{\mathrm{g_j}} \mathrm{e}^{-\mathrm{h}\nu/\mathrm{kT}} \quad . \tag{2.38}$$

The inclusion of a line profile function is due to the fact that the atomic energy levels are not infinitely sharp and due to the uncertainty principle the spectral line will have some natural broadening and other forms of line broadening. For a zero velocity field, the line profile that describes the broadening of the emission about a given central frequency, $\nu$, is given by,

$$\phi_{\mathrm{ij}}(\nu) = \frac{\mathrm{c}}{\mathrm{a_{therm}}\nu_{\mathrm{ij}}\sqrt{\pi}} \exp - \frac{\mathrm{c}^2(\nu - \nu_{\mathrm{ij}})^2}{\mathrm{a}^2_{\mathrm{therm}}\nu^2_{\mathrm{ij}}} \quad , \tag{2.39}$$

where $\nu_{\mathrm{ij}}$ is the line-centre frequency for the line and $\mathrm{a_{therm}}$ is the line width in units of cm/s due to thermal broadening and is given by,

$$\mathrm{a_{therm}} = \sqrt{\frac{2\mathrm{kT_{gas}}}{\mathrm{m_{mol}}}} \quad , \tag{2.40}$$

where k is the Boltzmann constant, $\mathrm{T_{gas}}$ is the gas temperature and $\mathrm{m_{mol}}$ is the molecular mass of the given gas species.

If we a introduce Doppler shifting, that is, the broadening of the spectral lines due to the motion of the atoms with respect to each other, the line profile is altered to the following,

$$\phi_{\mathrm{ij}}(\omega, \nu) = \phi_{\mathrm{ij}}(\nu(1 - \boldsymbol{\omega} \cdot \mathbf{v}/\mathrm{c}) - \nu_{\mathrm{ij}}) \quad . \tag{2.41}$$

In cases such as ours we can have lines than can be sub-critically excited and therefore need to consider non-local thermal equilibrium (non-LTE) line transfer. This renders equation 2.38 obsolete in these cases where we are not in LTE. In these cases one must then compute the level populations consistent with the local density and temperature. A full non-LTE radiative transfer calculation is too numerically demanding and often unnecessary. However, some codes such as LIME (Brinch & Hogerheijde, 2010) and TORUS (Harries et al., 2019) can indeed perform full non-LTE radiative transfer. In most cases, a simple approximation of the non-LTE effects is sufficient. A code such as RADMC-3D Dullemond et al. (2012) instead uses the Sobolev approximation, more commonly known as the Large Velocity Gradient (LVG) method. In his paper, Sobolev (1957) introduced the idea that a photon can escape a medium due to Doppler shifting before it is reabsorbed. Whether a photon can escape or not is determined by the velocity gradient, $\nabla \mathbf{v}$, i.e. the bigger the velocity gradient the more likely the photon is to escape and not be reabsorbed. To calculate the escape probability of a photon, we use the following equation,

$$\beta_{\rm ij} = \frac{1 - \exp\left(-\tau_{\rm ij}\right)}{\tau_{\rm ij}} \quad , \tag{2.42}$$

where $\tau_{\rm ij}$ is the line-centre optical depth of the line. For the LVG method this optical depth is given by the velocity gradient,

$$\tau_{\rm ij}^{\rm LVG} = \frac{\rm c^3}{8\pi\nu_{\rm ij}^3} \frac{\rm A_{ij}}{1.064|\nabla \mathbf{v}|} \left( \frac{\rm g_i}{\rm g_j} \rm n_j - n_i \right) \quad , \tag{2.43}$$

where $|\nabla \mathbf{v}|$ is the absolute value of the velocity gradient and $\nu_{\rm ij}$ is the line frequency for the transition from state i to state j (van der Tak et al., 2007).

For all of our simulations we use Radmc-3D to synthesise our emission. The input files required to successfully run Radmc-3D are based on all of the equations mentioned above and for clarity have collated all of the input files required to run Radmc-3D ito Table 2.3. All of our input files for Radmc-3D were re-grided from the Voronoi mesh structure found in Arepo to a simple Cartesian grid for Radmc-3D.

**Table 2.3.** List of input files required to run a non-LTE radiative transfer in RADMC-3D.

| File | Overview of the purpose of the input file |
|---|---|
| amr_grid.inp | sets the structure of the grid |
| camera_wavelength_micron.inp | inputs a range of wavelengths around the rest wavelength of the gas species to catch emission due to doppler shifting of the line |
| dust_density.inp | input file for the density of dust grains |
| dustkappa_silicate.inp | sets the value of $\kappa$ in equation 2.33 |
| dustopac.inp | sets various dust grain options and to use the above file |
| dust_temperature.dat | input file for the dust grain temperature |
| gas_temperature.inp | input file for the gas temperature |
| gas_velocity.inp | input file for the gas velocity |
| lines.inp | sets which gas species and collisional partners are used and controls the transition levels |
| molecule_X.inp | input file that gives the Einstein coefficients at various densities and temperatures and is in the format of the files produced by LAMDA Leiden Atomic and Molecular Database |
| numberdens_X.inp | input file for the number density of the gas species |
| numberdens_C.inp | input file for the number density of the collisional partners of the gas species |
| radmc.inp | sets various other options that can be switched on in RADMC-3D |
| wavelength_micron.inp | input file that provides a range of wavelengths for dust emission |

# CHAPTER 3

# NUMERICAL SIMULATIONS OF CLOUD-CLOUD COLLISIONS

To be able to link the simulations to the observations, the simulations must be a representative environment that observers observe HCN in. To recap what was said in Chapter 1, the regions in which HCN is observed is in star forming molecular cloud regions; since HCN is a dense gas tracer where star formation occurs, thus HCN is a good tracer for those researching star formation. In this chapter, we create several molecular cloud environments through numerical simulations, investigating the physical properties of these environments that will then be post-processed in Chapters 4 and 5 which will then be compared to observations.

Typically these star forming regions are found in spiral arms of galaxies and therefore require the inclusion of the dynamics and kinematics that is present in these spiral arms into our simulations. There are several methods of creating an environment such that is expected of these spiral galaxy arm regions. It is also achievable through numerical simulations such as AREPO that is used for the numerical simulations throughout this thesis, which is described in more detail in Chapter 2.

Molecular cloud environments vary from region to region even in our own milky way. Dobbs (2008) shows that molecular clouds collide with each other and that their collisional speeds vary from $\sim 1 - 30$ km s$^{-1}$. This is not the only variation a molecular cloud can have. The Interstellar radiation field can also vary significantly depending on the number of O and B type stars and their proximity to these molecular cloud regions. This affects the heating and cooling processes in the cloud, since the O and B type stars are the main contributors of UV radiation and cosmic rays in the ISM (Blasi, 2013). An increase in UV radiation will heat the ISM through the photoelectric effect of dust grains. An increase in cosmic rays will heat the ISM through ionization of predominantly Hydrogen and Helium nuclei. There is no such thing as a “standard” molecular cloud environment that we can use to replicate spiral arms of galaxies, therefore several different simulations need to be made exploring all the available parameter space.

There is observational evidence from Tan (2000), Dobbs (2008),Wu et al. (2017) and Liow & Dobbs (2020) in which they show that these spiral arms are chaotic and that these molecular clouds consistently collide with one another. We conclude that the most likely scenario of the formation of these dense clouds is through molecular clouds colliding with one another. Therefore, throughout this thesis, we shall investigate a colliding cloud scenario where two spherical clouds collide head on. Our justification for spherical clouds is that the energy contained in the cloud is much easier to calculate in spherical form than any other. For simplicity we collide head on since Hunter et al. (2021) found little variation in the formation of dense gas with an off-axis collision.

In this section we will create 10 different simulations; 4 of which will explore the variation in the cloud-cloud collisional speed, and 6 of which will explore the variations in the IRSF along with cosmic rays. The simulations of varying cloud-cloud collisional speeds are separated into its own section with the simulations varying ISRF strength also in a section of its own.

## 3.1 Initial Conditions for the variation in the cloud-cloud collisional speed

Our simulations start with two spherical clouds, each with a radius of 19.04 pc, a number density of 10 $\mathrm{cm}^{-3}$ (note that we will refer to ‘number density’ simply as ‘density’ for the rest of this thesis) and a mass of $1 \times 10^4$ $\mathrm{M}_\odot$. Both clouds have an initial temperature of 300 K, consistent with the balance between fine structure cooling and photoelectric heating at a number density of 10 $\mathrm{cm}^{-3}$. The geometry of the simulation is such that the cloud centres are placed at a distance of 57.11 pc and 114.23 pc respectively in x, while both centres are placed at a distance of 85.67 pc in both y and z in a cuboid of size 171.34 pc. The velocity of each cloud is mirrored along x such that they are sent on a collision course with one another. Four different velocities are chosen to cover the typical and extremes of the velocity distribution of the gas flow in spiral arms (Dobbs, 2008); 1.875 $\mathrm{km\,s}^{-1}$, 3.75 $\mathrm{km\,s}^{-1}$, 7.5 $\mathrm{km\,s}^{-1}$ and 15 $\mathrm{km\,s}^{-1}$ (note that these quoted velocities are the velocities of the individual clouds, i.e. the relative velocity is twice these values). An initial turbulent velocity

**Table 3.1.** A brief overview of all twelve cases that were post-processed through RADMC-3D. In the table, the time denotes the time at which the simulation has evolved to before being post-processed through RADMC-3D. The mass denotes the total mass that lies in our 10pc box that is post-processed through RADMC-3D. For clarity we group each case to their simulation corresponding to the initial cloud-cloud velocity in ascending order.

| ID | Initial velocity $[\mathrm{km\,s^{-1}}]$ | Time [Myr] | Mass $[\mathrm{M_\odot}]$ |
|---|---|---|---|
| A | 1.875 | 12.22 | 2176.49 |
| B | 1.875 | 13.31 | 2929.12 |
| C | 1.875 | 14.51 | 3590.91 |
| D | 3.75 | 6.46 | 2026.82 |
| E | 3.75 | 8.35 | 3153.03 |
| F | 3.75 | 10.69 | 4129.07 |
| G | 7.5 | 3.48 | 1971.21 |
| H | 7.5 | 5.47 | 3414.21 |
| I | 7.5 | 8.04 | 4380.66 |
| J | 15 | 5.07 | 1817.20 |
| K | 15 | 8.54 | 2636.88 |
| L | 15 | 11.60 | 2867.27 |

field is applied to the clouds, which follows a $\mathrm{P(k)} \propto \mathrm{k}^{-4}$ scaling law with a natural mix of solenoidal to compressive modes. The velocity dispersion of the turbulence is set to 1.16 $\mathrm{km\,s^{-1}}$, which provides virial balance between the (bulk) kinetic and gravitational energies. By allowing a period of time between the initial set-up and the cloud collision, the supersonic turbulence (Mach number of $\sim 2$) has the chance to create structure in the clouds before they encounter the main collisional shock.

Each cloud is initially modelled with 2,000,000 cells, randomly generated in a sphere, such that the initial cell mass is 0.005 $\mathrm{M_\odot}$. A further 262,144 cells, with mass 0.066 $\mathrm{M_\odot}$ are randomly injected into the rest of the computational domain to model the background gas, which is taken to have a density of 0.063 $\mathrm{cm^{-3}}$. As the simulation progresses, the mesh is constantly monitored to maintain a cell mass of roughly 0.005 $\mathrm{M_\odot}$. On top of this, we impose three further resolution criteria. The first criterion is that the Jeans length is resolved by at least 16 cells, to make sure we correctly capture the fragmentation in the gas. The second criterion is that the volume of neighbouring cells differs by no more than a factor of 8. Finally, we set a minimum and maximum cell size of 100 AU, and 12 pc, respectively.

Due to self-gravity in AREPO, the gas in our simulations has the ability to form regions of high density that can undergo runaway gravitational collapse. The final outcome of such a process would be the formation of a star or small stellar system. We employ sink particles (Bate et al., 1995) to model these objects, and to follow both their dynamics and further accretion. In this study, several conditions must be met for a gas cell to be turned into a sink particle, which follows the criteria laid out in Federrath et al. (2010). First, the candidate cell must be above our sink creation density $n_{\rm sink} = 10^8$ cm$^{-3}$, and be a local minimum in the gravitational potential. Then we require that the gas within the sink accretion radius, $r_{\rm sink}$ – here taken to be 185 AU – must be gravitationally bound, and both moving towards *and* accelerating towards the candidate's location – that is, the mass-weighted $\nabla \cdot \mathbf{v}$ and $\nabla \cdot \mathbf{a}$ within the sink creation radius must be negative.

The presence of magnetic fields in molecular clouds has long been known and summarised by Crutcher (1999); Crutcher et al. (2010); Crutcher (2012) and Hennebelle & Inutsuka (2019). A magnetohydrodynamical (MHD) module was implemented into AREPO, which is described in detail in Pakmor et al. (2011) and in Section 2.1.5. Because we know that there are magnetic fields present in molecular clouds and that we have a MHD module at our disposal in AREPO, we therefore utilise this MHD module in our research in order to reproduce a more representative environment that observers see. This module includes hyperbolic divergence cleaning (Dedner et al., 2002) and the divergence advection terms introduced by Powell et al. (1999). The magnetic field strength is observed to be a function of density (Crutcher et al., 2010; Crutcher, 2012), and our adopted field strength of 3 $\mu$G is consistent with observations and our initial density of 10 cm$^{-3}$. Due to the already large parameter range in this study, we chose to keep the strength of the magnetic field fixed. The magnetic field is therefore an ingredient of our initial conditions in this study, but it is not something that we explore. In our initial setup, the direction of the magnetic field is along x such that the collision is occurring along the magnetic field lines.

We adopt a composition characteristic of the local ISM for the metals and dust included in our ISM model (i.e. the heating and cooling and time-dependent chemistry). The initial abundances of carbon and oxygen are set to $x_{\rm C} = 1.4 \times 10^{-4}$ and $x_{\rm O} = 3.2 \times 10^{-4}$, respectively, as given by Sembach et al. (2000), where $x_i$ is the fractional abundance of the element relative to hydrogen nuclei. We assume that the carbon starts in the form of $\rm C^+$ due to the photoionization by the ISRF, and that oxygen starts in the form of neutral oxygen. We also assume that most of the hydrogen starts in atomic form, and that a small amount of hydrogen is in $\rm H^+$ form ($x_{\rm H^+} \sim 0.01$) due to the balance of cosmic ray ionization and recombination.

For our model of the interstellar radiation field (ISRF), we adopt the spectral shape described in Mathis et al. (1983) at longer wavelengths and Draine (1978) at UV wavelengths. The strength of the ISRF is $G_0 = 1.7$ in Habing (1968) units (see Draine 2011) and the cosmic ray ionization rate of atomic hydrogen is set to $\zeta_{\mathrm{H}} = 3 \times 10^{-17}$ s$^{-1}$.

## 3.2 Initial Conditions for our variation in ISRF

For our initial setup, we place two spherical clouds in a cuboid box with their centres separated by a set distance. We vary 3 different parameters; which can be seen in Table 3.2. We primarily vary the main component of the ISRF strength which is the UV radiation strength represented by the Draine (1978) fit with a standard value of $\mathrm{G}_0 = 1.7$ Habing (1968) units. We vary $\mathrm{G}_0$ by a multiple of ten from 0.1 to 100 as shown in Table 3.2. We also vary the CRIR of atomic hydrogen for one simulation from the standard value of $3 \times 10^{-17}\mathrm{s}^{-1}$ based on the research by Field et al. (1969) to $300 \times 10^{-17}\mathrm{s}^{-1}$ whilst keeping the value of $\mathrm{G}_0$ to the standard value of 1.7 Habing units.

The last variable parameter in our simulations is the clouds initial mass and so the geometry of the simulations vary also. For the first simulation, we chose a cloud mass of $1 \times 10^4$ $\mathrm{M}_\odot$, a number density of 10 cm$^{-3}$ and therefore a radius of 19.04 pc. The geometry of the simulation is such that the cloud centres are placed at a distance of 38.08 pc and 119.82 pc respectively in x, while both centres are placed at a distance of 78.95 pc in both y and z in a cuboid of size 157.9 pc.

For all other simulations we chose a cloud mass of $1 \times 10^5$ $\mathrm{M}_\odot$, a number density of 10 cm$^{-3}$ and therefore a radius of 41.01 pc. The geometry of these simulations is such that the cloud centres are placed at a distance of 82.03 pc and 162.62 pc respectively in x, while both centres are placed at a distance of 122.33 pc in both y and z in a cuboid of size 244.66 pc.

For all simulations, the initial temperature of both clouds is set at a value of 300 K, consistent with the balance between fine structure cooling and photoelectric heating at a number density of 10 cm$^{-3}$.

The velocity of each cloud is chosen to be 5 kms$^{-1}$, which is a typical velocity of the gas flow in spiral arms (Dobbs, 2008). The direction of travel of both clouds is such that they are on a collision course with one another. All other variable parameters such as the number of cells, Jeans length, accretion radius etc than can be inputted into Arepo are identical to that of Section 3.1.

We adopt values for the initial abundances of carbon and oxygen to be $x_{\mathrm{C}} = 1.4x10^{-4}$ and $x_{\mathrm{O}} = 3.2x10^{-4}$ given by Sembach et al. (2000), where $x_i$ is the fraction of abundance of the element relative to hydrogen nuclei. We assume that the carbon starts in the form of C+ due to the photoionization by the ISRF, and that oxygen

**Table 3.2.** A brief overview of all 6 cases that were post-processed through RADMC-3D. Again, the time denotes the time at which the simulation has evolved to before being post-processed through RADMC-3D.

| ID | Initial Mass | $G_0$ | CRIR | Time |
|---|---|---|---|---|
| | [$M_\odot$] | [Habing] | [$\times 10^{-17} s^{-1}$] | [Myr] |
| A | 1e4 | 1.7 | 3 | 8.74 |
| B | 1e5 | 1.7 | 300 | 4.95 |
| C | 1e5 | 1.7 | 3 | 3.9 |
| D | 1e5 | 0.17 | 3 | 2.9 |
| E | 1e5 | 17 | 3 | 4.34 |
| F | 1e5 | 170 | 3 | 4.55 |

starts in the form of neutral oxygen. We also assume that most of the hydrogen starts in atomic form, and that a small amount of hydrogen is in H+ form ($x_{\mathrm{H+}} \sim 0.01$) due to the balance of cosmic ray ionization and recombination.

## 3.3 Overview of the cloud-cloud collision simulations

We present four cloud-cloud collision simulations, with each investigating a different collision velocity, as outlined in Section 3.1. In Figure 3.2, we show the evolution of the 3.75 km s$^{-1}$ simulation from its initial conditions, to give the reader a better understanding of how our clouds evolve. Figure 3.2 shows that even though the simulations begin from unrealistic spheres, the simulations evolve over time to form dense filamentary structures, consistent with the chaotic environment familiar from both previous colliding flow models and from observational studies of molecular clouds. As the clouds meet, the two supersonic colliding flows cause a shocked layer at the point of impact creating a layer of dense gas. This process repeats as more of the in-flowing gas from the opposing edges of the clouds fall into the shocked dense region.

All simulations are evolved to a point $\sim 1 - 3$ Myr after the formation of the first sink particle, which we will denote as $t_{\mathrm{SF}}$ – the time of "star formation". In each of simulations, $t_{\mathrm{SF}}$ occurs at roughly 15 Myr, 11 Myr, 9 Myr and 12 Myr for the 1.875 km s$^{-1}$, 3.75 km s$^{-1}$, 7.5 km s$^{-1}$ and 15 km s$^{-1}$ initial bulk velocities respectively.

In Figure 3.1, we plot the evolution of the mass above different density thresholds ($n_{\mathrm{thr}}$) as a function of time. We see that a higher collision velocity between the two clouds decreases the time taken to form gas above $n_{\mathrm{thr}} \sim 10^4$ cm$^{-3}$. However this trend does not continue as we move to higher $n_{\mathrm{thr}}$: the faster flow of 15 km s$^{-1}$

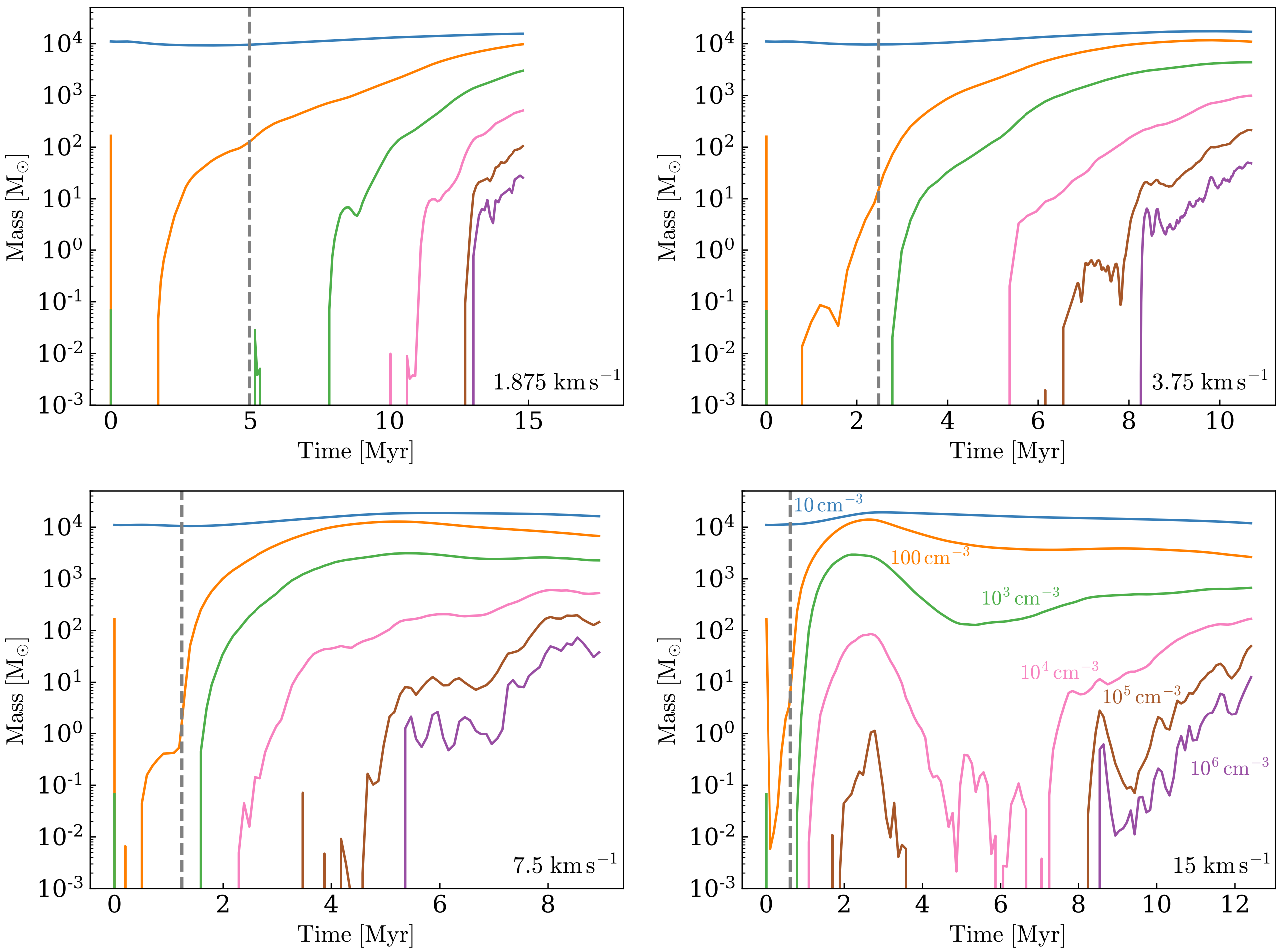

**Figure 3.1.** Evolution of mass of the gas within the simulations that lies above a given density threshold, which is labelled on the final plot. Each plot shows the evolution of mass with different initial velocities. From left to right, we have initial velocities of 1.875 km s$^{-1}$, 3.75 km s$^{-1}$, 7.5 km s$^{-1}$, 15 km s$^{-1}$. Note that the gray, vertical line denotes the approximate time at which the edge of both clouds come into contact.

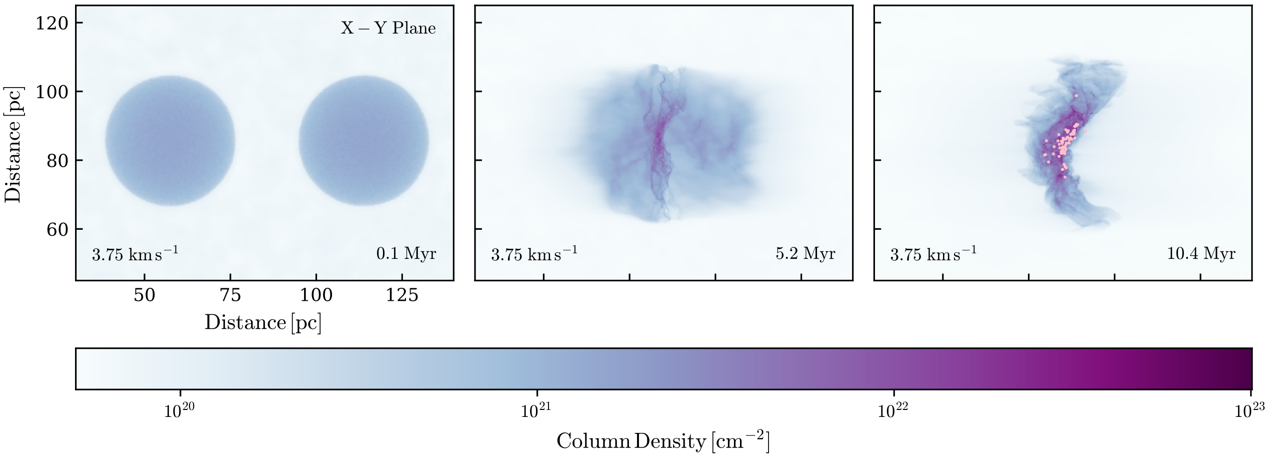

**Figure 3.2.** Column density of the 3.75 km s$^{-1}$ simulation at three different times, one at the start of our simulation, and the other two at 5.2 Myr intervals. The sink particle locations are also included in any image that possess sink particles which are represented as pink points.

has a clear difficulty in forming gas with density above $10^6$ cm$^{-3}$, and indeed actively seems to lose gas above $n_{\rm thr} \sim 10^4\,{\rm cm}^{-3}$ at times between $\sim 4 - 8$ Myr. This implies that much of the dense gas that is initially created in the 15 km s$^{-1}$ simulation is not self-gravitating, and either re-expands once the confining flow has finished, or is shredded by further interactions with surrounding flows. Only at late times (beyond around 8 Myr), once some of the collisional kinetic energy has been dissipated, are gravitationally bound regions able to form, providing an increase in the dense gas fractions. The dip and rise in the $n_{\rm thr} = 10^3\,{\rm cm}^{-3}$ line indicates that this occurs at initially quite low densities (and thus large scales).

Using Figure 3.1, we can see that by the point at which we terminate the simulation (as presented in the graph's timeline), somewhere between 0.5-3.6% of the total cloud mass sits above a density of $10^4$ cm$^{-3}$ and 0.04-0.2% of the total cloud mass above a density of $10^6$ cm$^{-3}$. The simulations have therefore evolved far enough for us to proceed with the analysis of the HCN emission with RADMC-3D, as they contain gas at densities commonly associated with prestellar cores, and starting to form sink particles.

## 3.4 Overview of the simulations of varying ISRF

We present six cloud-cloud collision simulations, with each simulation varying a different parameter according to Table 3.2. For consistency, all simulations were evolved until the first sink particle was created. At the point the first sin particle was

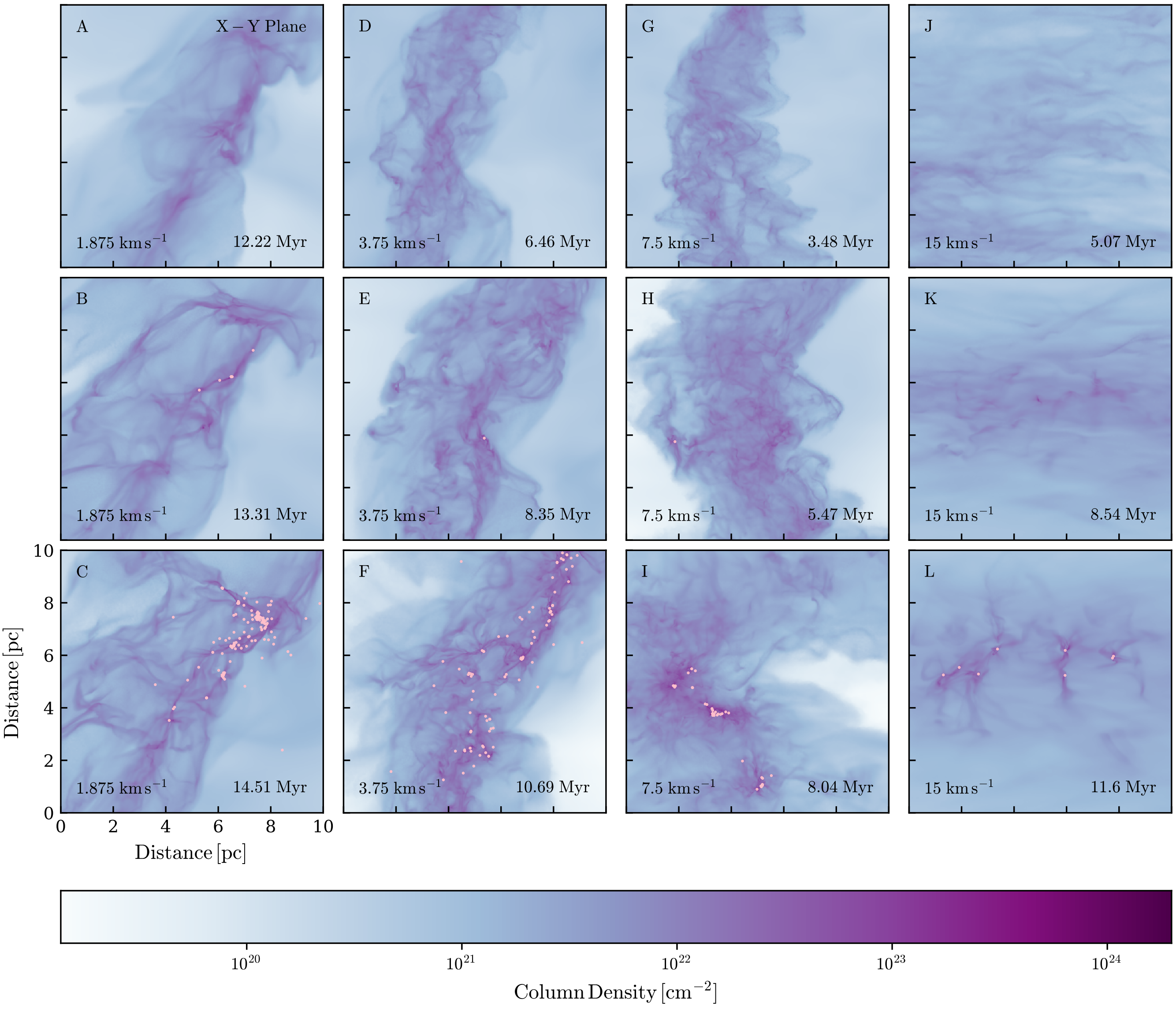

**Figure 3.3.** This grid of column densities shows the state of each simulation at the three points in their evolution where the RT is performed. The sink particle locations are also included in any image that possess sink particles which are represented as pink points. Note that the alphabetical letters on each tile corresponds to the IDs in Table 4.1.

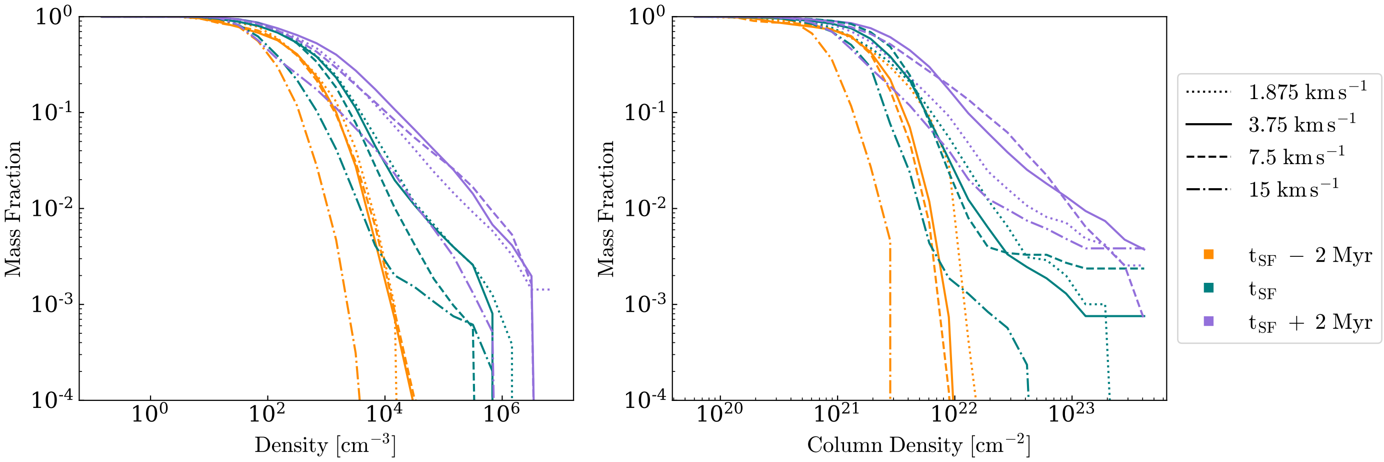

**Figure 3.4.** Comparison of the normalized mass-weighted complementary cumulative distribution function (CCDF) for both density and column density for all four simulations at the three different output times. Note that we vary our line-styles based on the initial cloud velocities at the start of our simulations and vary the colour based on the three different output times.

**Table 3.3.** A table presenting the mean column density of all 6 simulations along with the percentage column above $1 \times 10^{21}$ cm$^{-2}$ and $1 \times 10^{22}$ cm$^{-2}$.

| ID | Mean column density [cm$^{-2}$] | % Column above $1 \times 10^{21}$ cm$^{-2}$ | % Column above $1 \times 10^{22}$ cm$^{-2}$ |
|---|---|---|---|
| A | 2.33e21 | 42.7 | 5.3 |
| B | 3.18e21 | 60.0 | 6.0 |
| C | 1.98e21 | 53.4 | 2.0 |
| D | 1.53e21 | 46.5 | 0.6 |
| E | 2.52e21 | 43.0 | 4.2 |
| F | 2.48e21 | 46.2 | 4.5 |

formed we take a 10 pc box region and post-proccess this region through RADMC-3D.

In Figure 3.5, we present the evolution of the mass above different density thresholds ($n_{thr}$) as a function of time.

As in Section 3.3, we present the column densities of the six simulations in Figure 3.6. It appears if we simply look to Figure 3.6 that the column densities vary quite significantly from one simulation to another; the lower the ISRF (ID's C,D,E and F) the fewer the presence of high column density structures. This holds true apart from $G_0$ of 170, it appears to drop slightly, likely due to the high $G_0$ impacting the self-shielding of the core due to a higher photoionization rate.

However, although by appearance these simulations possess very different column densities. One would expect a higher value of $G_0$ to struggle to form high

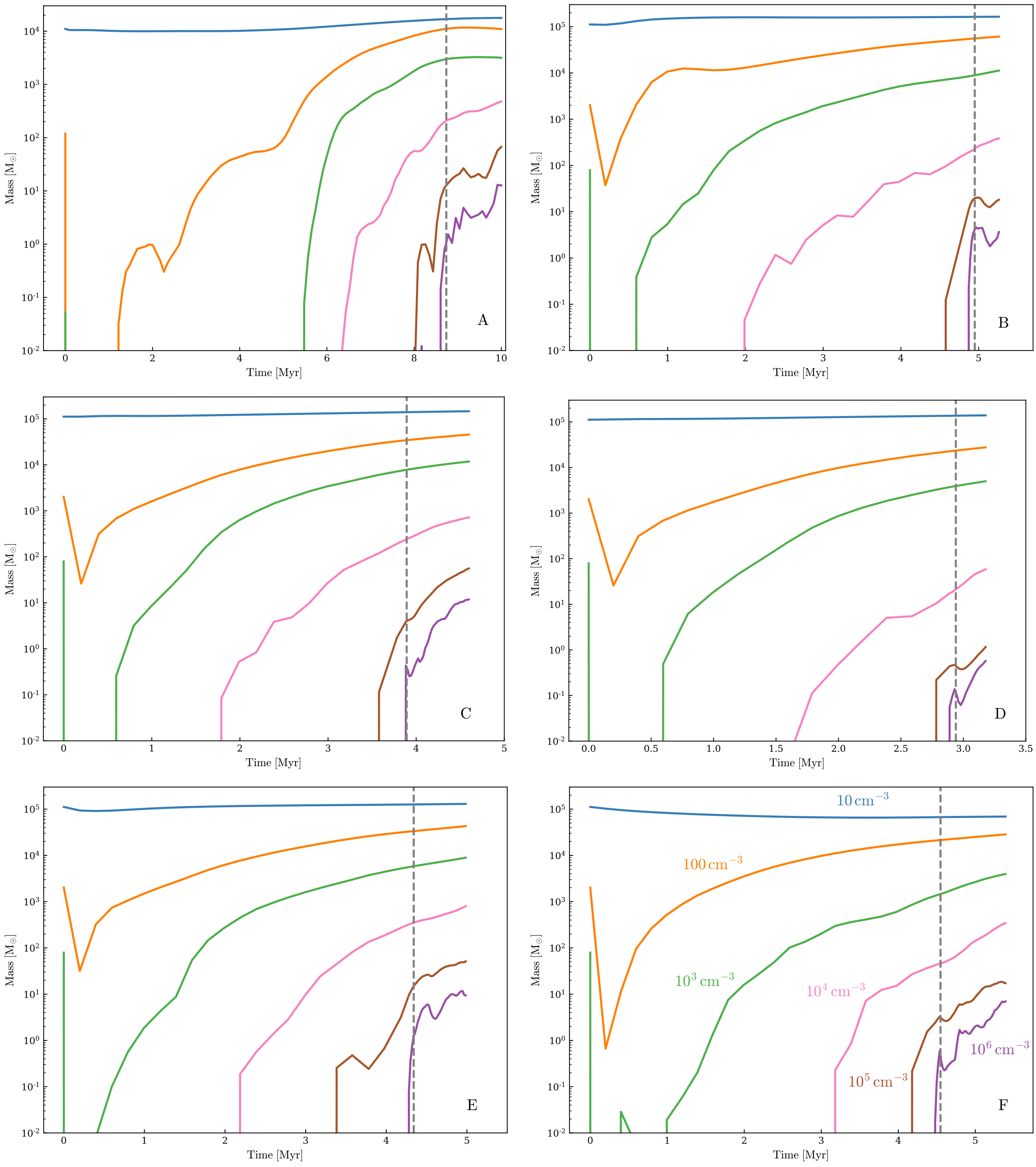

**Figure 3.5.** Evolution of mass of the gas within the simulations that lies above a given density threshold, which is labelled on the final plot. Each plot shows the evolution of mass with different variations in the starting parameters described in Table 3.2. Note that the gray, vertical line denotes the approximate time at which star formation occurs.

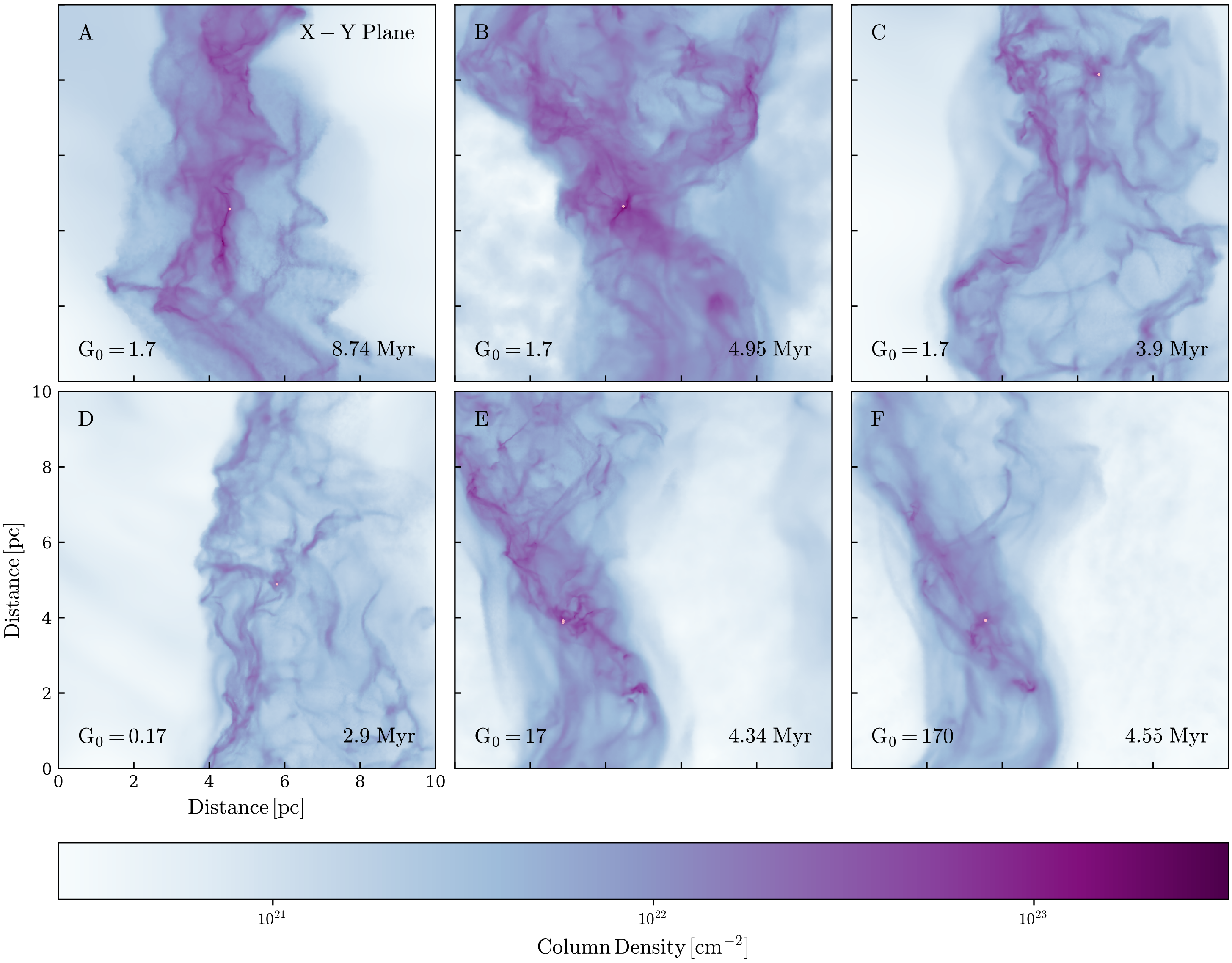

**Figure 3.6.** This grid of column densities shows the state of each simulation at the point in which star formation occurs. The sink particle locations are also included in any image that possess sink particles which are represented as pink points. Note that the alphabetical letters on each tile corresponds to the IDs in Table 3.2

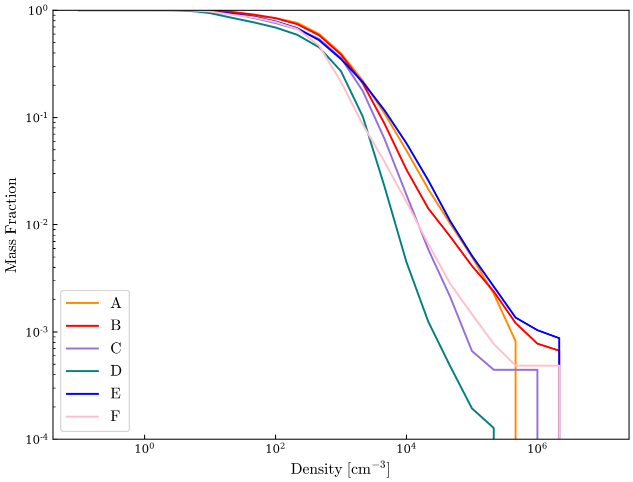

**Figure 3.7.** A normalized mass-weighted complementary cumulative distribution function (CCDF) for density where all simulations are labelled according to Table 3.2.

densities to to an increased thermal pressure in these dense regions, however, all results (from Table 3.3, Figures 3.6 and 3.7) indicate that these higher values of $G_0$ have no difficulties in forming these dense gas regions. In fact, both values of $G_0$ of 17 and 170 have a higher mean column density compared to $G_0$ of 1.7. Surprisingly we see that the percentage column above $1 \times 10^{21}$ cm$^{-2}$ and $1 \times 10^{22}$ cm$^{-2}$ for a $G_0$ of 170 is actually higher than for a $G_0$ of 17 and both $G_0$ values have over double the percentage of gas above $1 \times 10^{22}$ cm$^{-2}$ compared to a $G_0$ of 1.7. Both Table 3.3 and Figure 3.7 appear to be in agreement with one another showing that at least in these simulations there is a strong correlation between the column density and the volumetric density. Increasing the CRIR seems to increase significantly the higher column density structures, especially compared to the higher $G_0$ values. We do not see much of a difference in the composition of the density in Figure 3.7. However, what we do see is that lowering the value of $G_0$ has a far more significant impact on the distribution of density compared to increasing the value of $G_0$. A $G_0$ of 0.17 struggles to form mass above a density of $10^5$ cm$^{-3}$ unlike the other simulations which formed much more mass above the same density of $10^5$ cm$^{-3}$.

## 3.5 DISCUSSION

Although on face value the simulations of varying initial cloud velocity look very similar to the simulations of varying ISRF by simply looking at Figures 3.3 and 3.6, we can see that they are in fact quite different if we look at the normalized mass-weighted complementary cumulative distribution function (CCDF) for all 10 simulations (Figures 3.4 and 3.7). It is clear that varying the initial collisional velocity has a greater impact on the density distribution in the simulations compared to the variations in the ISRF strength.

We notice in Figure 3.1 and 3.5 that there are regular separations between the formation of gas with densities above $10^2$, $10^3$ and $10^4$ $\mathrm{cm}^{-3}$. However, when we look at the time it takes for gas with densities above $10^5$ $\mathrm{cm}^{-3}$ to form, it typically takes longer than expected especially if these clouds fall at some free-fall rate. And as soon as gas with densities above $10^5$ $\mathrm{cm}^{-3}$ are formed, these simulations typically form gas with densities above $10^6$ $\mathrm{cm}^{-3}$ very quickly. This brings up the question of why observers such as Wu et al. (2010), Lada et al. (2010) and Lada et al. (2012) state that star formation occurs at densities above $10^4$ $\mathrm{cm}^{-3}$. It could be argued from these simulations that a density of $10^5$ $\mathrm{cm}^{-3}$ is much more reasonable point at which to say that these regions are bound to form stars because as soon as this point is reached it quickly cascades in the formation of denser gas (we would however need to examine how quickly it takes for gas above densities of $10^7$ and $10^8$ $\mathrm{cm}^{-3}$ to form to properly justify this).

Using the free-fall time calculated from $\mathrm{t_{ff}} = \sqrt{3\pi/32\mathrm{G}\rho}$, for a density of $10^4$ $\mathrm{cm}^{-3}$, we would get a $\mathrm{t_{ff}}$ of 0.51 Myr. This value of 0.51 Myr is much shorter than the typical time it takes for our simulations to go from the first formation of gas above densities of $10^4$ $\mathrm{cm}^{-3}$ to the densities of $10^5$ $\mathrm{cm}^{-3}$. This therefore suggest that either; the use of free-fall time in observational studies such as Krumholz & Tan (2007) is unrealistic and that there are properties that hinder this free-fall time such as turbulent flows in these dense gas regions. Or that as suggested previously, the density at which star formation occurs should instead of being at a density of $10^4$ $\mathrm{cm}^{-3}$ as Wu et al. (2010) suggests, but at a density of $10^5$ $\mathrm{cm}^{-3}$. Since at a density of $10^5$ $\mathrm{cm}^{-3}$, we get a free-fall time of $\mathrm{t_{ff}}$ of 0.16 Myr, which is often larger than the time between the formation of densities above $10^5$ $\mathrm{cm}^{-3}$ and densities of $10^6$ $\mathrm{cm}^{-3}$ in our simulations.

## 3.6 CONCLUSION

We present 10 simulations run in AREPO, 4 simulations exploring the variation in the cloud-cloud collisional speed and 6 simulations exploring the variation of ISRF strength through varying the UV radiation strength expressed as $\mathrm{G_0}$ and the CRIR. We find that the increase in the ISRF strength provides little to no difficulty in the formation of these dense regions compared to a standard value of $\mathrm{G_0}$ of 1.7, which is surprising considering the increased thermal pressure likely to be present in these higher ISRF simulations. However, a lower value of $\mathrm{G_0}$ of 0.17 struggles to produce high density regions.

We argue that our simulations indicate that the use of a density threshold of $10^4$ cm$^{-3}$ for star formation is too low and that due to the combination of the free-fall time being much shorter than the time it takes to go from the formation of densities of $10^4$ cm$^{-3}$ to densities of $10^5$ cm$^{-3}$ and the ability to easily destroy gas of densities of $10^4$ cm$^{-3}$ through high collisional cloud velocities. A density of $10^5$ cm$^{-3}$ appears to be a more reasonable point at which star formation occurs. Each simulation was able to form sink particles and therefore able to reach the star formation stage. Each simulation appeared to be able to produce a dynamically unique environment that can be used for our synthetic observations in Sections 4 and 5.

# CHAPTER 4

# AN INVESTIGATION INTO THE EFFECTIVE DENSITY OF HCN

This chapter presents an investigation into the effective density of HCN along with the relationship between HCN/CO line emission ratio and dense gas. This work is published in Jones et al. (2023)

## 4.1 INTRODUCTION

A central goal of star formation theory is to predict the rate at which gas in the interstellar medium (ISM) is converted into stars, and so research into this field has focused on measuring the amount of gas present to form stars, and connecting that to the amount of star formation that actually occurs. Perhaps the most widely-studied relation is that between the surface density of the star formation rate, and the surface density of gas, known as the Kennicutt - Schmidt (K-S) relation (Schmidt, 1959; Kennicutt, 1989),

$$\Sigma_{\mathrm{SFR}} \propto \Sigma_{\mathrm{gas}}^{\mathrm{N}} \quad . \tag{4.1}$$

Kennicutt (1989) found N to be $1.4 \pm 0.15$, however there has been some debate over the value of the index since (Bigiel et al., 2010; Shetty et al., 2014). Simple arguments for the KS relation have been presented by several authors (Elmegreen, 1994; Wong & Blitz, 2002; Krumholz & Tan, 2007), revolving around the idea that a roughly constant fraction of the gas present in molecular clouds will be converted into stars each free-fall time. With $\mathrm{t_{ff}} \propto \rho^{-0.5}$, we would expect $\dot{\rho} \propto \rho^{1.5}$ and with an assumption that scale heights of galaxies do not vary significantly we can come to the conclusion that $\Sigma_{\mathrm{SFR}} \propto \Sigma_{\mathrm{gas}}^{1.5}$.

However the interpretation of the K-S relation is more complicated when we start to consider what "gas available for star formation" actually means. The early study by Kennicutt (1989) used CO emission to trace the gas surface density. Later studies (Bigiel et al., 2010; Shetty et al., 2014) that also focus on CO emission suggested lower values of the K-S index, towards $N \approx 1$ (although this too is under debate: Kennicutt & Evans, 2012).

As one moves to progressively higher density gas tracers, one would expect the correlation between the mass of the gas present and star formation rate to become tighter, provided that the star formation is being measured on time-scales similar to the free-fall time of the gas tracer (see the work by Kruijssen et al. (2014) for a discussion of the time-scales). For example, Gao & Solomon (2004a,b) conducted a K-S study using HCN $\mathrm{J} = 1-0$ line emission, which is assumed to trace higher density gas than CO, and found that $\mathrm{L_{FIR}} \propto \mathrm{L_{HCN}}$. This implies that $\Sigma_{\mathrm{SFR}} \propto \Sigma_{\mathrm{gas}}$, and so for HCN emission the K-S index is around 1. Wu et al. (2005) suggested that the HCN emission from a galaxy simply counts the number of star-forming clumps present in these galaxies, and so HCN is primarily tracing the densities at which star formation "sets in". This has spawned significant interest in HCN as a tracer of "dense gas" in the ISM, and as a tool for studying the star formation relations in more detail.

However, exactly what density HCN traces is still very much unclear. Although the critical density is quite high – $n_{\mathrm{crit}} = 4.7 \times 10^5\,\mathrm{cm^{-3}}$ for the multi-level definition of the critical density at 10K – the line is typically optically thick, which can lower the effective critical density, as discussed in detail by Shirley (2015). Indeed, Shirley (2015), using simple one-dimensional radiative transfer, demonstrates that a 1 $\mathrm{K\,km\,s^{-1}}$ line can be produced by densities as low as $8.4 \times 10^3$ $\mathrm{cm^{-3}}$, due to radiative trapping. This is below the density that HCN was assumed to trace in the studies of Gao & Solomon (2004a,b), where they calculated that HCN emission was probing a characteristic density of $3 \times 10^4$ $\mathrm{cm^{-3}}$.

Krumholz & Thompson (2007) investigated how the KS law changes with differing molecular gas tracers, including HCN (Nguyen et al., 1992; Gao & Solomon, 2004a,b; Riechers et al., 2006; Gao et al., 2007). Similar to Gao & Solomon (2004b), their model uses an LVG calculation but with the inclusion of a lognormal PDF for the density in the molecular gas in their model. With this approach they found that HCN emission generally traces dense gas, $\mathrm{n_{dense}} \sim 10^5$ $\mathrm{cm^{-3}}$. Their model showed a strong correlation with the observed data with a direct proportionality between far infrared luminosity and HCN luminosity.

More recently, Leroy et al. 2017 have used LVG calculations to explore the influence of the density PDF on the characteristic density traced by HCN emission. They found that the characteristic density is highly sensitive to what one assumes regarding the cloud density PDF, with values from their models ranging from $\sim 10^3\,\mathrm{cm}^{-3}$ to more than $10^5\,\mathrm{cm}^{-3}$. However, one weakness of this and the other simple models described above is that they incorporate little or no information on the spatial distribution of the dense gas, which potentially has a large impact on the relation between HCN optical depth and gas density. A first attempt to properly account for the spatial structure of the dense gas was made by Onus et al. 2018, who post-processed a high resolution simulation of a small portion of a molecular cloud by Federrath 2015. Based on this calculation, they predicted that HCN emission traces gas with a luminosity-weighted mean density of $0.8 - 1.7 \times 10^4\,\mathrm{cm}^{-3}$.

There is also increasing evidence from observational studies of giant molecular clouds (GMCs) in the Milky Way that HCN is probing lower densities than previous assumed. Pety et al. (2017), Kauffmann et al. (2017) and Barnes et al. (2020) have shown that HCN also traces diffuse regions of molecular clouds at a density of $\sim 500\,\mathrm{cm}^{-3}$, $\sim 10^3\,\mathrm{cm}^{-3}$ and $\sim 10^3\,\mathrm{cm}^{-3}$, respectively. Tafalla et al. (2021) also show that HCN emission can be detected at visual extinctions ($\mathrm{A_V}$) as low as $\sim 1\,\mathrm{mag}$.

In this section, we will expand upon the work of Onus et al. (2018). First, rather than simulating a small sub-region within a cloud, we will use simulations of low-density 'cloud-cloud collisions' (from section 3), to create dense molecular regions with self-consistent density and velocity fields. Second we will use a detailed model of the heating and cooling processes that is coupled to a time-dependent chemical network that follows $H_2$ and CO formation and destruction. Although we do not follow the HCN chemistry self-consistently in our study, we will use the results from Fuente et al. (2019) to relate the HCN abundance at each point in the simulation volume to the CO abundance and the local visual extinction – two properties that are followed self-consistently in our simulations. We perform radiative transfer (RT) post-processing on the simulations with the publicly available code RADMC-3D (Dullemond et al., 2012) to make synthetic observations of the HCN (1-0) line, and we use these to explore the density regime traced by HCN emission. Where possible, we have compared to the recent observational studies.

## 4.2 Numerical Approach

We investigate two spherical clouds that collide head-on at four different velocities using a magnetohydrodynamical (MHD) code that includes a time-dependent chemical network for $H_2$ and CO formation, which runs alongside a detailed treatment of the heating and cooling in the ISM. we then post-process our simulations using a synthesised HCN abundance, which is related to the CO abundance in our

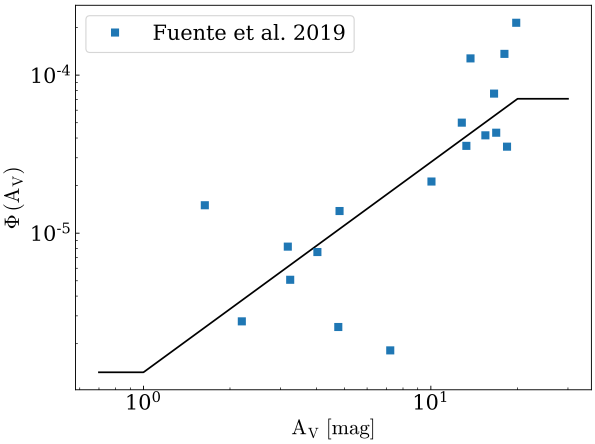

**Figure 4.1.** Our conversion factor from CO abundance to HCN abundance, $\Phi\,(A_V)$ (black line), together with the observational measurements of the HCN to CO ratio presented in Fuente et al. 2019 (blue squares)

models (see section 4.2.2 for further details), and a radiative transfer code to create HCN emission position-position-velocity (PPV) cubes. These are then analysed to determine the density regime traced by HCN emission.

### 4.2.1 THE NUMERICAL MODEL

We use a modified version of the publicly available moving-mesh code, AREPO (Springel, 2010; Weinberger et al., 2020). The adpative, moving mesh in AREPO allows us complete control over the resolution in our simulations, while at the same time minimising advection errors. It is thus ideally suited to this type of ISM problem. Our modifications to AREPO include: the use of the radiative heating and cooling and cosmic ray heating treatments described by Glover & Mac Low (2007); Glover & Clark (2012a); the TREECOL algorithm developed by Clark et al. (2012) to calculate the attenuation of the interstellar radiation field (ISRF); time-dependent chemistry that follows $H_2$ and CO formation (see Hunter et al. 2021); a sink particle algorithm (Bate et al., 1995; Federrath et al., 2010) to treat small, gravitationally-collapsing regions associated with star formation (Tress et al., 2020; Wollenberg et al., 2020).

### 4.2.2 RADIATIVE TRANSFER POST-PROCESSING

We use the RADMC-3D radiative transfer (RT) code (Dullemond et al., 2012) to create post-processed position-position-velocity (PPV) cubes of HCN emission from our AREPO simulations. We make use of internal functions in AREPO to create a regular cartesian grid of fluid properties that can be converted to a form that is compatible with the fixed cartesian grid used by RADMC-3D. This means however, that we cannot perform the RT post-processing on the entire computational domain that is evolved in AREPO. We therefore limit our RT analysis to a 10 pc cubic region that envelopes the highest density region in the cloud-cloud collision; AREPO's voronoi mesh is interpolated on to a $450^3$ grid such that we have a spatial resolution of 0.022 pc in the RT. This is sufficient to capture both the scales of the molecular cloud and the cores that form within.

Due to the complex nature of nitrogen chemistry, it is currently computationally intractable to self-consistently compute the time-dependent abundance of HCN in our AREPO chemical network. We therefore make use of the observationally-derived $x_{\rm HCN}/x_{\rm CO}$ v $\rm A_V$ relation shown in Figure 8 of Fuente et al. (2019). Note that other interpretations of the data in Fuente et al. (2019) are possible. For example from their Figure 6, one could infer that $x_{\rm HCN}$ is proportional to $\rm A_V$ above $\rm A_V \approx 10$, and flat below this. However by tying the HCN abundance to the CO abundance, we can capture (phenomenologically) the effects of the photo-destruction of the HCN by the ISRF, and thus avoid spuriously large HCN abundances at low densities and $\rm A_V$.

When using the $x_{\rm HCN}/x_{\rm CO}$ v $\rm A_V$ relation in Fuente et al (2019), our visual extinction is calculated along the same line of sight as the rays used to solve the RT problem in RADMC-3D, simply by first getting the column density at each point via,

$$\rm N_H = \sum_{i=0}^{N_{LoS}} \frac{\rho_i}{1.4\,m_p} \Delta L \quad , \tag{4.2}$$

where $i$ denotes each of the $N_{\rm LoS}$ cells along the line-of-sight, with densities $\rho_i$ and length $\Delta L$; the term $1.4\rm m_p$ converts to the number density of hydrogen nuclei. We then convert this to a visual extinction via,

$$\rm A_V = \frac{N_H}{1.87 \times 10^{21} cm^{-2}} \quad , \tag{4.3}$$

where here $\rm N_H$ is the column number density of hydrogen *nuclei* (Bohlin et al., 1978; Draine & Bertoldi, 1996). The column density thus derived is designed to mimic the observed column density used in Figure 8 of Fuente et al. (2019). Note that this differs from the column density as seen by each cell in our simulation, which is derived via our TREECOL algorithm.

Using this relationship, our computed CO abundances derived using AREPO can then be used to calculate our HCN abundance with respect to hydrogen nuclei.

We then compute the HCN abundance in each RADMC-3D grid cell via,

$$x_{\mathrm{HCN}} = \Phi\left(\mathrm{A_V}\right) \cdot x_{\mathrm{CO}} \quad , \tag{4.4}$$

where $\Phi\left(\mathrm{A_V}\right)$ is our conversion factor from CO abundance to HCN abundance, $x_{\mathrm{HCN}}$ is the abundance of HCN relative to hydrogen nuclei and $x_{\mathrm{CO}}$ is the abundance of CO also relative to hydrogen nuclei. The value of $\Phi\left(\mathrm{A_V}\right)$ is obtained from the Fuente et al. (2019) results, and we present the data used in Figure 4.1. Note that the data in Fuente et al. (2019) covers a limited range in $\mathrm{A_V}$. Rather than make up a relation outside these limits, we simply hold the conversion factor constant with increasing/decreasing $\mathrm{A_V}$. While one might expect this to cause problems at low $\mathrm{A_V}$ – potentially boosting the HCN abundance – in practise this does not happen, as at low $\mathrm{A_V}$ the CO abundance in any case self-consistently falls to zero due to our treatment of the photodissociation. Note that another caveat in our model is that the HCN formation timescale is assumed to be exactly equivalent to the CO formation timescale. Although this is unlikely to be exactly the case, the recent results from Priestley & Whitworth (2021) – which captured the non-equilibrium chemistry of a dynamically evolving cloud – demonstrate that both the CO and HCN formation timescales are shorter than the dynamical timescale in scenarios similar to those we study here. Thus our coupling of the HCN abundance to the CO abundance is unlikely to affect the results. Priestley & Whitworth (2020) found that a large variation in the distribution of the HCN abundance in the density space leads to very little variation in the intensity of HCN.

The level populations of HCN were calculated in RADMC-3D using the large velocity gradient (LVG) approximation (Sobolev, 1957) as implemented by Shetty et al. (2011). We use the collisional rate data for HCN provided by Leiden Atomic and Molecular Database (Schöier et al., 2005; Faure et al., 2007; Dumouchel et al., 2010). In this study, we use the version of the HCN line data without hyperfine structure, and we include excitation from two collisional partners, $H_2$ and electrons. The radiative transfer is performed along the $z$-axis of the grid (perpendicular to the axis of the cloud-cloud collision), such that the rays are directed from negative to positive $z$.

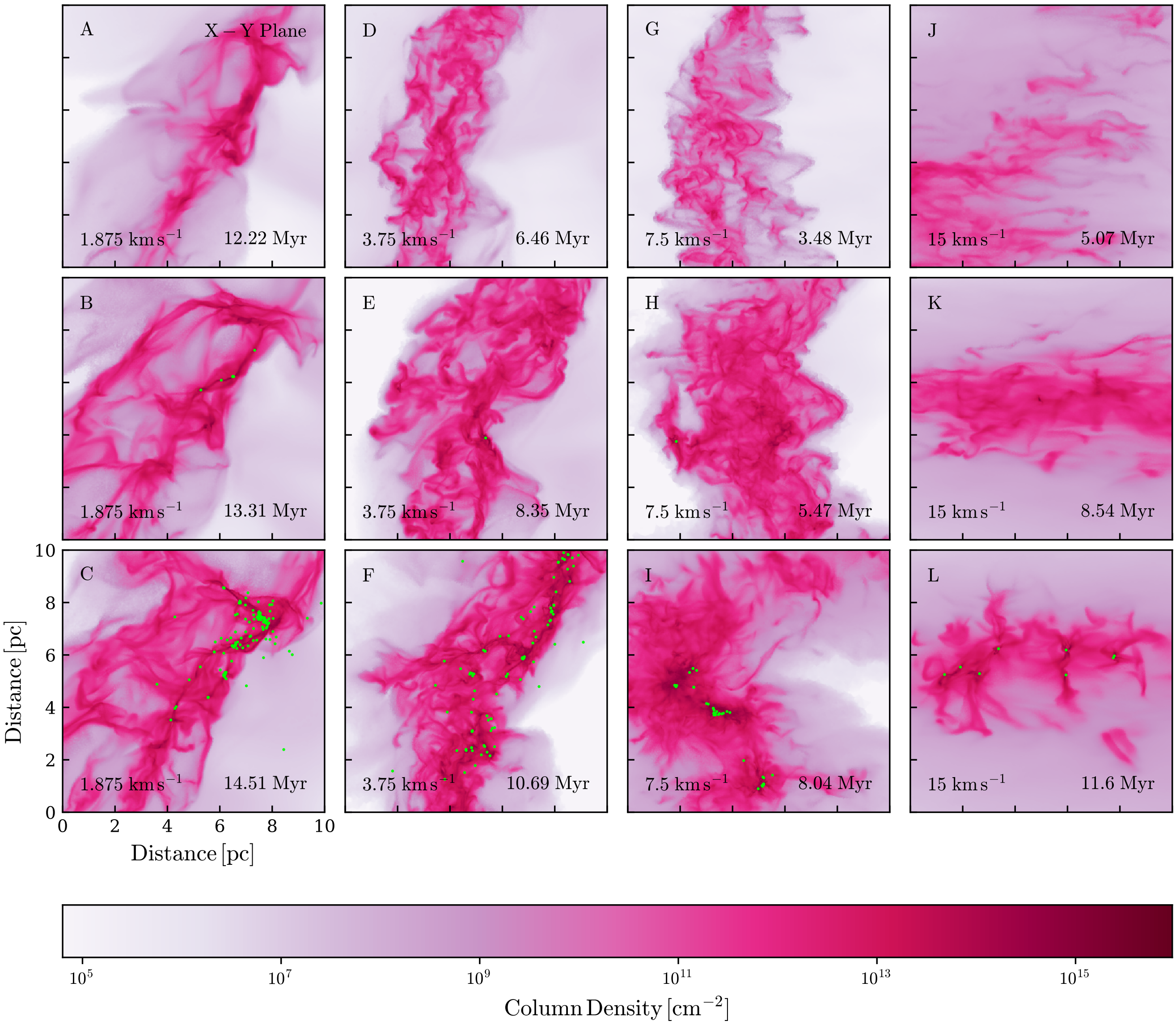

**Figure 4.2.** A grid of Column densities of HCN for all simulations presented in the same format as in Figure 3.3.

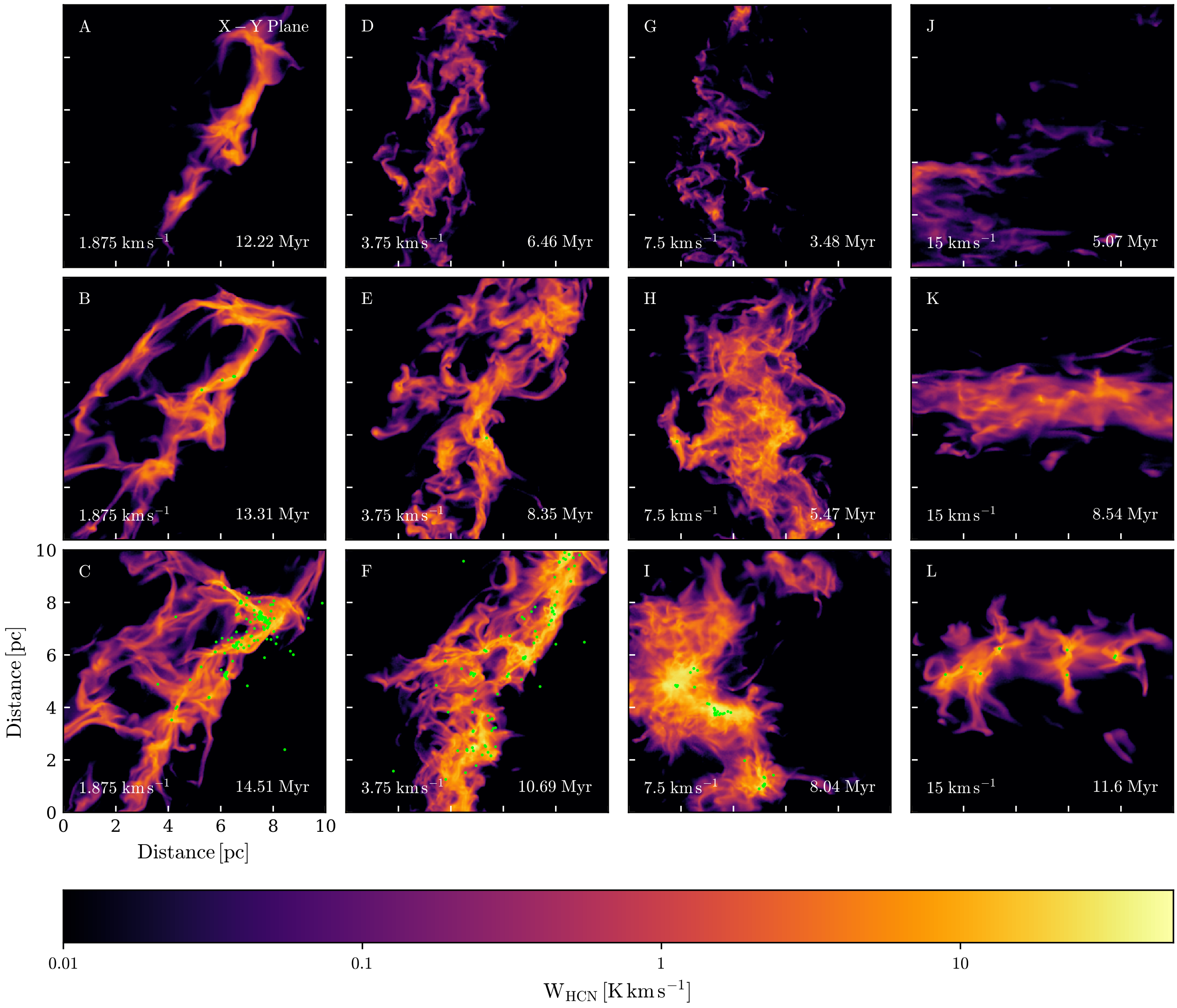

**Figure 4.3.** Maps of the velocity-integrated intensity in the $J = 1 \rightarrow 0$ line of HCN, $W_{\mathrm{HCN}}$, at the three simulation times and the four initial velocities that were used in Figure 3.3. Note that the alphabetical letters on each tile corresponds to the IDs in Table 4.1.

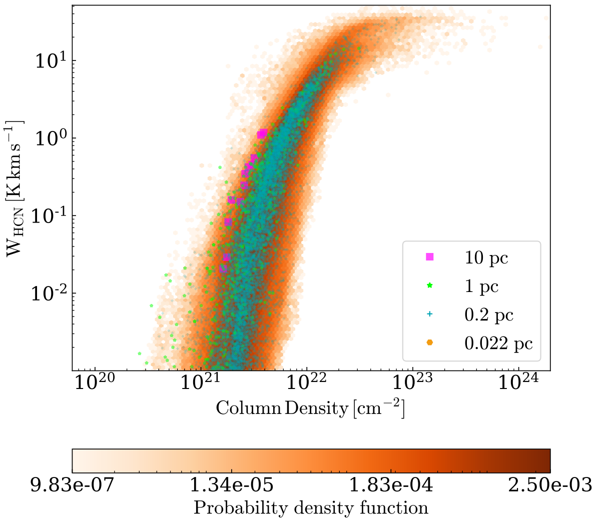

**Figure 4.4.** Velocity-integrated intensity in the J = 1 → 0 line of HCN, $W_{HCN}$, plotted against the column density for all simulations collated into one figure. We also demonstrate what happens if we degrade the spatial resolution of the PPV cubes to 0.2, 1 or 10 pc.

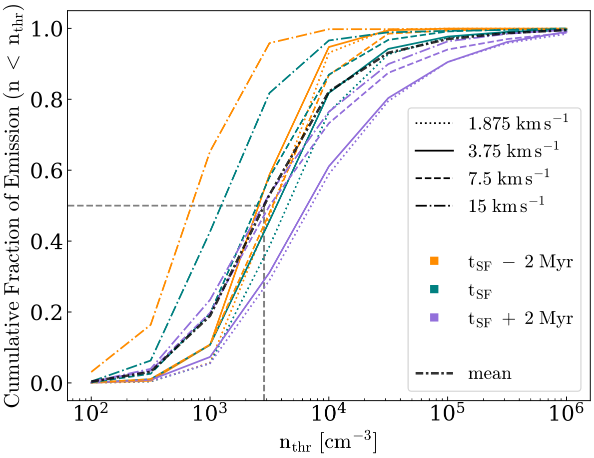

**Figure 4.5.** Cumulative fraction of emission of HCN plotted as a function of density for all four simulations at the three different output times. Note that we use the same stylistic format as Figure 3.4. Also included is the mean cumulative fraction of emission (densely dashdotted black line), plotted as a function of density. The dashed grey line indicates the mean value of the characteristic density, $n_{char} = 2.9 \times 10^3$ cm$^{-3}$.

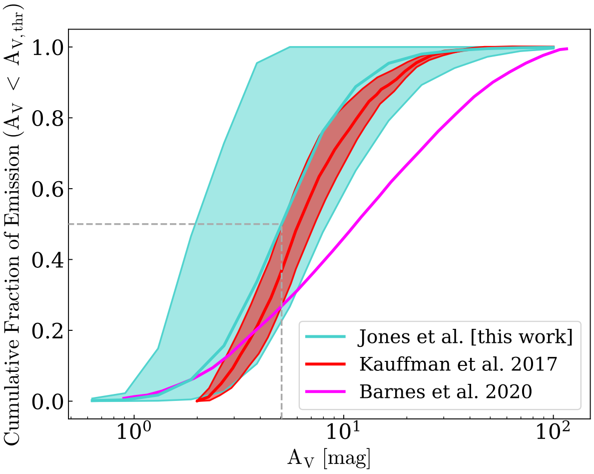

**Figure 4.6.** Cumulative emission of HCN plotted as a function of $A_V$ with the mean, minimum and maximum cumulative emission from all twelve simulations. We include the cumulative emission of HCN from Kauffmann et al. (2017) and Barnes et al. (2020) for comparison.

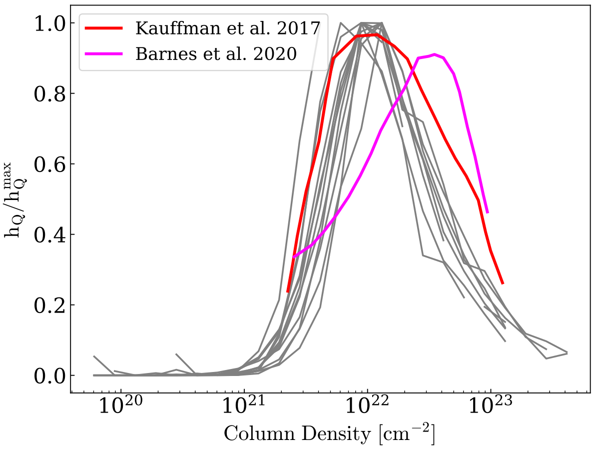

**Figure 4.7.** A normalized ratio of the integrated intensity to the column density, $h_{HCN}/h_{HCN}^{max}$, where $h_{HCN} = W_{HCN}/N_{H_2}$, as a function of column density. All of our twelve simulations are grey for clarity. We include Kauffmann et al. (2017) and Barnes et al. (2020) for comparison.

**Table 4.1.** A brief overview of all twelve cases that were post-processed through RADMC-3D. The time denotes the time at which the simulation has evolved to before being post-processed through RADMC-3D.

| ID | Initial velocity | Time | Mass | HCN luminosity | $W_{\mathrm{HCN}}^{\mathrm{mean}}$ | Fraction of mass above | |
|---|---|---|---|---|---|---|---|
| | | | | | | $2.85 \times 10^3$ cm$^{-3}$ | $3 \times 10^4$ cm$^{-3}$ |
| | [km s$^{-1}$] | [Myr] | [M$_\odot$] | [K km s$^{-1}$ pc$^2$] | [K km s$^{-1}$] | [%] | [%] |
| A | 1.875 | 12.22 | 2176.49 | 15.92 | 0.16 | 9.37 | 0.02 |
| B | 1.875 | 13.31 | 2929.12 | 34.67 | 0.35 | 19.36 | 1.78 |
| C | 1.875 | 14.51 | 3590.91 | 55.43 | 0.55 | 27.11 | 5.69 |
| D | 3.75 | 6.46 | 2026.82 | 8.28 | 0.08 | 6.65 | 0.03 |
| E | 3.75 | 8.35 | 3153.03 | 42.40 | 0.42 | 18.18 | 1.52 |
| F | 3.75 | 10.69 | 4129.07 | 109.79 | 1.09 | 35.23 | 8.69 |
| G | 7.5 | 3.48 | 1971.21 | 2.93 | 0.03 | 6.61 | 0.03 |
| H | 7.5 | 5.47 | 3414.21 | 45.39 | 0.45 | 13.71 | 0.69 |
| I | 7.5 | 8.04 | 4380.66 | 118.16 | 1.18 | 25.28 | 6.92 |
| J | 15 | 5.07 | 1817.20 | 2.14 | 0.02 | 0.19 | 0.00 |
| K | 15 | 8.54 | 2636.88 | 15.15 | 0.15 | 2.82 | 0.17 |
| L | 15 | 11.60 | 2867.27 | 24.60 | 0.25 | 9.35 | 1.70 |

## 4.3 HCN EMISSION FROM OUR CLOUDS

### 4.3.1 THE DENSITY REGIME PROBED BY HCN EMISSION

To get a better sense of the formation of the HCN in our simulations, we present a HCN column density in Figure 4.2 that is from the resulting application of Equation 4.4 to our CO data in our simulation to generate our HCN abundances combined with Figure 3.3.

Using the post-processed HCN abundances generated from AREPO, we create PPV cubes of the HCN ($J = 1 \rightarrow 0$) line emission using RADMC-3D for all twelve regions (three different times for each of our four simulations). All RADMC-3D simulations track the spectrum between $-3$ to 3 $\mathrm{km\,s^{-1}}$ in 0.02 $\mathrm{km\,s^{-1}}$ increments; this is sufficient to completely cover the range of velocities along the $z$ direction in each of our 10pc boxes, while allowing us to model the thermal line-width with around ten points.

From these PPV cubes, we create velocity-integrated intensity maps of HCN, which can be seen in Figure 5.1. The contribution of each column density of gas has on the HCN emission can be seen in Figure 4.4 and we see that as the column density increases the intensity of HCN emission also increases. It appears that HCN is above the observationally detectable limits of $\sim 0.1$ K $\mathrm{km\,s^{-1}}$ only above a column density of $\sim 3 \times 10^{21}\mathrm{cm^{-2}}$, which is roughly an order of magnitude higher than our lower threshold on the CO to HCN conversion in Figure 4.1. A similar behaviour in the HCN emission is reported by Pety et al. (2017), Kauffmann et al. (2017) and Barnes et al. (2020) who find $\sim 50\%$ emission stemming from column densities below $9.7 \times 10^{21}$ $\mathrm{cm^{-2}}$, $1.2 \times 10^{22}$ $\mathrm{cm^{-2}}$ and $2.1 \times 10^{22}$ $\mathrm{cm^{-2}}$ respectively.

The inclusion of sink particles in our figures allows us to clearly demonstrate that the regions of active star formation are associated with bright HCN emission. However, upon looking at cases C and F (see Table 4.1), we also see sink particles without any HCN emission demonstrating that star forming clouds can evolve rapidly: stars can be ejected from their natal environments, and young clusters may also consume the available gas on the local free-fall time. Note that there is no feedback from the sink particles in our simulations.

The main goal of this section is to determine the density regime probed by HCN. We achieve this by manipulating the HCN abundance that goes into RADMC-3D. By artificially setting the HCN abundance in cells with a density below a certain threshold density, $\mathrm{n_{thr}}$, to zero in our RADMC-3D input cubes, and then performing the RT for the HCN line, we can determine the amount of HCN emission arising from gas with $n > \mathrm{n_{thr}}$. If we repeat this process, systemically varying $\mathrm{n_{thr}}$ from

$10^2$ to $10^6$ cm$^{-3}$, we can work out the inverse cumulative fraction of HCN emission with density for each cloud. This analysis is repeated for all twelve of the simulated regions studied in this section. However, it is standard to determine the cumulative fraction of emission i.e. the amount of HCN emission arising from gas with $n < \mathrm{n_{thr}}$. Therefore to do this we simply take one minus our inverse cumulative fraction of HCN.

The results of this process can be seen in Figure 4.5, in which the fraction of emission is given by the ratio of the HCN luminosity produced by gas below a certain density threshold, $\mathrm{n_{thr}}$, to that in the case where no threshold is applied – i.e. the HCN abundance is unchanged from the value derived from Equation 4.4. In Figure 4.5, we see $\sim$ 50% of HCN emission emanates from densities below $\sim 1 - 7 \times 10^3$ cm$^{-3}$, with the scatter depending on both the evolutionary stage of the cloud in the simulation, and the collision velocity (the former proving a slightly larger scatter). This result goes against many observational results that postulate that most of the emission stems from densities above $10^4$ cm$^{-3}$ such as Gao & Solomon (2004a); Krumholz & Tan (2007). However, our result agrees with the more recent observational studies such as Shirley (2015); Kauffmann et al. (2017); Pety et al. (2017); Harada et al. (2019); Tafalla et al. (2021).

We see a trend towards a higher fraction of emission coming from higher densities as the simulations evolve over time, as they are able to accumulate a higher fraction of dense gas (as shown in Figure 3.1). Therefore, one could argue that we could reach a point where the emission from dense gas overwhelmingly dominates. However, we see both observationally and through simulations that the fraction of gas above $10^4$cm$^{-3}$ is generally small (Kainulainen et al., 2009; Lada et al., 2010), at least outside the galactic centre (Longmore et al., 2013). It is therefore unclear if an environment with enough dense gas for the HCN emission to probe densities above $3 \times 10^4$ cm$^{-3}$ is common in galaxies like the Milky Way, outside "extreme" environments.

The idea that more dense gas equates to a higher threshold density for HCN emission actually breaks down as soon as we vary our cloud-cloud collision velocity. We see a trend of decreasing threshold density as we increase our initial cloud velocity, even though we generally see an increase in the mass of gas at higher densities as we increase the collision velocity (Figure 3.1). The reason behind this is simply that the fraction of mass residing at densities above $10^3$ cm$^{-3}$ decreases as the initial cloud velocity of the simulation increases (see Table 4.1). As we will see below, it is around this density that is best traced by HCN (1-0) emission.

We can compare our results to those of Kauffmann et al. (2017) by adopting

**Table 4.2.** Summary of our findings of both the characteristic density and characteristic visual extinction traced by HCN emission. For comparison, we also quote the values from two recent observational studies.

| Reference | $A_{V,char}$ [mag] | $n_{char}$ [$\times 10^3$ cm$^{-3}$] |
|---|---|---|
| Jones et al. [this section] | $5.05^{+3.36}_{-3.07}$ | $2.85^{+4.25}_{-2.15}$ |
| Kauffmann et al. (2017) | $6.1^{+1.2}_{-1.0}$ | $0.87^{+1.24}_{-0.55}$ |
| Barnes et al. (2020) | $11.9 \pm 1.1$ | $3.4 \pm 2.8$ |

their definition of the 'characteristic density', $n_{char}$, which is the density below which half of the total integrated intensity arises, i.e. $W_{HCN}$ ($n < n_{thr}$) / $W_{HCN,Total} = 50\%$. From the data in Figure 4.5, we determine that $n_{char}$ is $2.85^{+4.25}_{-2.15} \times 10^3$ cm$^{-3}$ for our suite of simulations (i.e. taking the mean from all our RT modelling). Our characteristic density lies in between those derived for Orion A – $0.87^{+1.24}_{-0.55} \times 10^3$ cm$^{-3}$ (Kauffmann et al., 2017) – and W49 – $3.4 \pm 2.8 \times 10^3$ cm$^{-3}$ (Barnes et al., 2020) .

A further comparison between our work and both Kauffmann et al. (2017) and Barnes et al. (2020), can be made by looking at the cumulative fraction of emission as a function of $A_V$. Our column densities are derived by integrating along the $z$-direction in the RADMC-3D density cubes, to ensure that it is consistent with the 3D structure used in the RT (as opposed to deriving it straight from AREPO's more detailed Voronoi grid). The resulting column densities are then converted to $A_V$ using Equation 4.3. The cumulative total emission as a function of $A_V$ is given in Figure 4.6. We find that our results are closer to those found for Orion A by Kauffmann et al. (2017), than the results from W49 by Barnes et al. (2020). We discuss this further in Section 4.5.

We can perform a similar analysis for the characteristic visual extinction, and define $A_{V,char}$, where $A_V$ contains half the total integrated intensity, or $W_{HCN}$ ($A_V < A_{V,thr}$) / $W_{HCN,Total} = 50\%$. From the data used to compile Figure 4.6, we determine $A_{V,char}$ to be $5.05^{+3.36}_{-3.07}$ mag.

While our value of $A_{V,char}$ is consistent with that from Orion A, we can see from Figure 4.6 that our simulations are not consistent with the data from W49. The fact that we see a different relation to Barnes et al. (2020) is not that surprising. First, their resolution is much cruder, nearly $\sim 3$ pc, yet they report high gas column densities. Given the low resolution, their high column density regions are likely probing much higher densities than in the Orion A observations, to compensate for the low densities that are likely mixed into emission within the beam. Second, W49 is a much denser region than those we study here, and so likely contains more gas at high densities than our clouds. Another big difference between W49 and the

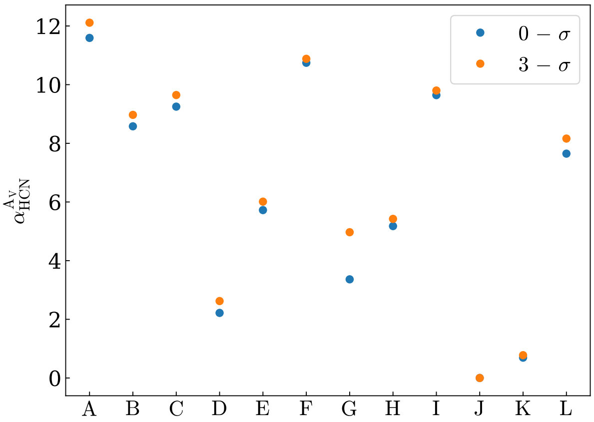

**Figure 4.8.** The conversion factor, $\alpha_{\mathrm{HCN}}^{\mathrm{A_V}}$, in each of the twelve cases considered in this section. Note that the conversion factors here correspond to the use of an $\mathrm{A_V}$ above 8 mag as seen in Equation 4.6. Here, the ID's of each simulation corresponding to Table 4.1 are given. The orange points show the values we obtain if we restrict the calculation to pixels where HCN is detected with signal-to-noise $>$ 3 for an assumed noise level $\sigma = 0.1$ ($\mathrm{K\,km\,s^{-1}}$). The blue points show the result in the ideal noise-free case. We see that in most cases, the inclusion of a realistic amount of noise makes very little difference to the derived value of $\alpha_{\mathrm{HCN}}^{\mathrm{A_V}}$.

clouds modelled here is cloud mass. Our total available mass is $2 \times 10^4$ $\mathrm{M_\odot}$, of which $\sim 10-20\,\%$ is in the region we study. On the other hand, the mass of the region Barnes et al. (2020) map in W49 is $\sim 2 \times 10^5$ $\mathrm{M_\odot}$, and the mass of the entire W49 complex is larger still, $\sim 10^6$ $\mathrm{M_\odot}$.

Finally, the observations of W49A focused around the star-forming region of W49A and not the entire W49 region. As noted by Pety et al. (2017), HCN is sensitive to far-UV radiation that is produced from star formation. Our ISRF with $\mathrm{G_0} = 1.7$ is hence not representative of the radiation field found in the massive star forming region of W49A. In contrast we see a good comparison with the data from Kauffmann et al. (2017), where the spatial resolution is very similar to that in our study: roughly $\sim 0.02$ pc in this work, compared to $\sim 0.05$ pc in the case of the Orion A observations. Along with Kauffmann et al. (2017) and Barnes et al. (2020), we see that our data is also consistent to that of Pety et al. (2017).

Finally, we can follow the analysis in Kauffmann et al. (2017) by examining the emission efficiency ratio, $\mathrm{h_{HCN}} = \mathrm{W_{HCN}/N_{H_2}}$. In Figure 4.7, we see the normalized ratio of the integrated intensity to the column density [or $\mathrm{h_{HCN}/h_{HCN}^{max}}$] as a function of column density. We see a clear trend with all of our simulations in that they all peak at around a column density of $10^{22}$ $\mathrm{cm^{-2}}$ which is roughly equivalent to $\mathrm{A_V} =$ 5 mag which is again comparable to our findings above.

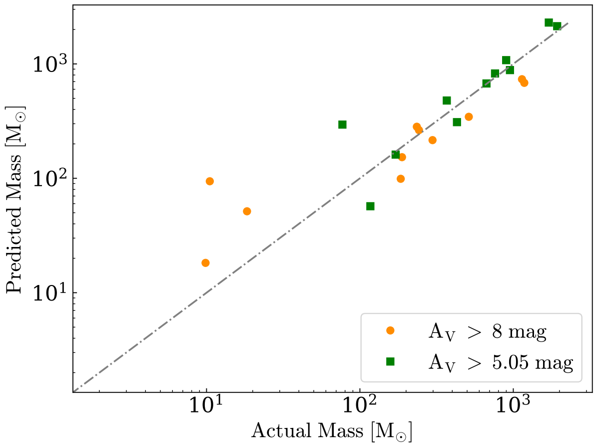

**Figure 4.9.** A plot of predicted mass for all simulations using a re-arranged version of equation 4.6 where $\alpha_{\rm HCN} = 6.79\ {\rm M_\odot}\,({\rm K\,km\,s^{-1}\,pc^2})^{-1}$ for $A_V > 8$ mag compared to the actual mass calculated within regions of $A_V > 8$ mag and $\alpha_{\rm HCN} = 19.46\ {\rm M_\odot}\,({\rm K\,km\,s^{-1}\,pc^2})^{-1}$ for $A_V > 5.05$ mag compared to the actual mass calculated within regions of $A_V > 5.05$ mag. The dashed line denotes the point at which the predicted mass is equivalent to the actual mass.

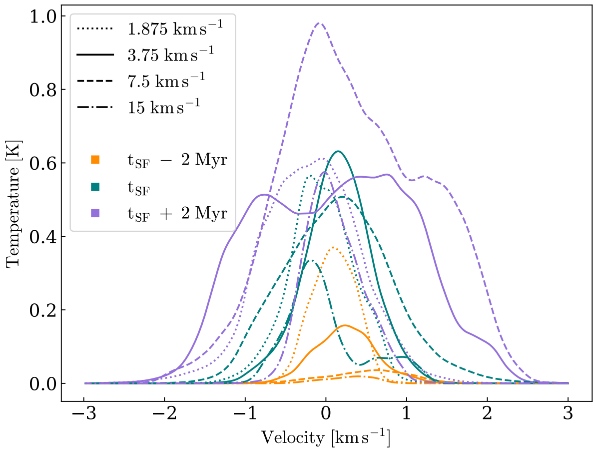

**Figure 4.10.** HCN (1-0) spectra of all simulations. The lines styles and colours are the same as Figure 3.4. We take the mean emission of our entire 10pc box. This is repeated for all velocity channels for all simulations to produce the observed spectra.

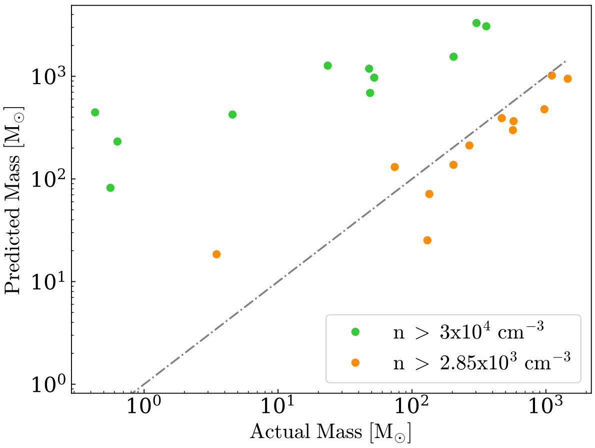

**Figure 4.11.** A plot of predicted mass for all simulations using Equation 4.7 for our density threshold of $2.85 \times 10^3$ cm$^{-3}$ and Gao & Solomon (2004a) density threshold of $3 \times 10^4$ cm$^{-3}$ compared to the actual mass calculated above these two density thresholds. The dashed line denotes the point at which the predicted mass is equivalent to the actual mass.

### 4.3.2 USING HCN EMISSION TO DETERMINE THE MASS OF 'DENSE' GAS

HCN emission has been used as way of tracing 'dense' gas in molecular clouds, with a conversion factor of the form,

$$\alpha_{\rm HCN} = {\rm M_{dg}/L_{HCN}} \ , \tag{4.5}$$

where $\alpha_{\rm HCN}$ is units of $\rm M_\odot\,(K\,km\,s^{-1}\,pc^2)^{-1}$. The typically adopted value is $\alpha_{\rm HCN} \sim 10{\rm M_\odot}\,({\rm K\,km\,s^{-1}\,pc^2})^{-1}$ (Gao & Solomon, 2004b). As already discussed, there is some uncertainty as to what exactly 'dense' means here, with (somewhat confusingly) both definitions based on volume and column density being used in the literature, as well as uncertainty over the value of the density being used in each case. In this section we explore both the column density ($\alpha_{\rm HCN}^{\rm A_V}$) and volume density ($\alpha_{\rm HCN}^{n_{\rm thr}}$) versions of this conversion factor.

We start our discussion by looking at the conversion factors based on column density, or in this case visual extinction, such as explored by Kauffmann et al. (2017); Evans et al. (2020); Barnes et al. (2020). For clarity we will define,

$$\alpha_{\rm HCN}^{\rm A_V} = {\rm M_{A_V > 8\,mag}/L_{HCN}} \ , \tag{4.6}$$

where $\rm M_{A_V > 8\,mag}$ is the mass residing above an $\rm A_V > 8$mag, as given in Evans et al.

(2020) and Barnes et al. (2020). This is in keeping with the result from Lada et al. (2010, 2012), who defined a “threshold” surface density of 8 mag above which the vast majority of dense cores are found. Note however that Kauffmann et al. (2017) uses a visual extinction of 7 mag in their analysis.

In Figure 4.8 we present the conversion factor, $\alpha_{\rm HCN}^{\rm A_V}$, as derived from our simulation data, adopting the definition given in Equation 4.6. To mimic the effects of limited observational sensitivity, we only consider pixels of integrated emission – and thus the corresponding pixels in the column density ($\rm A_V$) maps – that would be detected with a signal-to-noise greater than 3 for an assumed uniform noise level of $\sigma = 0.1$ ($\rm K\,km\,s^{-1}$). For comparison, we also show the results in the noise-free case.

It is clear from Figure 4.8 that there is a broad scatter in the values of $\alpha_{\rm HCN}^{\rm A_V}$ derived from our simulations, and that the values are largely unaffected by the choice of $\sigma$. We therefore ignore the effect of $\sigma$ on our analysis. The mean value of $\alpha_{\rm HCN}^{\rm A_V}$ from our suite of simulations is $\alpha_{\rm HCN}^{\rm A_V} = 6.79\ \rm M_\odot\,(K\,km\,s^{-1}\,pc^2)^{-1}$. Although this is close to the value quoted in Gao & Solomon (2004b), the standard deviation is $3.79\ \rm M_\odot\,(K\,km\,s^{-1}\,pc^2)^{-1}$ which is over half the mean value of $\alpha_{\rm HCN}^{\rm A_V}$.

We can demonstrate the effect of adopting an incorrect $\alpha_{\rm HCN}^{\rm A_V}$ by determining the mass we would expect to get above an $\rm A_V$ of 8 mag using Equation 4.6 and comparing to the actual mass in our simulations that lies above an $\rm A_V$ of 8 mag. We show the results of this analysis in Figure 4.9. We see that for a low amount of dense gas – around 10 $\rm M_\odot$, such as one might find in a handful of prestellar cores – the standard $\alpha_{\rm HCN}$ relation overestimates the amount of dense gas present by up to an order of magnitude. However, once the clouds contain $\rm M_{A_V > 8\,mag} > 100 M_\odot$, the standard $\alpha_{\rm HCN}^{\rm A_V}$ actually predicts the amount of dense gas very well. This suggests that provided one is already looking at well-evolved, and active star-forming regions, the true scatter in $\alpha_{\rm HCN}^{\rm A_V}$ will not significantly affect the predicted mass. However, for regions of low star formation (i.e. early in a cloud’s star-forming evolution), one could significantly over-predict the amount of dense gas present.

We can also do the same analysis using our value of $\rm A_{V,char} = 5.05$ mag that we derived above, instead of $\rm A_V$ of 8 mag in Equation 4.6. Here, we get a mean value of $\alpha_{\rm HCN}^{\rm A_V} = 19.46\ \rm M_\odot\,(K\,km\,s^{-1}\,pc^2)^{-1}$. We can use this value of $\alpha_{\rm HCN}^{\rm A_V}$ to repeat the analysis we just performed with $\rm A_V$ of 8 mag for our $\rm A_{V,char}$ of 5.05 mag, which can be seen in Figure 4.9. We see that using an $\rm A_{V,char}$ of 5.05 mag is a much more reliable estimate of mass across all stages of our suite of simulations.

We can now perform a similar analysis for the conversion factor between HCN emission and gas above a threshold volume density, $\alpha_{\rm HCN}^{\rm n_{thr}}$. As described in Gao & Solomon (2004a, see also Barnes et al. 2020), the mass above the threshold density can be given by,

$$\mathrm{M}^{\mathrm{sum}}_{\mathrm{n}>\mathrm{n}_{\mathrm{thr}}} \approx 2.1\frac{\mathrm{n}^{0.5}_{\mathrm{thr}}}{\mathrm{T}_{\mathrm{B}}}\mathrm{L}_{\mathrm{HCN}} \quad , \tag{4.7}$$

where $\mathrm{T_B}$ is the intrinsic HCN line brightness temperatures and $n_{\mathrm{thr}}$ is our density threshold. The factor of $2.1\mathrm{n}^{0.5}_{\mathrm{thr}}/\mathrm{T_B}$ can hence be identified with the volume density based conversion factor, $\alpha^{n_{\mathrm{thr}}}_{\mathrm{HCN}}$.

The intrinsic brightness temperature for Equation 4.7 would simply be the peak main beam temperature of the spectra, provided that we are dealing with extended sources (i.e. the source is filling the beam) like Barnes et al. 2020. However, if we take our box to be the beam we clearly have a case where the source is much smaller than the telescope beam. Indeed, we see this in Figure 4.10 where the main beam temperatures are at least an order of magnitude lower than those seen in Barnes et al. 2020. In this case we would have to take into account the solid angle of the source convolved with the diameter (FWHM) of the telescope Gaussian beam $\theta_{\mathrm{MB}}$ (see section 4.2 in Gao & Solomon 2004a). Since all the observational studies have a different set-up, we instead use our pixel size as the main beam size and therefore our intrinsic brightness temperature is simply our pixel brightness temperature.

From our simulations, we find $\mathrm{T_B}$ to vary between 6 and 14 K, with a mean of roughly 13 K. We now consider two values for $n_{\mathrm{thr}}$: first, we input the density that is most commonly adopted in the literature (Gao & Solomon, 2004a) of $3\times10^4$ cm$^{-3}$; and second we input our characteristic density of $2.85\times10^3$ cm$^{-3}$ that we established from our simulations in Section 4.3.1. This yields a conversion factor of $\alpha^{n_{\mathrm{thr}}}_{\mathrm{HCN}} = 8.62\ \mathrm{M}_\odot\,(\mathrm{K\,km\,s^{-1}\,pc^2})^{-1}$ for $n > 2.85\times10^3$ cm$^{-3}$ and $\alpha^{n_{\mathrm{thr}}}_{\mathrm{HCN}} = 27.98\ \mathrm{M}_\odot\,(\mathrm{K\,km\,s^{-1}\,pc^2})^{-1}$ for $n > 3\times10^4$ cm$^{-3}$.

We see from Figure 4.11 that our lower calculated density of $2.85\times10^3$ cm$^{-3}$ is able to reproduce the actual mass far better than $3\times10^4$ cm$^{-3}$. In contrast, the standard value of $n_{\mathrm{thr}} = 3\times10^4$ cm$^{-3}$ consistently over-predicts the amount of mass above this density in our simulations by at least an order of magnitude; in one extreme case it predicts 59.9 $\mathrm{M}_\odot$ above $3\times10^4$ cm$^{-3}$ even though *the simulation contained no mass above this density.*

### 4.3.3 THE EFFECT OF OPTICAL DEPTH ON THE HCN EMISSION

We can take advantage of the fact that RADMC-3D can produce optical depth maps of our simulations to explore the effect that the optical depth has on the emission of HCN. Selecting this option in RADMC-3D generates a PPV cube of optical depths (we will use $\tau_{\mathrm{HCN}}$ for the remainder of the section) instead of emission. We can then use these $\tau_{\mathrm{HCN}}$ PPV cubes to find out if the use of $\mathrm{n_H}6\times10^4/\tau$ cm$^{-3}$ by the likes

**Table 4.3.** A table of the percentage of cumulative fraction of emission emanating from $\tau_{\rm HCN} > 1$ from Figure 4.13.

| ID | Percentage [%] |
|---|---|
| C | 34.5 |
| F | 40.2 |
| I | 40.9 |
| L | 33.2 |

of Gao & Solomon 2004a and Krumholz & Tan 2007 is justifiable since we can use our $\tau_{\rm HCN}$ to predict an effective density and compare it to our effective density from Table 4.2. Note that we restrict our analysis to the $\rm t_{SF}$ + 2 Myr snapshots as this is where we find the most dense gas (e.g. Fig 3.4).

We can create maps of the mean optical depth along a line of sight by defining,

$$\langle\tau_{\rm HCN}\rangle = \frac{\sum_{\rm i}\tau_{\rm i}\times {\rm T_i}}{\sum_{\rm i}{\rm T_i}} \quad , \tag{4.8}$$

where i denotes the index of the PPV cube along the velocity axis. The maps of mean optical depth for all four initial velocities are shown in Figure 4.12.

We see from Figure 4.12 that $\langle\tau_{\rm HCN}\rangle$ is high, above 10, towards the bright regions of HCN emission that we see in Figure 5.1, which are associated with column densities in excess of $10^{22}{\rm cm}^{-2}$ (see Figure 3.3). However $\langle\tau_{\rm HCN}\rangle$ is substantially lower than this for most of the map. To get a better idea of the optical depths associated with the bulk of the emission, we show in Figure 4.13 the fraction of emission of HCN as a function of $\tau_{\rm HCN}$. We see that the the peak fraction of emission occurs at around $\tau_{\rm HCN} = 1$ for all 4 simulations. However, from the cumulative distributions, we see that only between 33 % and 41 % of the emission emanates from $\tau_{\rm HCN} > 1$, as summarised in Table 4.3.

To give some indication of the variations of the optical depth with velocity (and thus along the line of sight), we also select a small region of $10 \times 10$ pixels within these simulations to compare the mean line spectra to the mean $\tau_{\rm HCN}$ line. These regions are focused on bright spots in the integrated HCN intensity, and are labelled alphabetically in Figure 4.12. In contrast to the low optical depth seen for the bulk of the cloud, the majority of the emission in these $10 \times 10$ pixel regions stems from $\tau_{\rm HCN} > 1$; indeed, we find some 83 - 95 percent of the emission is associated with $\tau_{\rm HCN} > 1$.

Our analysis shows that while the effective critical density of the HCN might be lowered towards bright, dense (and possibly pre-star-forming) cores, this is not the case for the bulk of the emission in a molecular cloud such as those we study here. We conclude that the low effective density for HCN in our study is the result of sub-thermal excitation from a large amount of low-density material, rather than a lowering of the critical density, such as suggested by Barnes et al. (2020) and Gao & Solomon (2004a).

## 4.4 THE RELATIONSHIP BETWEEN HCN/CO AND DENSE GAS.

As well as using the brightness of the HCN (1-0) line, we can also use the ratio of the HCN (1-0) and CO (1-0) lines to constrain the distribution of gas volume densities in molecular clouds (e.g., Gao & Solomon 2004b, García-Burillo et al. 2012, Leroy et al. 2017, Gallagher et al. 2018). Because each line traces densities above their effective densities (for a clear definition of effective densities, see Shirley 2015), $n_{\rm eff}$, a change in the ratio of intensities between two lines with different $n_{\rm eff}$ can gauge changes in the estimated dense gas mass fraction (see, for example, Krumholz & Thompson 2007 and Leroy et al. 2017). This multiple line method improves the accuracy with which variations in the sub-beam density distribution are recovered, and so is well-suited for low resolution studies i.e. galactic-scale studies which use high effective critical density lines that tend not to fill the beam.

Due to the high effective critical density of HCN, galactic scale studies have begun using HCN (1-0) to CO (1-0) integrated intensity ratio to estimate the distribution of gas volume density (e.g., Leroy et al. 2017, Gallagher et al. 2018, Querejeta et al. 2019). We therefore investigate how the HCN (1-0) / CO (1-0) integrated intensity ratio varies as a function of CO (2-1) line emission which is used as a proxy for surface density. We use the same RT code, RADMC-3D, that we use for our HCN analysis. For both CO (1-0) and (2-1) lines we use ortho- and para- $H_2$ as collisional partners along with the collisional rates provided by Leiden Atomic and Molecular Database (Schöier et al., 2005; Jankowski & Szalewicz, 2005; Yang et al., 2010). When calculating the level populations of the CO, we assume that the gas has an $H_2$ ortho-to-para ratio of 3:1.

For this section we create twelve PPV cubes for all three lines (HCN (1-0), CO (1-0) and CO (2-1)) and for all twelve cases characterised by Table 4.1. We create three additional resolutions for our analysis by degrading all twelve PPV cubes to 0.2, 1 and 10 pc respectively. The resulting variation in the resolution can be seen in Figure 4.4. A cut-off of 0.001 $\mathrm{K\,km\,s^{-1}}$ is placed on the velocity-integrated intensity

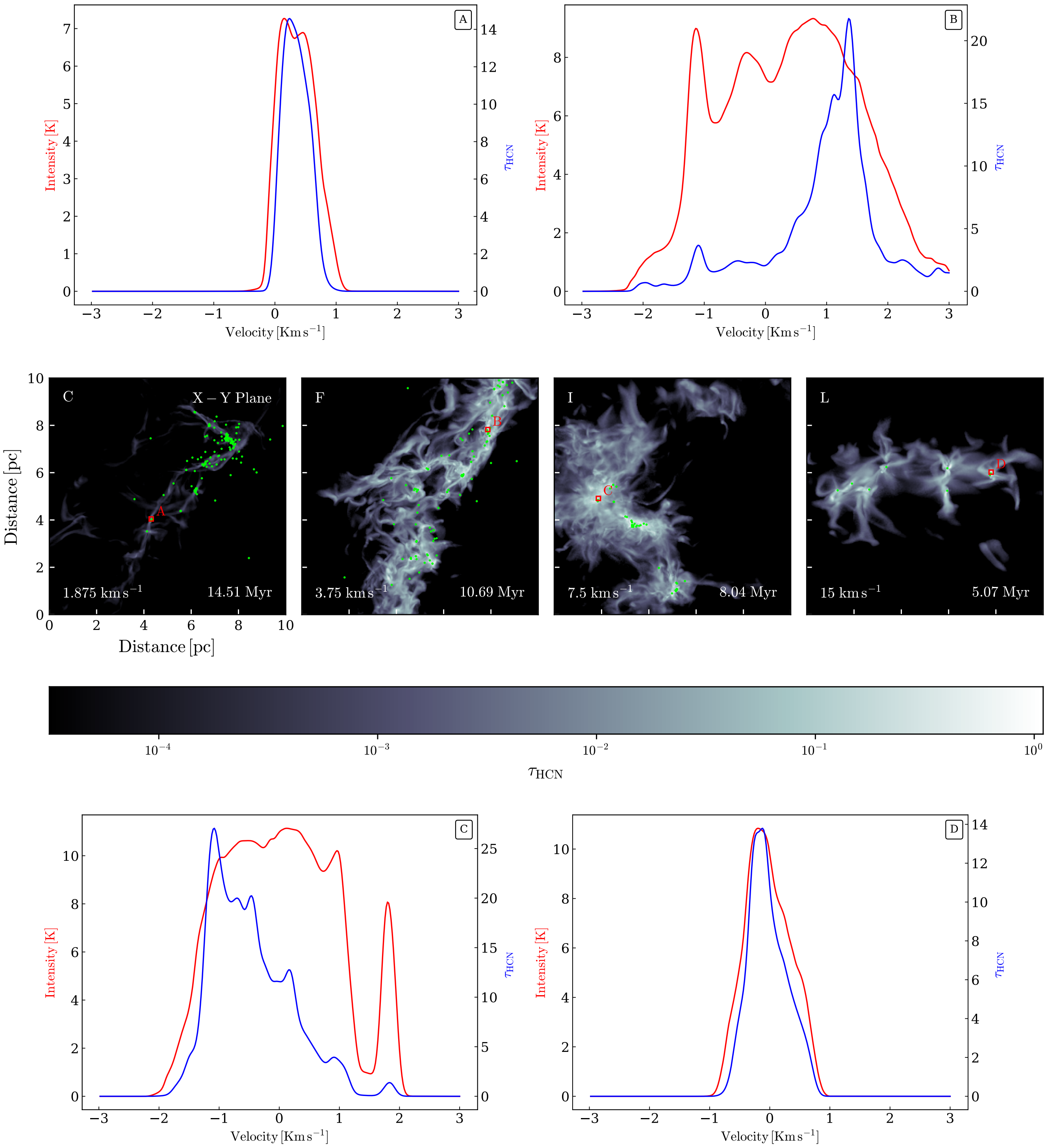

**Figure 4.12.** Emission-weighted integrated optical depth maps of the four initial velocities, all at the later simulation time surrounded by four line spectra and optical depths of selected regions labelled alphabetically (in red) on the optical depth maps. These regions are chosen with the peak optical depth as the centre of a square region with a size of 10 pixels, taking the mean emission and the mean optical depth of these square regions and repeating through each velocity channel to produce the resulting four line profile plots.

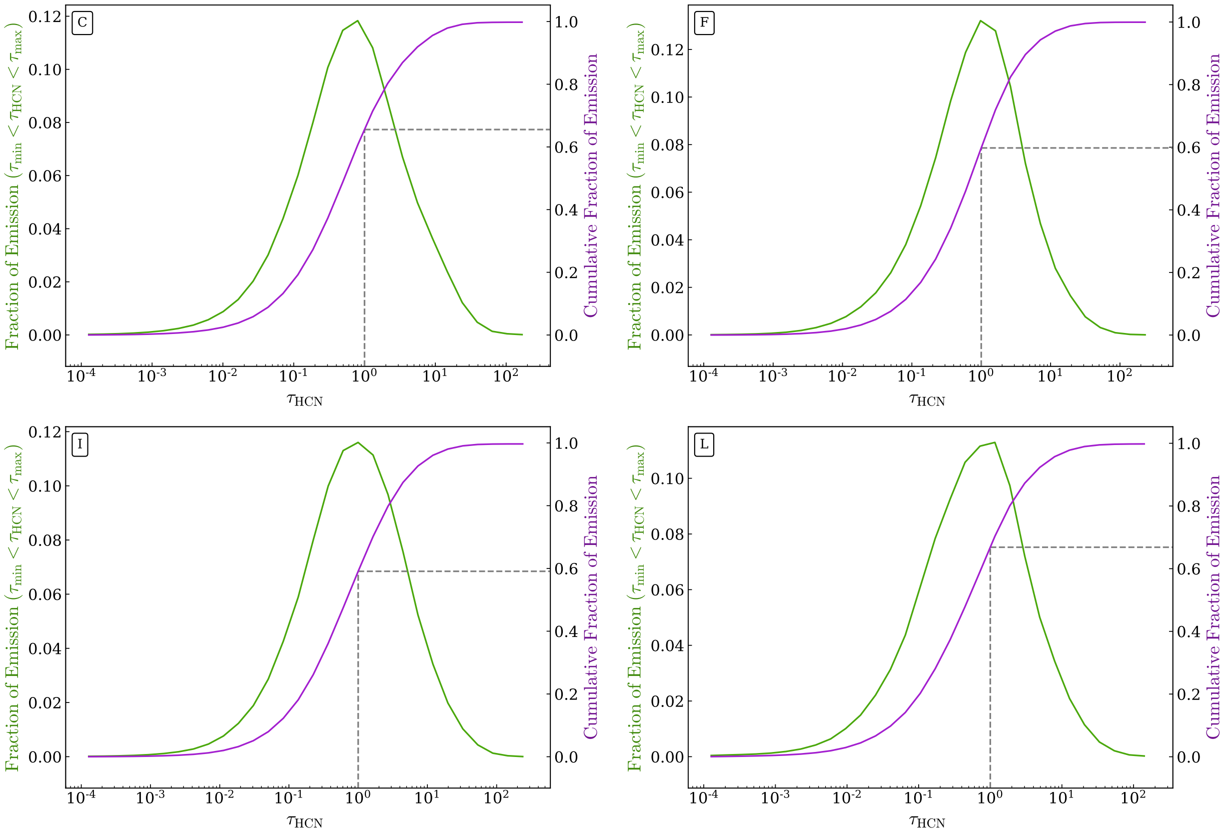

**Figure 4.13.** The fraction of HCN emission as function of optical depth (with accompanying cumulative fraction) for the four later stage simulations. The simulation IDs corresponds to those used in Table 4.1.

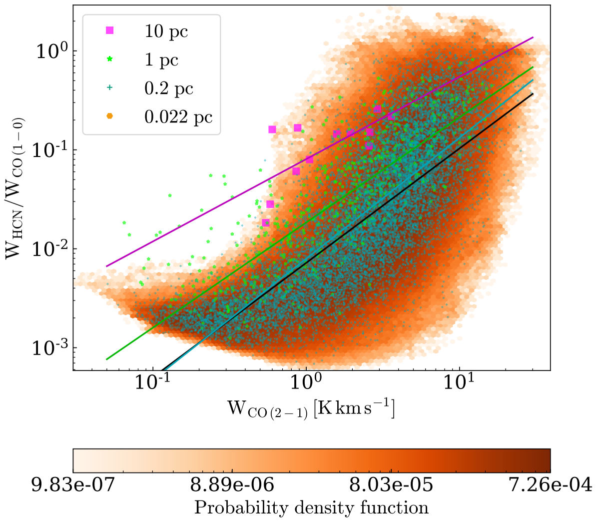

**Figure 4.14.** A plot of HCN/CO integrated intensity ratio against the velocity-integrated intensity of CO (2-1) at four different resolutions of 0.022, 0.2, 1 and 10 pc. Note that a cut-off of 0.001 K km s$^{-1}$ is placed to simulate an observational cut-off due to noise.

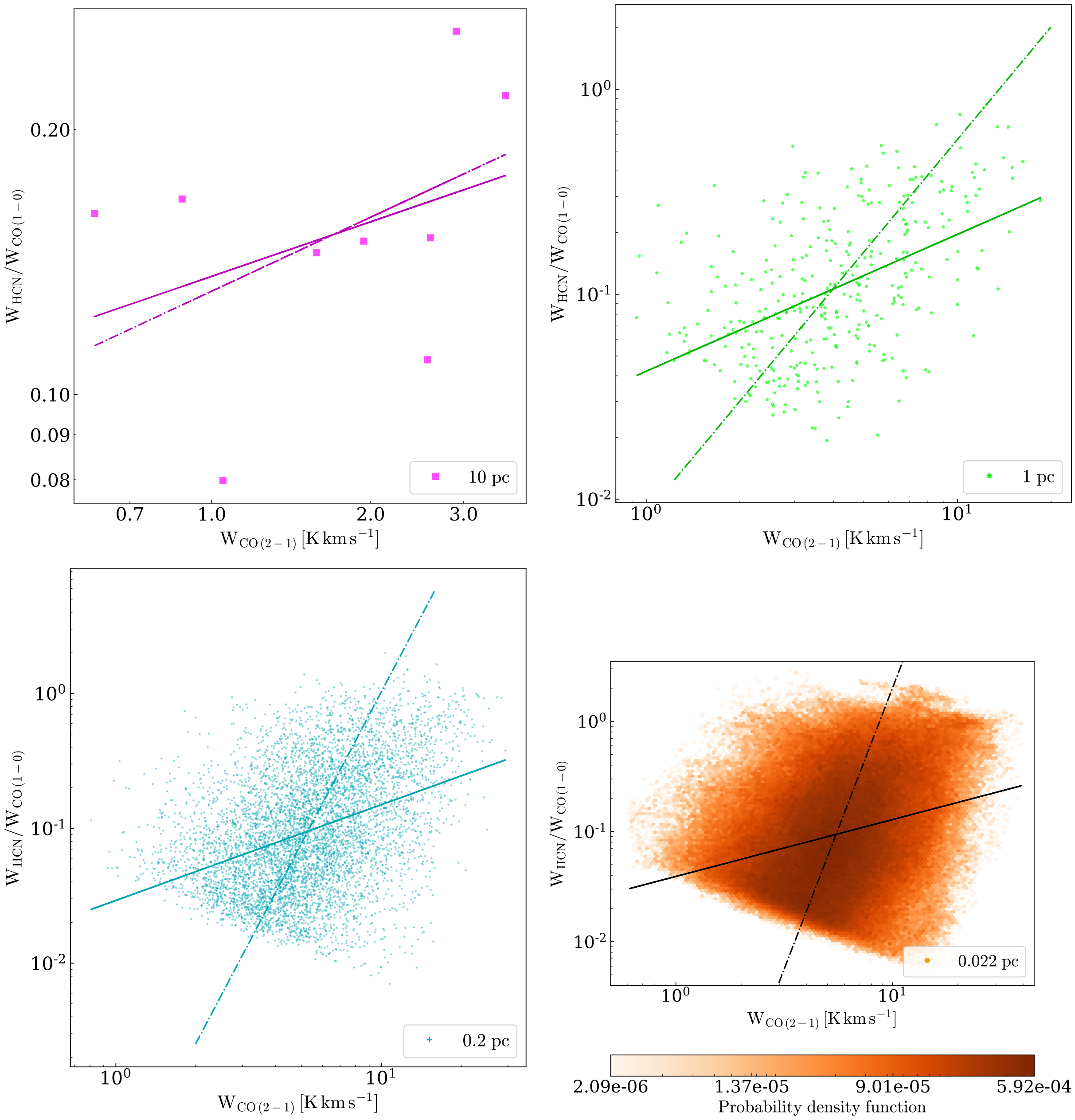

**Figure 4.15.** As Figure 4.14, but with a higher cut-off of 0.1 K km s$^{-1}$. The dotted-dashed line denotes the gradient obtained through total least squares fitting and the solid line denotes the gradient obtained through ordinary least squares fitting.

**Table 4.4.** Summary of our results of comparison between HCN/CO (1-0) to $W_{\mathrm{CO}\,(2-1)}$ for the 0.001 $\mathrm{K\,km\,s^{-1}}$. Note that these gradients are obtained through ordinary least squares (OLS) fitting.

| Resolution [pc] | Gradient of fit OLS |
|---|---|
| 0.022 | 1.16 |
| 0.2 | 1.22 |
| 1 | 1.06 |
| 10 | 0.83 |

**Table 4.5.** Summary of our results of comparison between HCN/CO (1-0) to $W_{\mathrm{CO}\,(2-1)}$ for the 0.1 $\mathrm{K\,km\,s^{-1}}$. Note that these gradients are obtained through ordinary least squares (OLS) and total least squares (TLS) fitting.

| Resolution | Gradient of fit | |
|---|---|---|
| [pc] | OLS | TLS |
| 0.022 | 0.52 | 5.1 |
| 0.2 | 0.71 | 3.7 |
| 1 | 0.67 | 1.83 |
| 10 | 0.21 | 0.28 |

of all three lines to limit our analysis to lines of sight where the abundances are more certain.

We present our HCN/CO integrated intensity ratio against $W_{\mathrm{CO}\,(2-1)}$ in Figure 4.14, which despite the scatter, shows a clear correlation between $W_{\mathrm{HCN}}/W_{\mathrm{CO}}$ and $W_{\mathrm{CO}\,(2-1)}$. We see that the relation between these observables becomes progressively more linear as the resolution decreases. To compare with Gallagher et al. (2018), we present here a the results from a linear regression fit to the data in Figure 4.14, assuming a power-law relationship between $W_{\mathrm{HCN}}/W_{\mathrm{CO}}$ and $W_{\mathrm{CO}\,(2-1)}$; the gradient of fit for all four resolutions is given in Table 4.4. We see that as the resolution decreases (i.e. the pixel area increases) the gradient of fit also decreases (see Table 4.4). Although the trend is consistent with the Gallagher et al. (2018) study, who find a similar relationship between these quantities with a gradient of between 0.55 to 0.81 for resolutions in the range 650 - 2770 pc, the fact that the slope changes so much with resolution for the same underlying data, implies there is no real physical justification for a linear relationship between these variables. At very high resolution, that is, when the beam (each pixel) is fully filled with emission, we find a much steeper relationship than that seen in the unresolved, galactic-scale observations. Once again, this suggests that one needs to be extremely careful when interpreting data of this sort from galactic-scale surveys.

Our cut-off point of 0.001 $\mathrm{K\,km\,s^{-1}}$ in the emission used to generate Figure 4.14 is significantly lower than the $\sim 0.1$ $\mathrm{K\,km\,s^{-1}}$ noise limit of observational surveys. We therefore repeat the analysis above but with a higher velocity-integrated intensity cut-off of 0.1 $\mathrm{K\,km\,s^{-1}}$ on all three lines. For clarity, we plot the four different resolutions on four separate plots (see Figure 4.15). With the higher cut-off, we lose the tail at low $\mathrm{W_{CO\,(2-1)}}$ that clearly has a very shallow gradient. We therefore would reasonably expect a steeper gradient for the higher cut-off analysis. However, using an ordinary least squares (OLS) fitting method we get much shallower gradients than our lower cut-off of 0.001 $\mathrm{K\,km\,s^{-1}}$ (see Table 4.5), since it is sensitive to the outliers from the main trend (the main ridge that you can see by eye). One could also argue that, observationally, there should be errors in both variables, and so OLS is not a statistically valid method for exploring a relation in this data. We therefore compare the OLS to a total least squares (TLS) fitting method that minimizes the orthogonal difference of both the dependent and independent variables to the predicted best fit model. Using TLS to fit our data, we recover a best fit gradient that follows a high density ridge in the scatter. We now see much steeper gradients than what we saw for both OLS fitting of the cut-off of 0.001 $\mathrm{K\,km\,s^{-1}}$ and also 0.1 $\mathrm{K\,km\,s^{-1}}$. We conclude here that the correlation in HCN/CO integrated intensity ratio against $\mathrm{W_{CO\,(2-1)}}$ in previous studies might be in fact due to the resolution and not necessarily due to a physical correlation. Indeed, our RT results would suggest that the underlying correlation between $\mathrm{W_{HCN}/W_{CO}}$ and $\mathrm{W_{CO\,(2-1)}}$ is significantly more complex.

## 4.5 Discussion

Although our work, and those of recent observational and numerical studies (Kauffmann et al. 2017, Pety et al. 2017, Onus et al. 2018, Barnes et al. 2020 and Evans et al. 2020), suggests that HCN primarily traces lower density gas then previously assumed (Gao & Solomon, 2004a; Krumholz & Tan, 2007), there is an undeniable correlation between HCN emission and star formation (Gao & Solomon, 2004a,b). More importantly, the correlation appears to be more linear than that between CO emission and star formation (e.g. Gao & Solomon 2004b). Hacar et al. (2020) has suggested that this correlation between HCN emission and star formation is due to the temperature dependence of the HCN to HNC abundance ratio, and that the ratio increases with temperature. In regions of star formation, where the interstellar radiation field is higher, we expect the gas to be hotter at the lower densities within the cloud (e.g. see Clark et al. 2019). The combination of higher HCN abundance and higher temperature is then proposed to boost the emission.

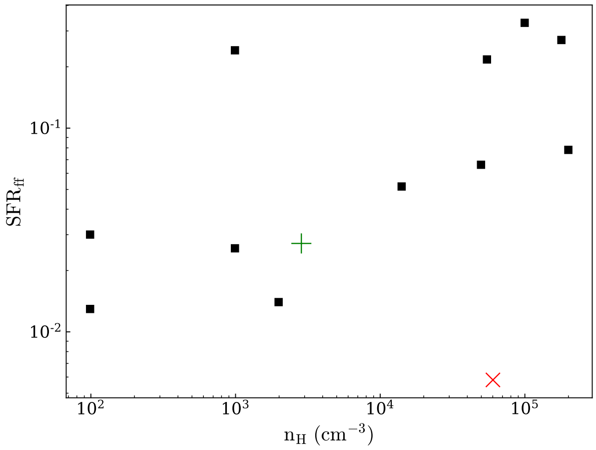

**Figure 4.16.** A reproduction of Figure 5 of Krumholz & Tan (2007), where we highlight their value of the characteristic density and SFR$_{\mathrm{ff}}$ of HCN as a red cross and our value of the characteristic density and SFR$_{\mathrm{ff}}$ as a green plus.

Although we do not include an explicitly temperature-dependent abundance in this section, we can predict what the qualitative effect on our results would be. If our clouds were exposed to a higher degree of ambient star formation, the gas at low densities would be hotter, and the HCN abundance would then be higher than what we currently adopt in these regions (Hacar et al., 2020). This would boost the emission from the lower density gas. The effect on our results would be, if anything, to lower the characteristic density traced by HCN emission, and thus this does not alter our main conclusion. However, whether this combination of effects leads to a linear relation between HCN emission and star formation remains to be tested, and we aim to revisit it in a future study.

Our use of the Fuente et al. (2019) results to derive our HCN to CO abundance ratio also differs slightly from those of Tafalla et al. (2021). Fuente et al. (2019) only observed a particular region of TMC-1 whilst Tafalla et al. (2021) observed the entire cloud. However, using Fuente et al. (2019) gives us a very conservative estimate for the HCN abundance at lower densities (below an $A_V$ of 20 mag) compared to Tafalla et al. (2021). Once again, we can predict that using the Tafalla et al. (2021) abundance ration would almost certainly lower the density threshold ($n_{\mathrm{char}}$) as the higher HCN abundances at lower densities / $A_V$ would provide a greater contribution of HCN emission to our Figure 4.5 at lower densities.

The findings in this section, and those from the observational studies of Pety et al. (2017), Kauffmann et al. (2017), Barnes et al. (2020) and Tafalla et al. (2021), have serious implications for the use of HCN as a tracer of dense gas. This lower density threshold for HCN emission also has implications for the study of the star formation efficiency per free-fall time in GMCs. For example, Krumholz & Tan (2007) argue that star formation in dense gas is "slow", in the sense that only a small percentage of the gas forms stars every free-fall time. However, they assume that HCN emission traces gas with densities $\sim 6 \times 10^4\,\mathrm{cm}^{-3}$, which therefore has a short free-fall time. If the true value for the density traced by HCN is closer to the value of $\sim 3 \times 10^3\,\mathrm{cm}^{-3}$ that we find, this implies that the actual free-fall time is a factor of 4–5 longer than the value they derive, with a corresponding increase in the inferred star formation efficiency per free-fall time. Further, as we demonstrate at the end of Section 4.3.2, the commonly-used methods for converting HCN emission into dense gas can over-predict the amount of gas residing at densities of $\mathrm{n_{char}}$ and higher be orders of magnitude, especially at early times when there is little star formation. This would again artificially lower the apparent star formation rate per free-fall time.

## 4.6 CONCLUSIONS

We investigate the relationship between gas density and HCN emission through post-processing of high resolution magnetohydrodynamical simulations of cloud-cloud collisions using RADMC-3D and AREPO. We carry out 4 simulations with increasing cloud velocities from 1.875 $\mathrm{kms^{-1}}$ to 15 $\mathrm{kms^{-1}}$ and study the HCN emission from the clouds at 3 different times in each simulation, allowing us to explore a wide range of potential molecular cloud environments.

In our study, we find that HCN (1-0) emission traces gas with a characteristic volumetric density of $\sim 3 \times 10^3$ $\mathrm{cm^{-3}}$ and a characteristic visual extinction of $\sim 5$ mag. Our findings are broadly consistent with those from recent observational studies Pety et al. (2017), Kauffmann et al. (2017) and Barnes et al. (2020), and taken together, implies that HCN emission traces more diffuse gas than previously thought (e.g. Gao & Solomon 2004a).

We also find a luminosity to mass conversion factor of $\alpha_{\mathrm{HCN}}^{\mathrm{A_V}} = 6.79\ \mathrm{M_\odot}\,(\mathrm{K\,km\,s^{-1}\,pc^2})^{-1}$ for $\mathrm{A_V} > 8$ mag and $\alpha_{\mathrm{HCN}}^{\mathrm{n_{thr}}} = 8.62\ \mathrm{M_\odot}\,(\mathrm{K\,km\,s^{-1}\,pc^2})^{-1}$ for $\mathrm{n} > 2.85 \times 10^3\ \mathrm{cm^{-3}}$. When we adopt the "standard" conversion factor with characteristic density $\mathrm{n} > 3 \times 10^4\ \mathrm{cm^{-3}}$, we find that the analysis over-predicts the amount of "dense" gas by at least an order of magnitude. Indeed, in some cases, the conversion factor predicts gas in the the density range $\mathrm{n} > 3 \times 10^4\ \mathrm{cm^{-3}}$ when no gas above that density exists in our simulations.

# CHAPTER 5

# DOES THE ISRF HAVE AN IMPACT ON THE EFFECTIVE DENSITY OF HCN?

## 5.1 INTRODUCTION

The relationship between star formation and the ISRF is somewhat linear since the more stars that are formed, the more the contribution of radiation from these stars have on the ISRF. There is an assumption here that the initial mass function (IMF) of a star forming region is invariant to the ISRF and that a higher star formation in a produces more O and B type stars that are the primary source of UV and cosmic rays in the ISRF (Clark & Glover, 2015). With the typical age of O and B type stars being roughly 2 million years and most of these stars likely to go supernova, this creates a frequent large source of UV rays and most of the cosmic rays since it is thought that supernovae are the main source of cosmic rays Blasi (2013).

This is very significant since the far-ultraviolet (FUV) region of the interstellar radiation field is also the dominant driving force of chemistry in the ISM, since FUV photons actively participate to the photoionization and photodissociation process (Levrier et al., 2012; Bron et al., 2014). Cosmic rays also provide a source of influence on the chemistry of the ISM since they penetrate deep into dense molecular clouds and provide a small degree of ionization upon collision with gas-phase species, mainly, molecular hydrogen and helium Herbst et al. (2000). This therefore implies a relationship between the chemistry in the ISM and both star formation rate and ISRF strength as shown in Clark et al. (2019).

As we have seen in Section 4 the ISRF strength was assumed to be constant with a $G_0$ of 1.7 Habing units. However, this is calculated based on the local ultraviolet background. It is therefore reasonable to assume that the value of $G_0$ in galaxies can vary wildly. Indeed even in our own Milky Way we see that in Porter & Strong

(2005) the radiation field strength varies over ∼2 orders of magnitude.

As mentioned earlier this variation in the ISRF (and therefore the value in $G_0$) is significant to the chemistry of these environments because of the photoionization and photodissociation processess. We have shown previously that there is a relationship between HCN abundance and CO abundance (Fuente et al., 2019). Fuente et al. (2019) also show that this relationship is quite robust and that our interest is therefore whether or not the CO abundance is robust to the ISRF. So in summary, the main component of the effect of the ISRF strength on the effective density of the HCN emission is the relationship between the UV field and CO.

This therefore begs the question, should we have used Barnes et al to compare with our section 4 work, since they had a much more active star forming region. This would give a higher ISRF strength and therefore potentially a different radial profile of CO abundance, which leads to a different HCN abundance profile and would result in a potentially different effective density of the HCN emission.

Hacar et al. (2020) also found an order of magnitude lower energy barrier for the production of HCN through HNC and therefore found that the temperature required for HNC to HCN production went from being unrealistically high to a more achievable low temperature of ∼ 50K. This creates a boost in HCN production in star forming dense cores and therefore contributes to the relationship between HCN formation and star formation.

In this section we expand on our previous sections work by examining how the HCN emission in our cloud-cloud collision simulations vary with varying levels of $G_0$ and CRIR. Specifically, we investigate if there is such a relationship between HCN luminosity and star formation and whether or not the ISRF has an affect on the effective density of HCN emission.

## 5.2 Numerical Method

### 5.2.1 Numerical Model

To model the gas in this study, we use the same modified version Arepo as presented in Chapter 3. To simulate the HCN emission in these simulations, we use the same RADMC-3D radiative transfer (RT) code (Dullemond et al., 2012) as in section 4 to create post-processed position-position-velocity (PPV) cubes.

**Table 5.1.** A brief overview of all 6 cases that were post-processed through RADMC-3D. The time denotes the time at which the simulation has evolved to before being post-processed through RADMC-3D.

| ID | Initial Mass $[\mathrm{M}_\odot]$ | $\mathrm{G}_0$ [Habing] | CRIR $[\times 10^{-17}\mathrm{s}^{-1}]$ | Time [Myr] |
|---|---|---|---|---|
| A | 1e4 | 1.7 | 3 | 8.74 |
| B | 1e5 | 1.7 | 300 | 4.95 |
| C | 1e5 | 1.7 | 3 | 3.9 |
| D | 1e5 | 0.17 | 3 | 2.9 |
| E | 1e5 | 17 | 3 | 4.34 |
| F | 1e5 | 170 | 3 | 4.55 |

### 5.2.2 RADIATIVE TRANSFER POST-PROCESSING

As in Chapter 4 we convert our voronoi mesh into a regular cartesian grid. Due to the fine resolutions that the voronoi mesh can go to, we would struggle to post-process the entire 157.9/244.66 pc box. Instead we choose a 10 pc cubic region that contains some of the highest densities within the box; AREPO's voronoi mesh is interpolated on to a $450^3$ grid such that we have a spatial resolution of 0.022 pc in the RT. We use the same observationally derived $x_{\mathrm{HCN}}/x_{\mathrm{CO}}$ v $\mathrm{A_V}$ relation from Chapter 3 shown in Figure 8 of Fuente et al. (2019) to create our HCN abundances from the CO abundances generated in our AREPO simulations.

## 5.3 RESULTS

We can already see in Figure 5.1 that the relationship between HCN emission and Star formation rate is unlikely to hold true since the $\mathrm{G}_0 = 170$ produces significantly less emission in all regions compared to both $\mathrm{G}_0 = 17$ and $\mathrm{G}_0 = 1.7$. This is reinforced by Figure 5.2 in which we can clearly see that there is no clear relationship between HCN emission and $\mathrm{G}_0$ (and therefore temperature of the ISM). It is clear that Figure 5.2 goes directly against the result that Hacar et al. (2020) finds in which a correlation between the temperature of the ISM and the intensity of HCN is observed and that the HCN/HNC line ratio can be used as a new chemical thermometer for the ISM.

We also replicate Figure 11 from Hacar et al. (2020) by using our column density and our HCN intensity along with the temperature of the gas being represented by our different simulations of varying $\mathrm{G}_0$ (where the "colder" bluer data is represented by our lower $\mathrm{G}_0$ simulation and the "hotter" redder data is represented by our higher $\mathrm{G}_0$ simulation). This can be seen in Figure 5.3 where we include all

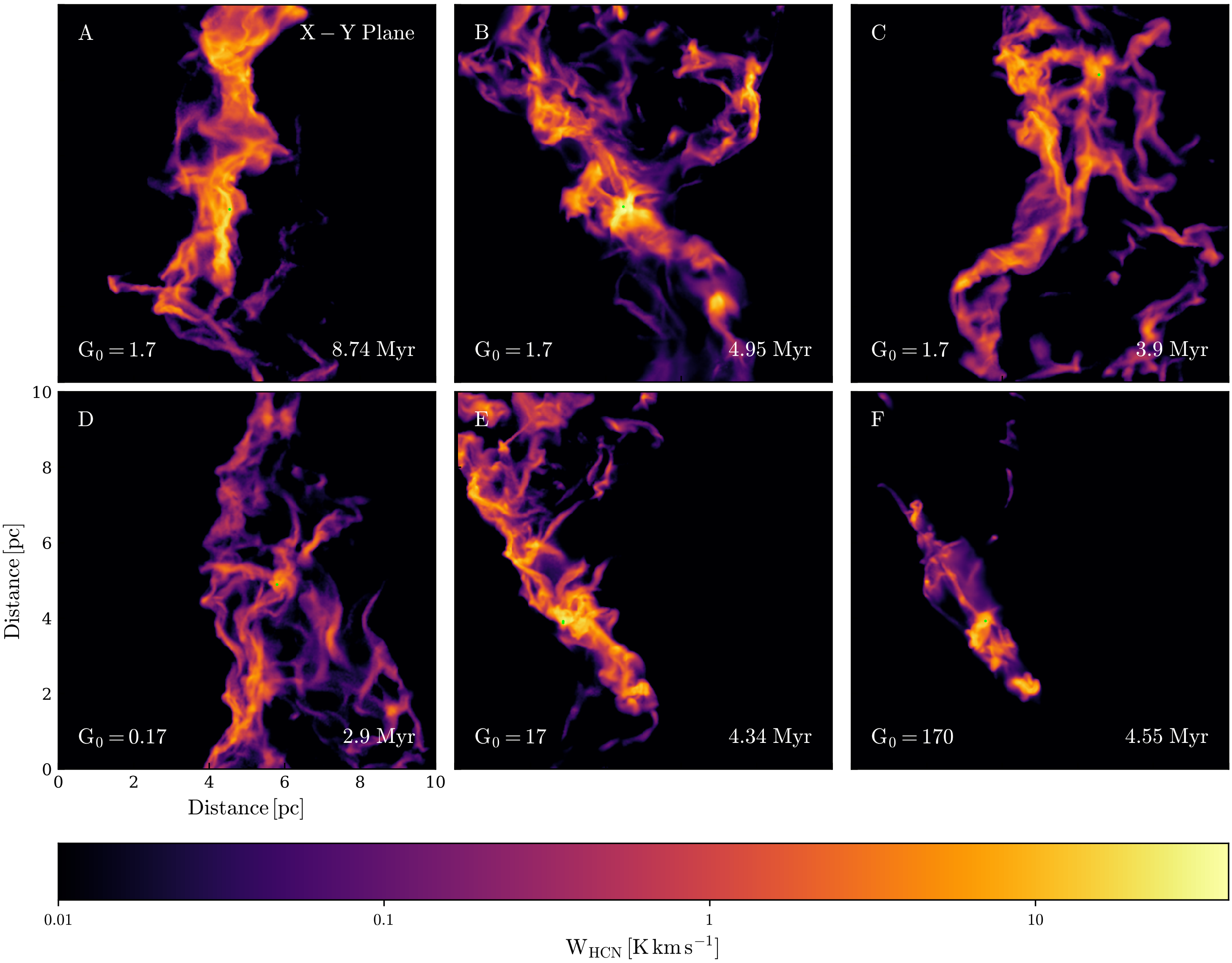

**Figure 5.1.** Maps of the velocity-integrated intensity in the J = 1 → 0 line of HCN, $W_{HCN}$, at the three simulation times and the four initial velocities that were used in Figure 3.3. Note that the alphabetical letters on each tile corresponds to the IDs in Table 5.1

our simulation data, even that which cannot be seen by observers. We also include a figure that is more representative of that which can be seen in Figure 11 of Hacar et al. (2020), this can be seen in Figure 5.4.

Whilst we do see some correlation between temperature and HCN intensity at very low intensities in Figure 5.3, we do not see this same trend at the more observable higher intensity scales. We see that for a given column density, the higher $G_0$ simulations have a lower value of $W_{HCN}$. This correlation in Figure 5.4 is almost completely to the contrary to what was seen in Figure 11 in Hacar et al. (2020).

What we are seeing in Figure 5.4 is the lack of HCN due to the photodissociation in the exposed regions is not balanced by the higher gas temperature emission of the HCN in regions that are only somewhat shielded.

Producing gas kinetic temperature - density phase diagram of our lowest $G_0$ and also our highest $G_0$ (seen in Figures 5.5 and 5.6 respectively), we can see that the higher $G_0$ produces a higher value for the gas temperature across all density values. This means that the higher $G_0$ is indeed “hotter” than the lower $G_0$ simulation, and therefore this is indeed opposite to the claim that Hacar et al. (2020) states in that the hot gas is “brighter”.

There is a small caveat in our result however, in that we do not account for the “boost” in HCN that Hacar et al. (2020) calculates due to the revised HCN/HNC line ratio. This means that Hacar et al. (2020) would predict a higher HCN abundance in the high density gas and would see more emission, with the assumption that this in a region of optically thin and beneath the critical density.

Conversely, there is an issue in Hacar et al. (2020) in that their modelling does not have a self-consistent relation between $G_0$ and gas temperature whereas our modelling does. This means that they can have unrealistic temperatures since one of the main driving factor of gas temperature is the $G_0$. In addition, we are able to tie the HCN abundance to our CO abundance explore down to low column densities unlike Hacar et al. (2020) who only explores HCN in high column densities. Finally because our HCN - CO relation is observationally derived, we naturally explore large variations in the local UV and CRIR since even for a cloud sitting in a single UV field, the local UV field will vary because of shielding.

The cumulative fraction of emission that was produced in our previous chapter (Chapter 4) with the same methodology is calculated and shown in Figure 5.7. We can see that as the ISRF increases in the simulations the effective density of HCN increases. What is also clear is that there appears to be an upper limit or a boundary that the effective density reaches with a higher ISRF. This suggest that there is a maximum value that the effective density of HCN can reach (at roughly $10^4\,\mathrm{cm}^{-3}$)

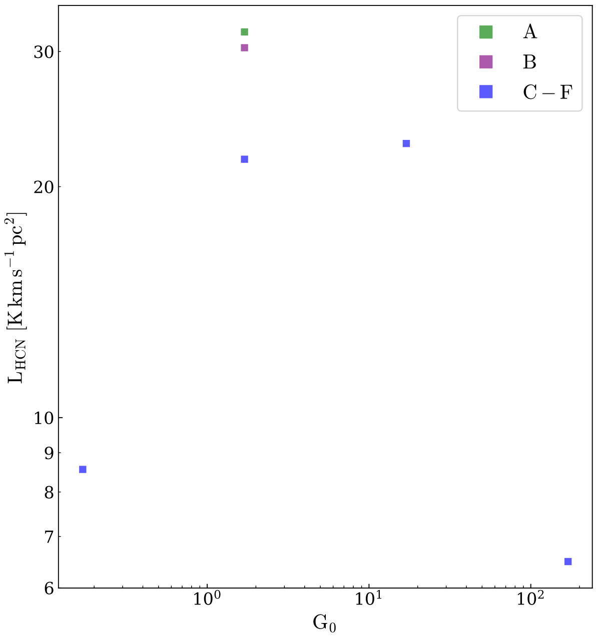

**Figure 5.2.** Total integrated luminosity of HCN as a function of interstellar radiation field strength, $G_0$. The legend denotes the IDs corresponding to the simulation found in Table 5.1.

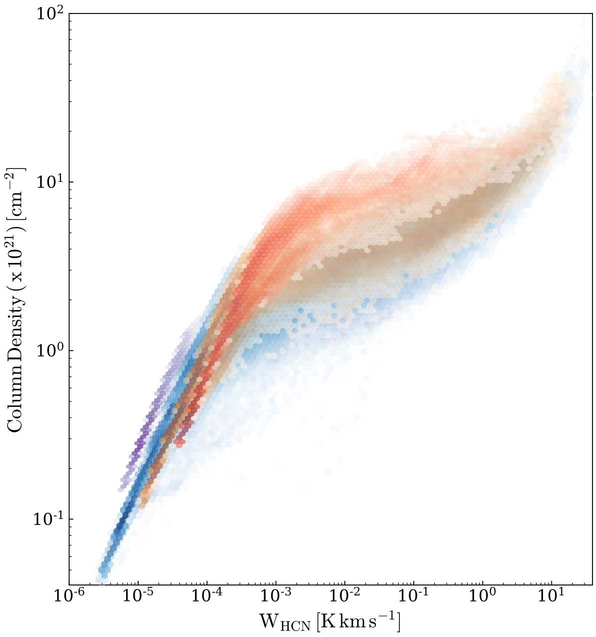

**Figure 5.3.** Correlation between the observed total HCN intensities $W_{HCN}$ and the total gas column density for all simulations. Here the colour denotes the different "gas kinetic temperatures" represented by the value of $G_0$ for each simulation. Purple is a value of $G_0 = 0.17$, blue is a value of $G_0 = 1.7$, orange is a value of $G_0 = 17$ and red is a value of $G_0 = 170$.

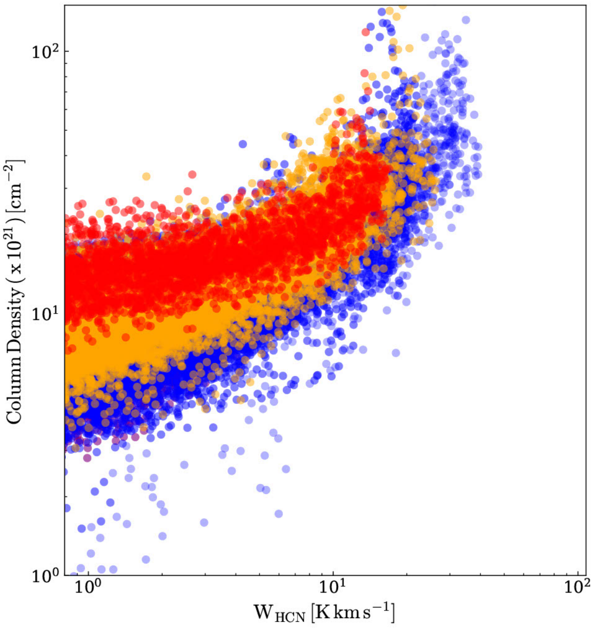

**Figure 5.4.** A zoomed in segment of Figure 5.3, where the limits are similar to that of Figure 11 in Hacar et al. (2020). This figure share the same colour format as Figure 5.3.

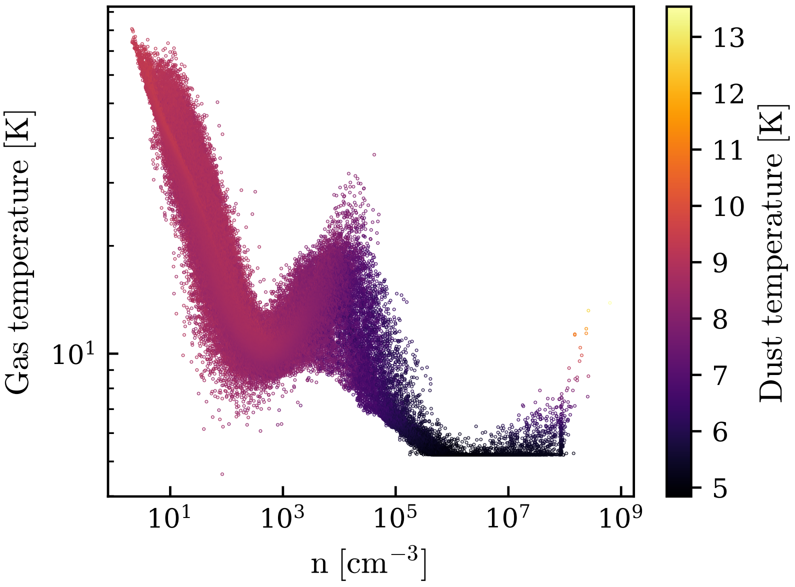

**Figure 5.5.** A phase diagram of the gas temperature versus density coloured by the dust temperature for the $G_0 = 0.17$ simulation (labelled D in Table 5.1).

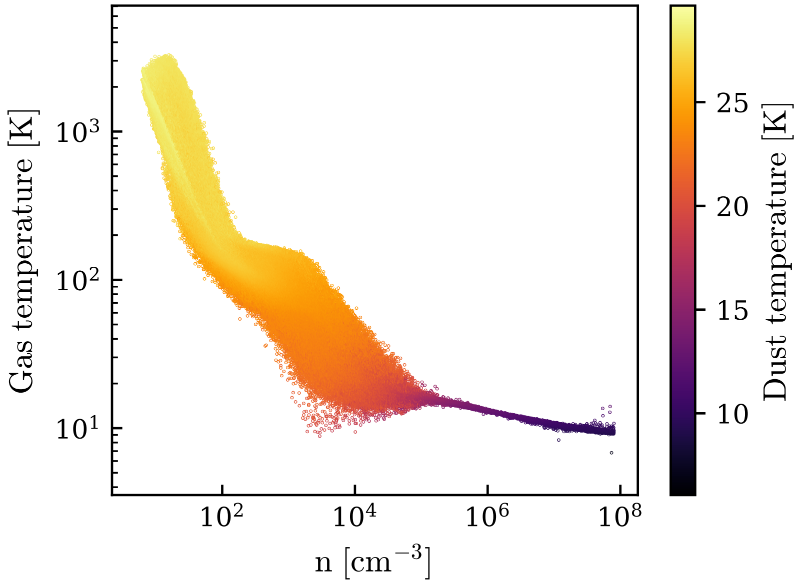

**Figure 5.6.** A phase diagram of the gas temperature versus density coloured by the dust temperature for the $G_0 = 170$ simulation (labelled F in Table 5.1).

and therefore the effective density of HCN of $6 \times 10^4\,\mathrm{cm}^{-3}$ stated by Krumholz & Tan (2007) is unrealistic and that if we were to use something a little more realistic such as $8 \times 10^3\,\mathrm{cm}^{-3}$ we would see Figure 5 in Krumholz & Tan (2007) become much more aligned to the other tracers, disproving their theory of this evidence of slow star formation in dense gas. We also compare again to Kauffmann et al. (2017) and Barnes et al. (2020) like we did in Chapter 4. We see that our cumulative is much closer to Barnes et al. (2020) this time around, especially comparing our simulation of highest $G_0$. This is particularly comforting since Barnes et al. (2020) were looking into a very hot dense region which our $G_0$ of 170 tries to resemble.

We can now investigate whether or not a large variance in the ISRF effects our study into the $\alpha_{\mathrm{HCN}}$ that we made in Chapter 4. Using the same equations (see Equations 4.6 and 4.5) in Chapter 4, however in this case we now have a different characteristic density, $n_{\mathrm{char}}$, and a different characteristic visual extinction, $A_{V,\mathrm{char}}$, derived from Figures 5.7 and 5.8. We find that the characteristic density of HCN here is an $n_{\mathrm{char}}$ of $4.3 \times 10^3\,\mathrm{cm}^{-3}$ and a characteristic visual extinction, $A_{V,\mathrm{char}}$ of 7 mag.

Looking at how well HCN emission can predict the mass above a given column density, we calculate the predicted mass above a given column density using the same equation 4.6 shown in Section 4.3.2 and compare to the actual mass above a given density, which is presented in Figure 5.9. Delving into the granular detail of the differences between the predicted mass derived using an $A_V$ of 7 mag versus 8 mag, we see that the predicted mass derived using 7 mag can reproduce the actual mass

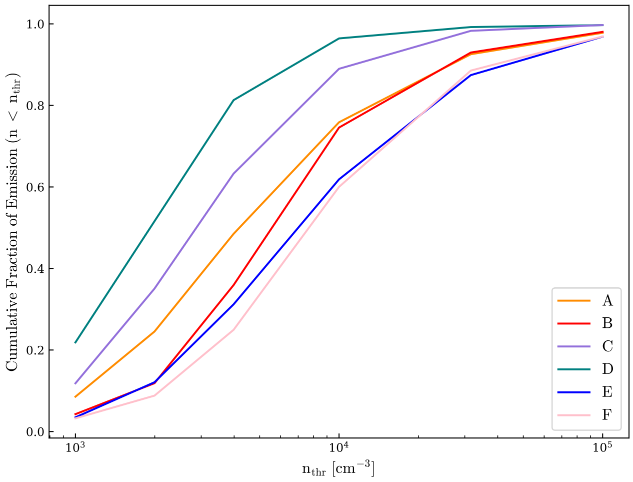

**Figure 5.7.** Cumulative fraction of emission of HCN plotted as a function of density for all simulations with the labelling according to Table 5.1.

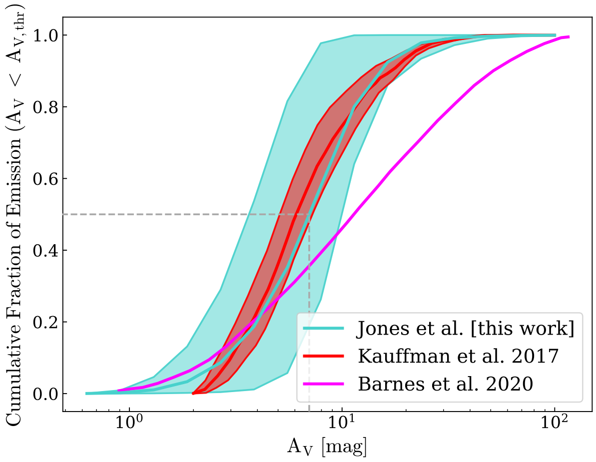

**Figure 5.8.** Cumulative emission of HCN plotted as a function of $A_V$ with the mean, minimum and maximum cumulative emission from all six simulations. We include the cumulative emission of HCN from Kauffmann et al. (2017) and Barnes et al. (2020) for comparison.

incredibly well at the higher mass range compared to 8 mag. However, the predicted mass using 8 mag can reproduce the actual mass incredibly well at the lower mass range compared to 7 mag. But overall we see that there is very little difference between our value of 7 mag and the commonly used value of 8 mag in the result of the predicted mass vs the actual mass in our simulations. Since there is very little difference between the predicted and actual mass for both 7 mag and 8 mag, it is reasonable to assume that both values are acceptable to use as characteristic visual extinction values. An important detail to note here is that this only applies to this study and does not apply to the previous work done in the previous chapter, where the commonly used value used by observers of 8 mag did not reproduce the actual mass well at all compared to our value of 5.05 mag. This could be down to the different variations in the parameters and therefore our value of 7 mag and the commonly used value of 8 mag can only be applied to environments of wide variations of the ISRF strength, i.e. on large galactic scales. Whereas, our value of 5.05 mag can only be used on environments of small variations of ISRF strength and large velocity scales such as small molecular cloud scales.

In order to examine how well the HCN emission can predict a mass above a certain density, we revisit Equation 4.7 from Section 4.3.1. We must recalculate the factor of $2.1\mathrm{n}_{\mathrm{thr}}^{0.5}/\mathrm{T}_{\mathrm{B}}$. The main beam temperature, $\mathrm{T}_B$ was found to be 17 K. We therefore calculate a factor of 19.42 for $\mathrm{n}_{\mathrm{char}}$ of $3 \times 10^4\,\mathrm{cm}^{-3}$ and 7.35 for $\mathrm{n}_{\mathrm{char}}$ of $4.3 \times 10^3\,\mathrm{cm}^{-3}$. The predicted mass calculated above a given density is then compared to the actual mass above the same density found in the simulation and is presented in Figure 5.10.

When we look at Figure 5.10, we see that neither of the values of the characteristic density of the standard value of $3 \times 10^4\,\mathrm{cm}^{-3}$ and our value of $4.3 \times 10^3\,\mathrm{cm}^{-3}$ do a good job of predicting the mass in our simulations. We are under-predicting the actual mass that is in the simulation whereas the commonly used value from Gao & Solomon (2004b) of $3 \times 10^4\,\mathrm{cm}^{-3}$ is over-predicting the actual mass that is in the simulation. It could be argued that we do a modestly good job of predicting the mass in the simulations towards the higher end scale of the mass range.

This over- / under-prediction in the mass in Figure 5.10 could be due to the fact that observers assume that these clouds are roughly isothermal when HCN is bright ($\tau >> 1$), so one can postulate that $\mathrm{T}_{\mathrm{g}} \equiv \mathrm{T}_{\mathrm{ex}}$ and so the 'peak' temperature is a good $\mathrm{n}_{\mathrm{crit}}$ estimate for Equation 4.7. But as clouds have HCN tracing low density, with higher gas temperature but still with $\mathrm{T}_{\mathrm{ex}} < \mathrm{T}_{\mathrm{g}}$ that is also below $\mathrm{n}_{\mathrm{crit}}$, the 'peak' main beam temperature is tracing low density, subthermal emission and not the gas with high density ($\mathrm{n} >> \mathrm{n}_{\mathrm{crit}}$).

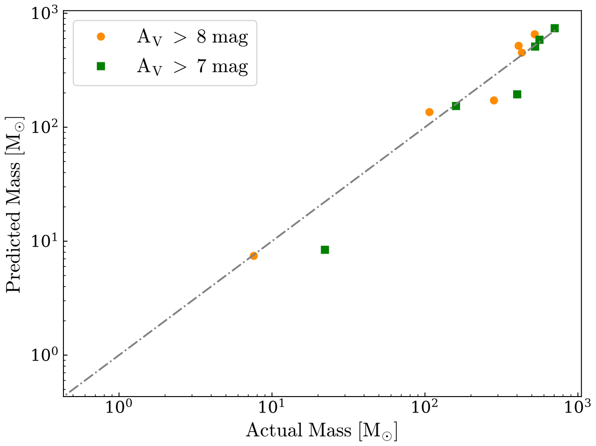

**Figure 5.9.** A plot of predicted mass for all simulations using a re-arranged version of equation 4.6 where $\alpha_{\rm HCN} = 35.55\ {\rm M_\odot}\,({\rm K\,km\,s^{-1}\,pc^2})^{-1}$ for $A_V > 8$ mag compared to the actual mass calculated within regions of $A_V > 8$ mag and $\alpha_{\rm HCN} = 40.20\ {\rm M_\odot}\,({\rm K\,km\,s^{-1}\,pc^2})^{-1}$ for $A_V > 7$ mag compared to the actual mass calculated within regions of $A_V > 7$ mag. The dashed line denotes the point at which the predicted mass is equivalent to the actual mass.

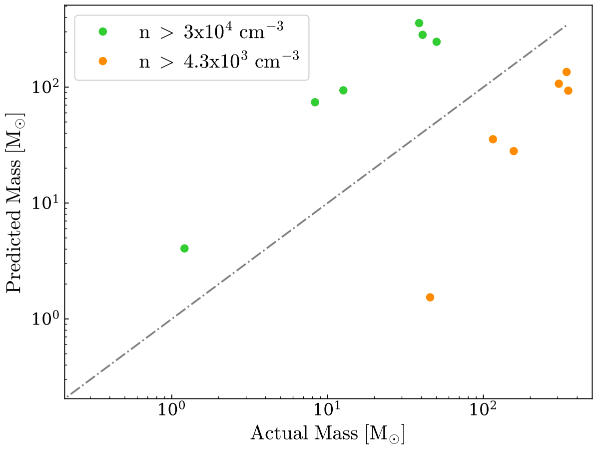

**Figure 5.10.** A plot of predicted mass for all simulations using Equation 4.7 for our density threshold of $4.3 \times 10^3$ cm$^{-3}$ and Gao & Solomon (2004a) density threshold of $3 \times 10^4$ cm$^{-3}$ compared to the actual mass calculated above these two density thresholds. The dashed line denotes the point at which the predicted mass is equivalent to the actual mass.

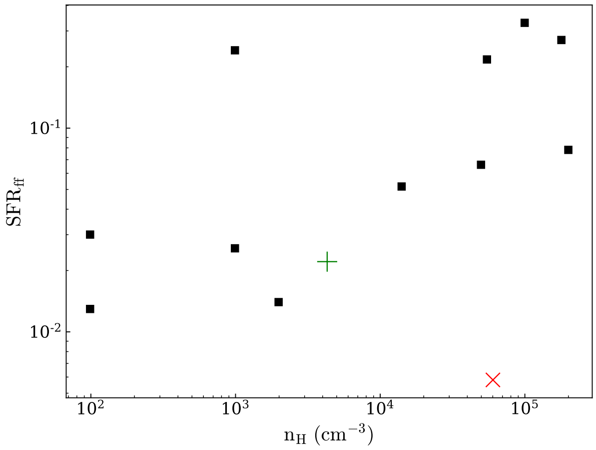

**Figure 5.11.** A reproduction of Figure 5 of Krumholz & Tan (2007), where we highlight their value of the characteristic density and $SFR_{ff}$ of HCN as a red cross and our value of the characteristic density and $SFR_{ff}$ as a green plus. Note that our green plus has shifted ever so slightly lower in $SFR_{ff}$ and higher in the characteristic density compared to Figure 4.16.

## 5.4 Discussion

The results over the last two chapters have shown that the use of HCN in observational studies is more complicated than previously assumed. Both Figures 4.5 and 5.7 show that there are several factors that influence the characteristic density of HCN. It is unclear how sensitive HCN is to these factors, this would have to be researched further with a broader parameter space, however it is clear that using a blanket value such as $3 \times 10^4\,\mathrm{cm}^{-3}$ is impractical and could effect the crucial role that HCN provides to observers. And that is the star formation rate of dense gas regions. If we have a lower characteristic density, we overestimate the amount of dense gas we have within our HCN observations and therefore overestimate the star formation rate.

As we mention in Section 4.5, a change of an order of magnitude in the characteristic density of HCN would change the position of the HCN data on Figure 5 of Krumholz & Tan (2007) entirely, in fact to show this we decide to replicate Figure 5 of Krumholz & Tan (2007) but with our own data also showed to emphasize the difference that using a characteristic density of $6 \times 10^4\,\mathrm{cm}^{-3}$ can have compared to $4.3 \times 10^3\,\mathrm{cm}^{-3}$. We compare their $SFR_{ff}$ value, we use Equation 1 in Krumholz & Tan (2007) along with their assumptions of $f_{HCN} = 1$ and $\dot{M}_\star/M_{HCN} = (30\,\mathrm{Myr})^{-1}$. We can see in Figure 5.11 that our value is much more aligned with the trend set by the other tracers.

## 5.5 CONCLUSIONS

We investigate the significance of varying the Interstellar radiation field strength has on the characteristic density of HCN. We also investigate whether or not HCN can be a tool to be used as a “chemical thermometer for the ISM”. We find that the Total integrated luminosity, $\mathrm{L_{HCN}}$, and $G_0$ of our simulation (that characterises our temperature) does not follow any particular trend and certainly does not show that HCN can be used as a “chemical thermometer for the ISM”.

We also find that the characteristic density of HCN varies of order of a half a magnitude and that the mean characteristic density of HCN, $\mathrm{n_{char}}$, is $4.3 \times 10^3\,\mathrm{cm^{-3}}$ and the characteristic visual extinction, $\mathrm{A_{V,char}}$ is 7 mag. An interesting observation was that we find that there appears to be an upper limit/boundary that the characteristic density of HCN can have as the simulations' $G_0$ is increased. It appears that for this environment that we created it is very unlikely that $\mathrm{n_{char}}$ would surpass $10^4\,\mathrm{cm^{-3}}$ no matter how high the $G_0$ is. However, this is not necessarily a universal statement as it is unclear if this observation applies to clouds of different masses.

# CHAPTER 6

# CONCLUSIONS AND FUTURE WORK

In this chapter, I summarise the main conclusions of this work, the caveats that were present in our work and present the future work that would follow from the work conducted in this thesis.

## 6.1 CONCLUSIONS

The goal of this thesis was to investigate the role of HCN emission in star formation studies both observationally and theoretically. HCN emission is commonly used in observational studies as a gas tracer that traces densities above $10^4$ cm$^{-3}$ (Gao & Solomon, 2004a,b; Krumholz & Thompson, 2007; Krumholz & Tan, 2007; García-Burillo et al., 2012; Jiménez-Donaire et al., 2017; Onus et al., 2018; Fuente et al., 2019). However, there are studies that suggest that HCN emission traces gas at densities much lower than the $10^4$ cm$^{-3}$ that was originally thought (Pety et al., 2017; Kauffmann et al., 2017; Barnes et al., 2020).

We therefore try to provide some clarity on the density regime that HCN emission probes by improving on previous theoretical models such as Onus et al. (2018). We produce synthetic observations of HCN emission through the use of a Voronoi moving-mesh hydrodynamical code called AREPO that gives us the molecular cloud environments. These simulations were then post-processed in a radiative transfer code called RADMC-3D to produce synthetic images of HCN emission.

In total we created 10 different simulations of molecular cloud environments through cloud-cloud collisions; 4 of which explored the variation in the initial cloud-cloud collisional velocity with each clouds velocity starting from 1.875 km s$^{-1}$ doubling each simulation to a velocity of 15 km s$^{-1}$. The other 6 simulations varied the ISRF strength with 4 simulations of varying values of $G_0$ from 0.17 to 170 in factors of 10.

One simulation of a higher CRIR of $300 \times 10^{-17}$ s$^{-1}$ compared to the standard value of $3 \times 10^{-17}$ s$^{-1}$ used for all other simulations.

Through our simulations we found that the initial collisional velocity influenced the formation of dense gas much more compared to that of the variations in the ISRF strength. Surprisingly, a higher ISRF strength provides very little hindrance to the formation of dense gas even though it provides a higher thermal pressure to push against the collapse of a molecular cloud that then forms dense gas. We argue that our simulations indicate that the use of a density threshold of $10^4$ cm$^{-3}$ for star formation is too low and that due to the combination of the free-fall time being much shorter than the time it takes to go from the formation of densities of $10^4$ cm$^{-3}$ to densities of $10^5$ cm$^{-3}$ and the ability to easily destroy gas of densities of $10^4$ cm$^{-3}$ through high collisional cloud velocities.

For the work on the variation of the initial cloud collisional velocities, we find that HCN emission traces gas with a characteristic volumetric density of $\sim 3 \times 10^3$ cm$^{-3}$ and a characteristic visual extinction of $\sim 5$ mag. This characteristic density is more consistent with the research from Pety et al. (2017), Kauffmann et al. (2017) and Barnes et al. (2020) than those that use $10^4$ cm$^{-3}$ as their characteristic density of HCN emission. This characteristic density of $\sim 3 \times 10^3$ cm$^{-3}$ has implications in observational studies such as Krumholz & Tan (2007), where this lower characteristic density disputes their argument that HCN emission is evidence of slow star formation. This is due to the fact that the free-fall time for a density of $\sim 3 \times 10^3$ cm$^{-3}$ would increase compared to a density of $1 \times 10^4$ cm$^{-3}$ and through their own equation of star formation rate per free-fall time this lower characteristic density would increase star formation rate per free-fall time to be as "fast" as other tracers shown in Figures 4.16 and 5.11.

We find a luminosity-to-mass conversion factor of $\alpha_{\mathrm{HCN}}^{\mathrm{A_V}} = 6.79\ \mathrm{M_\odot\,(K\,km\,s^{-1}\,pc^2)^{-1}}$ for $\mathrm{A_V} > 8$ mag and $\alpha_{\mathrm{HCN}}^{\mathrm{n_{thr}}} = 8.62\ \mathrm{M_\odot\,(K\,km\,s^{-1}\,pc^2)^{-1}}$ for $\mathrm{n} > 2.85 \times 10^3$ cm$^{-3}$. When we adopt the "standard" conversion factor with characteristic density $\mathrm{n} > 3 \times 10^4$ cm$^{-3}$, we find that the analysis over-predicts the amount of "dense" gas by at least an order of magnitude. In some cases, the conversion factor predicts gas in the the density range $\mathrm{n} > 3 \times 10^4$ cm$^{-3}$ when no gas above that density exists in our simulations.

For the work on the variation of the ISRF strength, we find that HCN traces gas with a characteristic density of $4.3 \times 10^3$ cm$^{-3}$ and the characteristic visual extinction, $\mathrm{A_{V,char}}$ of 7 mag. An interesting observation was that we find that there appears to be an upper limit/boundary that the characteristic density of HCN can have as the simulations' $G_0$ is increased. It appears that for this environment that we created it is very unlikely that $n_{\mathrm{char}}$ would surpass $10^4\,\mathrm{cm}^{-3}$ no matter how high the $G_0$ is. However, this is not necessarily a universal statement as it is unclear if this observation applies to clouds of different masses.

Our work on HCN emission has shown that it is not as simple to say that HCN emission traces a certain density or that the effective density of HCN emission can be described by one particular observational property such as the optical depth. We show that the effective density of HCN emission has some correlation with the local ISRF strength of the molecular cloud environment and that the effective density of HCN emission from our simulation of highest $\mathrm{G}_0$ value of 170 agrees with the effective density from a similar region of high star formation rate stated by Barnes et al. (2020). We suggest that those observing HCN emission in the local Milky-Way or an environment similar to it should use an effective density of $\sim 3 \times 10^3$ $\mathrm{cm}^{-3}$ with an upper limit of $\sim 1 \times 10^4$ $\mathrm{cm}^{-3}$ for those observing regions of high star formation. Similarly to the effective density, caution should be taken when using the luminosity-to-mass conversion factor.

## 6.2 CAVEATS

As with any study, there are obviously caveats that perhaps arise from the assumptions we took. Our first caveat is how we produce our abundance of HCN. Our HCN abundance is achieved through relating the CO abundance in our simulations to a conversion factor (shown by equation 4.4). It could be argued that since we are tying our HCN abundance to the CO abundance, we are intrinsically lowering the effective density of HCN emission in our work. We argue that although our HCN abundance is tied to the CO abundance, we do bring a variation from the CO abundance through the fact that there is a dependency on the visual extinction, $\mathrm{A_V}$, in the conversion factor (in equation 4.4). Also the Einstein A-coefficients and collisional rate coefficients are very different for HCN compared to CO and therefore using equation 1.2 will lead to a different $n_{\mathrm{crit}}$. However, we would ideally like to be able to form the HCN abundance in a more self-consitent method. Through the use of tracer particles (see Section 6.3 for further details) and a PDR code we could create a lookup table of HCN abundances that are related to the gas temperature, density and visual extinction of the molecular cloud environment in the simulations to achieve our HCN abundances.

We then come to our next caveat by raising the question, is our use of initial conditions such that our clouds are set to be colliding head-on with one another realistic? It could be argued that it is much likely that these clouds will collide with one another at oblique angles and possibly with their cloud centres of axis with one another. We know that from Chapter 3, that the variation in the initial cloud velocity has much more of an impact on the formation and destruction of dense gas than the variation of the ISRF strength. Therefore, its possible that having a more realistic conditions of oblique collision could produce a different outcome on our results in both Chapters 3 and 4.

## 6.3 FUTURE WORK

Following from our caveats, the future work that could be done after the work from this thesis would be to redo some of our research but with the focus on amending the caveats that were in our work. The first work that we could do is to focus on the issue of our clouds colliding head-on which is somewhat straightforward. This would require a change in the initial conditions such that centres of the clouds are change to be off axis. The velocities would be changed from a simple 1d velocity to a 3d velocity vector in which the magnitude of the velocity is taken to be comparable to the velocities seen by studies from Dobbs (2008). The meeting point of the two clouds would be dependent on the velocity vectors of the two clouds. The velocity could be varied so that we have simulations of off centred collisions and simulations in which the centres of both clouds meet.

We could improve our method of producing our abundance of HCN from one that use our CO abundances in the simulation to using tracer particles and a PDR code to produce our HCN abundances. Tracer particles are discrete particles that track the Lagrangian evolution of a model fluid, and can be conceptualised by imagining that these tracer particles are like rubber ducks flowing down a river. They do not influence the voronoi cells in any way and are fluxed from cell to another based on the flow of the gas. They keep a track of variables such as the gas temperature, density, chemical abundance and other variables that are outputted from AREO. Therefore, these tracer particles can be used to track the history of the formation and destruction of the gas. With the use of a PDR code such as UCLCHEM, the chemical abundance of molecules such as $H_2$ and CO can be produced by giving UCLCHEM the history of the properties of the gas (it requires time, density, temperature and $A_V$), which can then be compared to the CO abundance produced by AREPO. But most importantly, UCLCHEM can produce HCN abundance that we can then use for our synthetic observations.

Some work into using UCLCHEM to produce HCN abundance was already made, which can be seen in Figures 6.1, 6.2 and 6.3. The accuracy of our chemical

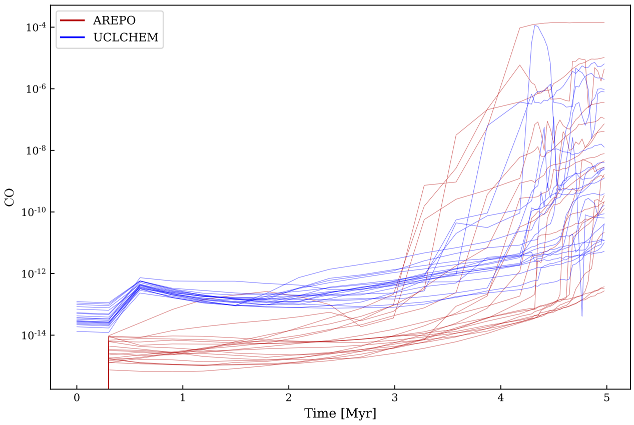

**Figure 6.1.** A small sample of the tracer particle history, showing the formation and destruction of CO abundance with time. The CO abundances formed from Uclchem is shown in blue whilst the red lines denote the CO abundances formed from Arepo.

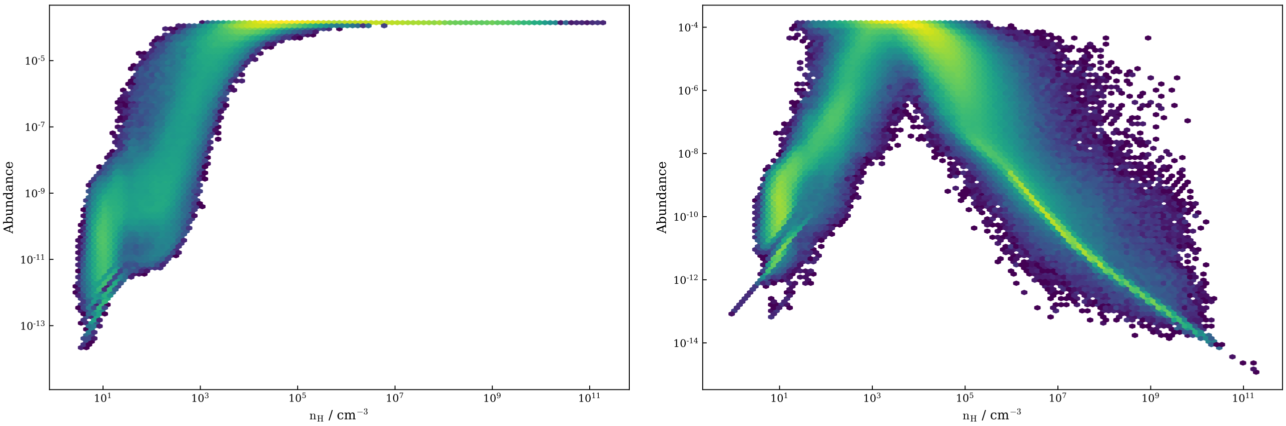

**Figure 6.2.** On the left we have the CO abundance formed from Arepo at all timesteps that are passed into Uclchem. On the right we have the CO abundance formed from Uclchem at all timesteps that are passed into Uclchem.

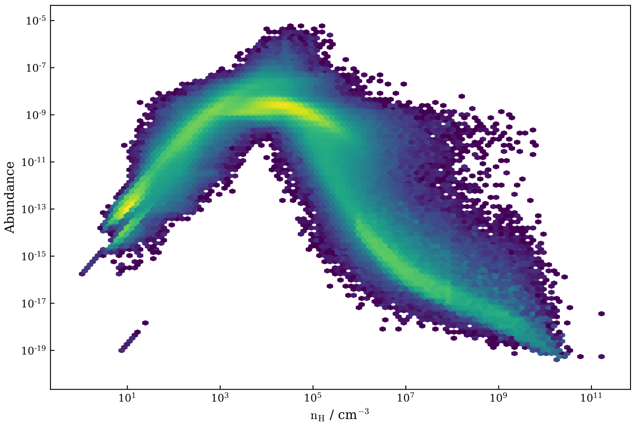

**Figure 6.3.** A figure showing the HCN abundance formed from Uclchem at all timesteps that are passed into Uclchem.

modelling in AREPO can be compared to UCLCHEM which can be seen in Figures 6.1 and 6.2. We see that there is quite a difference in the formation of CO as a function of time. However, they do appear to reach their peak CO abundance at roughly the same time. We also see that in Figure 6.2, AREPO does not consider the freeze out of CO onto dust grains whereas UCLCHEM does consider freeze out of CO onto dust grains. In Figure 6.3, we see the HCN abundance that is formed from UCLCHEM that would be used to produce our new synthetic observations of HCN.

# BIBLIOGRAPHY

Aguerri J., 2012, Advances in Astronomy, 35

André P., et al., 2010, Astronomy & Astrophysics, 518, L102

Badnell N. R., 2006, The Astrophysical Journal Supplement Series, 167, 334

Badnell N. R., et al., 2003, Astronomy & Astrophysics, 406, 1151

Barlow S. E., Dunn G. H., Schauer M., 1984, Physical Review Letters, 52, 902

Barnes J., Hut P., 1986, Nature, 324, 446

Barnes A. T., et al., 2020, Monthly Notices of the Royal Astronomical Society, 497, 1972

Bate M. R., Bonnell I. A., Price N. M., 1995, Monthly Notices of the Royal Astronomical Society, 277, 362

Bergin E. A., Hartmann L. W., Raymond J. C., Ballesteros-Paredes J., 2004, The Astrophysical Journal, 612, 921

Bigiel F., Leroy A., Walter F., Brinks E., de Blok W. J. G., Madore B., Thornley M. D., 2008, The Astronomical Journal, 136, 2846

Bigiel F., Walter F., Blitz L., Brinks E., de Blok W. J. G., Madore B., 2010, The Astronomical Journal, 140, 1194

Bisbas T. G., Haworth T. J., Barlow M. J., Viti S., Harries T. J., Bell T., Yates J. A., 2015, Monthly Notices of the Royal Astronomical Society, 454, 2828

Black J. H., Dalgarno A., 1977, The Astrophysical Journal Supplement Series, 34, 405

Blasi P., 2013, The Astronomy and Astrophysics Review, 21, 70

Blitz L., Shu F. H., 1980, The Astrophysical Journal, 238, 148

Bohlin R. C., Savage B. D., Drake J. F., 1978, The Astrophysical Journal, 224, 132

Bontemps S., et al., 2010, Astronomy and Astrophysics, 518, L85

Brinch C., Hogerheijde M. R., 2010, Astronomy and Astrophysics, 523, A25

Bron E., Bourlot J. L., Petit F. L., 2014, Astronomy & Astrophysics, 569, A100

Burton M. G., Hollenbach D. J., Tielens A. G. G. M., 1990, The Astrophysical Journal, 365, 620

Carty D., Goddard A., Köhler S. P. K., Sims I. R., Smith I. W. M., 2006, Journal of Physical Chemistry A, 110, 3101

Clark P. C., Glover S. C. O., 2015, Monthly Notices of the Royal Astronomical Society, 452, 2057

Clark P. C., Glover S. C. O., Klessen R. S., 2012, Monthly Notices of the Royal Astronomical Society, 420, 745

Clark P. C., Glover S. C. O., Ragan S. E., Duarte-Cabral A., 2019, Monthly Notices of the Royal Astronomical Society, 486, 4622

Crutcher R. M., 1999, The Astrophysical Journal, 520, 706

Crutcher R. M., 2012, Annual Review of Astronomy and Astrophysics, 50, 29

Crutcher R. M., Wandelt B., Heiles C., Falgarone E., Troland T. H., 2010, The Astrophysical Journal, 725, 466

Dedner A., Kemm F., Kröner D., Munz C. D., Schnitzer T., Wesenberg M., 2002, Journal of Computational Physics, 175, 645

Dobbs C. L., 2008, Monthly Notices of the Royal Astronomical Society, 391, 844

Draine B. T., 1978, The Astrophysical Journal Supplement Series, 36, 595

Draine B. T., 2011, Physics of the Interstellar and Intergalactic Medium by Bruce T. Draine. Princeton University Press, 2011.

Draine B. T., Bertoldi F., 1996, The Astrophysical Journal, 468, 269

Dubey A., et al., 2008, 385, 145

Dullemond C. P., Juhasz A., Pohl A., Sereshti F., Shetty R., Peters T., Commercon B., Flock M., 2012, Astrophysics Source Code Library

Dumouchel F., Faure A., Lique F., 2010, Monthly Notices of the Royal Astronomical Society, 406, 2488

Elmegreen B. G., 1994, The Astrophysical Journal Letters, 425, L73

Elmegreen B. G., Scalo J., 2004, Annual Review of Astronomy and Astrophysics, 42, 211

Evans N. J., Kim K.-T., Wu J., Chao Z., Heyer M., Liu T., Nguyen-Lu'o'ng Q., Kauffmann J., 2020, The Astrophysical Journal, 894, 103

Ewen H. I., Purcell E. M., 1951, Nature, 168, 356

Faure A., Varambhia H. N., Stoecklin T., Tennyson J., 2007, Monthly Notices of the Royal Astronomical Society, 382, 840

Federrath C., 2015, Monthly Notices of the Royal Astronomical Society, 450, 4035

Federrath C., Banerjee R., Clark P. C., Klessen R. S., 2010, The Astrophysical Journal, 713, 269

Ferland G. J., Peterson B. M., Horne K., Welsh W. F., Nahar S. N., 1992, The Astrophysical Journal, 387, 95

Field G. B., Goldsmith D. W., Habing H. J., 1969, The Astrophysical Journal Letters, 155, L149

Fryxell B., et al., 2000, The Astrophysical Journal Supplement Series, 131, 273

Fuente A., et al., 2019, Astronomy & Astrophysics, 624, A105

Gallagher M. J., et al., 2018, The Astrophysical Journal, 868, L38

Gao Y., Solomon P. M., 2004a, The Astrophysical Journal Supplement Series, 152, 63

Gao Y., Solomon P. M., 2004b, The Astrophysical Journal, 606, 271

Gao Y., Carilli C. L., Solomon P. M., Bout P. A. V., 2007, The Astrophysical Journal, 660, L93

García-Burillo S., Usero A., Alonso-Herrero A., Graciá-Carpio J., Pereira-Santaella M., Colina L., Planesas P., Arribas S., 2012, Astronomy & Astrophysics, 539, A8

Geppert W. D., et al., 2005, in Journal of Physics Conference Series. pp 26–31

Glassgold A. E., Langer W. D., 1974, The Astrophysical Journal, 193, 73

Glassgold A. E., Langer W. D., 1975, The Astrophysical Journal, 197, 347

Glover S. C. O., Clark P. C., 2012a, Monthly Notices of the Royal Astronomical Society, 421, 9

Glover S. C. O., Clark P. C., 2012b, Monthly Notices of the Royal Astronomical Society, 421, 116

Glover S. C. O., Jappsen A.-K., 2007, The Astrophysical Journal, 666, 1

Glover S. C. O., Mac Low M.-M., 2007, The Astrophysical Journal, 659, 1317

Glover S. C. O., Federrath C., Mac Low M.-M., Klessen R. S., 2010, Monthly Notices of the Royal Astronomical Society, 404, 2

Godunov S. K., Bohachevsky I., 1959, Matematičeskij sbornik, 47(89), 271

Goldsmith P. F., Heyer M., Narayanan G., Snell R., Li D., Brunt C., 2008, The Astrophysical Journal, 680, 428

Gong M., Ostriker E. C., Wolfire M. G., 2017, The Astrophysical Journal, 843, 38

Habing H. J., 1968, Bulletin of the Astronomical Institutes of the Netherlands, 19, 421

Hacar A., Bosman A. D., van Dishoeck E. F., 2020, Astronomy & Astrophysics, 635, A4

Hao C.-N., Kennicutt R. C., Johnson B. D., Calzetti D., Dale D. A., Moustakas J., 2011, The Astrophysical Journal, 741, 124

Harada N., Nishimura Y., Watanabe Y., Yamamoto S., Aikawa Y., Sakai N., Shimonishi T., 2019, The Astrophysical Journal, 871, 238

Harries T., Haworth T., Acreman D., Ali A., Douglas T., 2019, The TORUS Radiation Transfer Code (arxiv:1903.06672)

Hartmann L., Ballesteros-Paredes J., Bergin E. A., 2001, The Astrophysical Journal, 562, 852

Heays A. N., Bosman A. D., van Dishoeck E. F., 2017, Astronomy & Astrophysics, 602, A105

Hennebelle P., Inutsuka S.-i., 2019, Frontiers in Astronomy and Space Sciences, 6

Herbst E., Miller S., Oka T., Watson J. K., Herbst E., 2000, Philosophical Transactions of the Royal Society of London. Series A: Mathematical, Physical and Engineering Sciences, 358, 2523

Hinkle K. H., Aringer B., Lebzelter T., Martin C. L., Ridgway S. T., 2000, Astronomy and Astrophysics, 363, 1065

Hollenbach D., McKee C. F., 1979, The Astrophysical Journal Supplement Series, 41, 555

Hollenbach D. J., Werner M. W., Salpeter E. E., 1971, The Astrophysical Journal, 163, 165

Hollenbach D., Kaufman M. J., Neufeld D., Wolfire M., Goicoechea J. R., 2012, The Astrophysical Journal, 754, 105

Hosokawa T., Inutsuka S.-i., 2006, The Astrophysical Journal, 646, 240

Hummer D. G., Storey P. J., 1998, Monthly Notices of the Royal Astronomical Society, 297, 1073

Hunter G. H., Clark P. C., Glover S. C. O., Klessen R. S., 2021, arXiv:2109.06195 [astro-ph]

Indriolo N., Geballe T. R., Oka T., McCall B. J., 2007, The Astrophysical Journal, 671, 1736

Jacobs T. A., Giedt R. R., Cohen N., 1967, The Journal of Chemical Physics, 47, 54

Janev R. K., Langer W. D., Post D. E., Evans K., 1987, Elementary Processes in Hydrogen-Helium Plasmas. Springer, Berlin, Heidelberg

Jankowski P., Szalewicz K., 2005, Journal of Chemical Physics, 123, 104301

Jansen, D.J., 1995, PhD thesis, Leiden University

Jiménez-Donaire M. J., et al., 2017, Monthly Notices of the Royal Astronomical Society, 466, 49

Jones G. H., Clark P. C., Glover S. C. O., Hacar A., 2023, Monthly Notices of the Royal Astronomical Society

Jørgensen J. K., 2004, Astronomy & Astrophysics, 424, 589

Jura M., 1974, The Astrophysical Journal, 191, 375

Kainulainen J., Beuther H., Henning T., Plume R., 2009, Astronomy and Astrophysics, 508, L35

Karpas Z., Anicich V., Huntress W. T., 1979, Journal of Chemical Physics, 70, 2877

Kauffmann J., Goldsmith P. F., Melnick G., Tolls V., Guzman A., Menten K. M., 2017, Astronomy and Astrophysics, 605, L5

Kennicutt Jr. R. C., 1989, The Astrophysical Journal, 344, 685

Kennicutt Jr. R. C., 1998, The Astrophysical Journal, 498, 541

Kennicutt R. C., Evans N. J., 2012, Annual Review of Astronomy and Astrophysics, 50, 531

Kim J. K., Theard L. P., Huntress W. T. Jr., 1975, Chemical Physics Letters, 32, 610

Könyves V., et al., 2010, Astronomy & Astrophysics, 518, L106

Kruijssen J. M. D., Longmore S. N., Elmegreen B. G., Murray N., Bally J., Testi L., Kennicutt Jr R. C., 2014, Monthly Notices of the Royal Astronomical Society, 440, 3370

Krumholz M. R., 2014, Monthly Notices of the Royal Astronomical Society, 437, 1662

Krumholz M. R., McKee C. F., 2005, The Astrophysical Journal, 630, 250

Krumholz M. R., Tan J. C., 2007, The Astrophysical Journal, 654, 304

Krumholz M. R., Thompson T. A., 2007, The Astrophysical Journal, 669, 289

Kulesa C. A., et al., 2012, Proceedings of the International Astronomical Union, 8, 256

Lada C. J., Lombardi M., Alves J. F., 2009, The Astrophysical Journal, 703, 52

Lada C. J., Lombardi M., Alves J. F., 2010, The Astrophysical Journal, 724, 687

Lada C. J., Forbrich J., Lombardi M., Alves J. F., 2012, The Astrophysical Journal, 745, 190

Lepp S., Shull J. M., 1983, The Astrophysical Journal, 270, 578

Leroy A. K., et al., 2017, The Astrophysical Journal, 835, 217

Levrier F., Petit F. L., Hennebelle P., Lesaffre P., Gerin M., Falgarone E., 2012, Astronomy & Astrophysics, 544, A22

Linder F., Janev R. K., Botero J., 1995, in Janev R. K., ed., Atomic and Molecular Processes in Fusion Edge Plasmas. p. 397

Liow K. Y., Dobbs C. L., 2020, \mnras, 499, 1099

Liszt H. S., Pety J., Lucas R., 2010, Astronomy & Astrophysics, 518, A45

Longmore S. N., et al., 2013, Monthly Notices of the Royal Astronomical Society, 429, 987

Mac Low M.-M., Klessen R. S., 2004, Reviews of Modern Physics, 76, 125

Mac Low M. M., Shull J. M., 1986, The Astrophysical Journal, 302, 585

Martin P. G., Schwarz D. H., Mandy M. E., 1996, The Astrophysical Journal, 461, 265

Martin P. G., Keogh W. J., Mandy M. E., 1998, The Astrophysical Journal, 499, 793

Mathis J. S., Mezger P. G., Panagia N., 1983, Astronomy and Astrophysics, 128, 212

McCall B. J., et al., 2004, Physical Review. A, 70

McElroy D., Walsh C., Markwick A. J., Cordiner M. A., Smith K., Millar T. J., 2013, Astronomy & Astrophysics, 550, A36

Mitchell G. F., 1984, The Astrophysical Journal Supplement Series, 54, 81

Miyoshi T., Kusano K., 2005, Journal of Computational Physics, 208, 315

Moore T. J. T., Urquhart J. S., Morgan L. K., Thompson M. A., 2012, Monthly Notices of the Royal Astronomical Society, 426, 701

Murphy E. J., et al., 2011, The Astrophysical Journal, 737, 67

Nahar S. N., 2000, The Astrophysical Journal Supplement Series, 126, 537

Nelson R. P., Langer W. D., 1997, The Astrophysical Journal, 482, 796

Nelson R. P., Langer W. D., 1999, The Astrophysical Journal, 524, 923

Nguyen Q.-R., Jackson J. M., Henkel C., Truong B., Mauersberger R., 1992, The Astrophysical Journal, 399, 521

Norman M. L., 2000, 9, 66

Onus A., Krumholz M. R., Federrath C., 2018, Monthly Notices of the Royal Astronomical Society, 479, 1702

Pakmor R., Springel V., 2013, Monthly Notices of the Royal Astronomical Society, 432, 176

Pakmor R., Bauer A., Springel V., 2011, Monthly Notices of the Royal Astronomical Society, 418, 1392

Pakmor R., Springel V., Bauer A., Mocz P., Munoz D. J., Ohlmann S. T., Schaal K., Zhu C., 2016, Monthly Notices of the Royal Astronomical Society, 455, 1134

Petuchowski S. J., Dwek E., Allen Jr. J. E., Nuth III J. A., 1989, The Astrophysical Journal, 342, 406

Pety J., et al., 2013, The Astrophysical Journal, 779, 43

Pety J., et al., 2017, Astronomy and Astrophysics, 599, A98

Pineda J. L., Goldsmith P. F., Chapman N., Snell R. L., Li D., Cambrésy L., Brunt C., 2010, The Astrophysical Journal, 721, 686

Porter T. A., Strong A. W., 2005, 4, 77

Powell K. G., Roe P. L., Linde T. J., Gombosi T. I., De Zeeuw D. L., 1999, Journal of Computational Physics, 154, 284

Prasad S. S., Huntress Jr. W. T., 1980, The Astrophysical Journal Supplement Series, 43, 1

Priestley F. D., Whitworth A. P., 2020, Monthly Notices of the Royal Astronomical Society, 499, 3728

Priestley F. D., Whitworth A. P., 2021, Monthly Notices of the Royal Astronomical Society, 506, 775

Querejeta M., et al., 2019, Astronomy & Astrophysics, 625, A19

Ragan S. E., Moore T. J. T., Eden D. J., Hoare M. G., Urquhart J. S., Elia D., Molinari S., 2018, Monthly Notices of the Royal Astronomical Society, 479, 2361

Riechers D. A., Walter F., Carilli C. L., Weiss A., Bertoldi F., Menten K. M., Knudsen K. K., Cox P., 2006, The Astrophysical Journal Letters, 645, L13

Rigby A. J., et al., 2019, Astronomy & Astrophysics, Volume 632, id.A58, 24, 632, A58

Roman-Duval J., Heyer M., Brunt C. M., Clark P., Klessen R., Shetty R., 2016, The Astrophysical Journal, 818, 144

Schauer A. T. P., Glover S. C. O., Klessen R. S., Clark P., 2021, Monthly Notices of the Royal Astronomical Society, 507, 1775

Schmidt M., 1959, The Astrophysical Journal, 129, 243

Schöier F. L., van der Tak F. F. S., van Dishoeck E. F., Black J. H., 2005, Astronomy & Astrophysics, 432, 369

Sembach K. R., Howk J. C., Ryans R. S. I., Keenan F. P., 2000, The Astrophysical Journal, 528, 310

Shetty R., Glover S. C., Dullemond C. P., Klessen R. S., 2011, Monthly Notices of the Royal Astronomical Society, 412, 1686

Shetty R., Kelly B. C., Rahman N., Bigiel F., Bolatto A. D., Clark P. C., Klessen R. S., Konstandin L. K., 2014, Monthly Notices of the Royal Astronomical Society, 437, L61

Shirley Y. L., 2015, Publications of the Astronomical Society of the Pacific, 127, 299

Sobolev V. V., 1957, Soviet Astronomy, 1, 678

Springel V., 2005, Monthly Notices of the Royal Astronomical Society, 364, 1105

Springel V., 2010, Monthly Notices of the Royal Astronomical Society, 401, 791

Springel V., Yoshida N., White S. D. M., 2001, New Astronomy, 6, 79

Stahler S. W., Palla F., 2004, The Formation of Stars

Stancil P. C., Schultz D. R., Kimura M., Gu J. P., Hirsch G., Buenker R. J., 1999, Astronomy and Astrophysics Supplement Series, 140, 225

Tafalla M., Usero A., Hacar A., 2021, Astronomy & Astrophysics, 646, A97

Tan J. C., 2000, The Astrophysical Journal, 536, 173

Teyssier R., 2002, Astronomy and Astrophysics, 385, 337

Toro E. F., 1997, Riemann Solvers and Numerical Methods for Fluid Dynamics. Springer, Berlin, Heidelberg

Tress R. G., Smith R. J., Sormani M. C., Glover S. C. O., Klessen R. S., Mac Low M.-M., Clark P. C., 2020, Monthly Notices of the Royal Astronomical Society, 492, 2973

Trevisan C. S., Tennyson J., 2002, Plasma Physics and Controlled Fusion, 44, 1263

Tsang W., Hampson R. F., 1986, Journal of Physical and Chemical Reference Data, 15, 1087

Urquhart J. S., et al., 2014, Monthly Notices of the Royal Astronomical Society, 443, 1555

Usero A., et al., 2015, The Astronomical Journal, 150, 115

Vissapragada S., Buzard C. F., Miller K. A., O'Connor A. P., de Ruette N., Urbain X., Savin D. W., 2016, The Astrophysical Journal, 832, 31

Voronov G. S., 1997, Atomic Data and Nuclear Data Tables, 65, 1

Wakelam V., et al., 2010, Space Science Reviews, 156, 13

Weinberger R., Springel V., Pakmor R., 2020, The Astrophysical Journal Supplement Series, 248, 32

Weingartner J. C., Draine B. T., 2001, The Astrophysical Journal, 563, 842

Wollenberg K. M. J., Glover S. C. O., Clark P. C., Klessen R. S., 2020, Monthly Notices of the Royal Astronomical Society, 494, 1871

Wong T., Blitz L., 2002, The Astrophysical Journal, 569, 157

Woodall J., Agúndez M., Markwick-Kemper A. J., Millar T. J., 2007, Astronomy and Astrophysics, 466, 1197

Wu J., Evans II N. J., Gao Y., Solomon P. M., Shirley Y. L., Vanden Bout P. A., 2005, The Astrophysical Journal Letters, 635, L173

Wu J., Evans II N. J., Shirley Y. L., Knez C., 2010, The Astrophysical Journal Supplement Series, 188, 313

Wu B., Tan J. C., Christie D., Nakamura F., Van Loo S., Collins D., 2017, \apj, 841, 88

Yang B., Stancil P. C., Balakrishnan N., Forrey R. C., 2010, The Astrophysical Journal, 718, 1062

Zanchet A., Bussery-Honvault B., Jorfi M., Honvault P., 2009, Physical Chemistry Chemical Physics (Incorporating Faraday Transactions), 11, 6182

Zuckerman B., Evans II N. J., 1974, The Astrophysical Journal, 192, L149

de Ruette N., Miller K. A., O'Connor A. P., Urbain X., Buzard C. F., Vissapragada S., Savin D. W., 2016, The Astrophysical Journal, 816, 31

van Dishoeck E. F., 1988, in Millar T. J., Williams D. A., eds, Rate Coefficients in Astrochemistry. Astrophysics and Space Science Library. Springer Netherlands, Dordrecht, pp 49–72

van Leer B., 1984, SIAM Journal on Scientific and Statistical Computing, 5, 1

van der Tak F. F. S., Black J. H., Schöier F. L., Jansen D. J., van Dishoeck E. F., 2007, Astronomy and Astrophysics, 468, 627